COUPLED THERMO-HYDRO-MECHANICAL COMPUTATIONAL MODELING OF AN END BEARING HEAT EXCHANGER PILE

by

TRI VAN TRAN

B.Eng., CanTho University, VietNam, 2005

A THESIS

Submitted in partial fulfillment of the requirements for the degree

MASTER OF SCIENCE

Department of Civil Engineering
College of Engineering

KANSAS STATE UNIVERSITY
Manhattan, Kansas

2015

Approved by:

Major Professor
Dr. Dunja Perić

Copyright

Abstract

Piles have been used for many years in civil infrastructure as foundations for buildings, bridges, and retaining walls. Energy piles are thermo-active foundation systems that use geothermal energy for heating and cooling of buildings. Ground source heat is a very attractive, economical, efficient and sustainable alternative to current heating practices. Unlike the air temperature, the temperature below the Earth's surface remains relatively constant throughout the year, somewhere between 10^{o}C to 15^{o}C below a depth of 6 m to 9 m (Kelly, 2011). This provides an opportunity for construction of thermo-active foundation systems with embedded geothermal loops. The main purpose of such thermo-active system is to transfer deep ground heat to a building through the fluid circulating within the geothermal loop. It is because these thermo-active foundation systems enable heat exchange between the deep ground and the building that is called the heat exchanger pile (HEP). The thermal energy supplied by a HEP can then supplement air-pump-based heating/cooling system.

Although heat exchanger piles have been successfully implemented in Europe and Asia, their usage in U.S. remains uncommon. One reason for this might be currently limited understanding of the associated soil-structure interaction, thus unfavorably affecting the design procedures. To this end, a study was undertaken to investigate the predictive capabilities of computational models and to gain a better understanding of the load-transfer mechanisms of energy piles. Thus, coupled thermo-hydro-mechanical computational modeling of a single actual end bearing HEP was carried out for different loading scenarios including thermal and mechanical loads by using the finite element code ABAQUS/Standard 6.13-2. The results of the analyses of the heat exchanger pile with two different types of layered soil profile are presented: isotropic and anisotropic. The computational model was validated and verified successfully against field test results for all considered loading scenarios. Additional analyses were performed to gain a deeper insight into the effects of soil layering and on the behavior of energy piles. It was found that changes in the soil stiffness affected primarily the head displacement and vertical stresses and strains in the pile.

Table of Contents

List of Figures

List of Tables

Acknowledgements

I would like to thanks my supervisor, Prof. Dunja Perić, for her teaching, continuous guidance and advice throughout this research, for her valuable time and patience. Special thanks to Prof. Gerard J. Kluitenberg for his kindness and providing information, which facilitated the heat transfer analysis. My appreciation also extends to Prof. Asad Esmaeily for his helpful suggestions.

I am extremely grateful to everybody in the Department of Civil Engineering who has supported me in my study and my work, and everybody who always made me feel comfortable and treated me kindly.

In addition, I want to give many thanks to all of my friends in Viet Nam and my colleagues here for their helping me during my student life.

Finally, I would like to thank my family for their support and encouragement during my time at KSU. Especially, I still do not have enough words to express my love for my wife, who gave me strength when I was weak, who helped me out when I was stressed and who shared with me everything in my life.

Manhattan, Kansas 04 / 10 / 2015

Tri Van Tran

Chapter 1 - Introduction

1.1 Geothermal Energy

1.1.1 Background

Geothermal energy is thermal energy generated by the Earth and stored in the Earth. Geothermal power is cost effective, reliable, sustainable, and environmentally friendly, but its use has been limited. Recent scientific advances have dramatically expanded the range and size of practical resources, especially for applications such as home heating, thus opening a potential for widespread exploitation. Geothermal wells release greenhouse gases trapped deep within the earth, but these emissions are much lower per energy unit than those of fossil fuels. As a result, geothermal power has the potential to help mitigate global warming if widely deployed in place of fossil fuels.

Table 1.1 Summary of the various categories of direct use of geothermal energy worldwide, 1995-2010 (Lund et al. 2010)

Capacity, MWt

	2010	**2005**	**2000**	**1995**
Geothermal Heat Pumps	35,236	15,384	5,275	1,854
Space Heating	5,391	4,366	3,263	2,579
Greenhouse Heating	1,544	1,404	1,246	1,085
Aquaculture Pond Heating	653	616	605	1,097
Agricultural Drying	127	157	74	67
Industrial Uses	533	484	474	544
Bathing and Swimming	6,689	5,401	3,957	1,085
Cooling / Snow Melting	368	371	114	115
Others	41	86	137	238
Total	**50,583**	**28,269**	**15,145**	**8,664**

Utilization, TJ/yr

	2010	2005	2000	1995
Geothermal Heat Pumps	214,782	87,503	23,275	14,617
Space Heating	62,984	55,256	42,926	38,230
Greenhouse Heating	23,264	20,661	17,864	15,742
Aquaculture Pond Heating	11,521	10,976	11,733	13,493
Agricultural Drying	1,662	2,013	1,038	1,124
Industrial Uses	11,746	10,868	10,220	10,120
Bathing and Swimming	109,032	83,018	79,546	15,742
Cooling / Snow Melting	2,126	2,032	1,063	1,124
Others	956	1,045	3,034	2,249
Total	**438,071**	**273,372**	**190,699**	**112,441**

Capacity Factor

	2010	2005	2000	1995
Geothermal Heat Pumps	0.19	0.18	0.14	0.25
Space Heating	0.37	0.40	0.42	0.47
Greenhouse Heating	0.48	0.47	0.45	0.46
Aquaculture Pond Heating	0.56	0.57	0.61	0.39
Agricultural Drying	0.42	0.41	0.44	0.53
Industrial Uses	0.70	0.71	0.68	0.59
Bathing and Swimming	0.52	0.49	0.64	0.46
Cooling / Snow Melting	0.18	0.18	0.30	0.31
Others	0.73	0.39	0.70	0.30
Total	**0.27**	**0.31**	**0.40**	**0.41**

The Earth's geothermal resources are theoretically more than adequate to supply the energy needs of humanity, but currently only a very small fraction may be profitably exploited. Drilling and exploration for deep resources is very expensive and it depends on technology, energy prices, and subsidies. Geothermal energy can be used for the generation of electricity or for direct use, including building heating, growing plants in greenhouses, drying crops, heating

water at fish farms, and for several industrial processes such as pasteurizing milk. Many technologies have been developed to take advantage of geothermal energy. Geothermal heat pumps (GHP) system is one of the technologies which were seemly introduced by using the shallow ground to heat and cool buildings.

Figure 1.1 Geothermal direct applications worldwide in 2010, distributed by percentage of total installed capacity (a) and percentage of total energy use (b) (Lund et al. 2010)

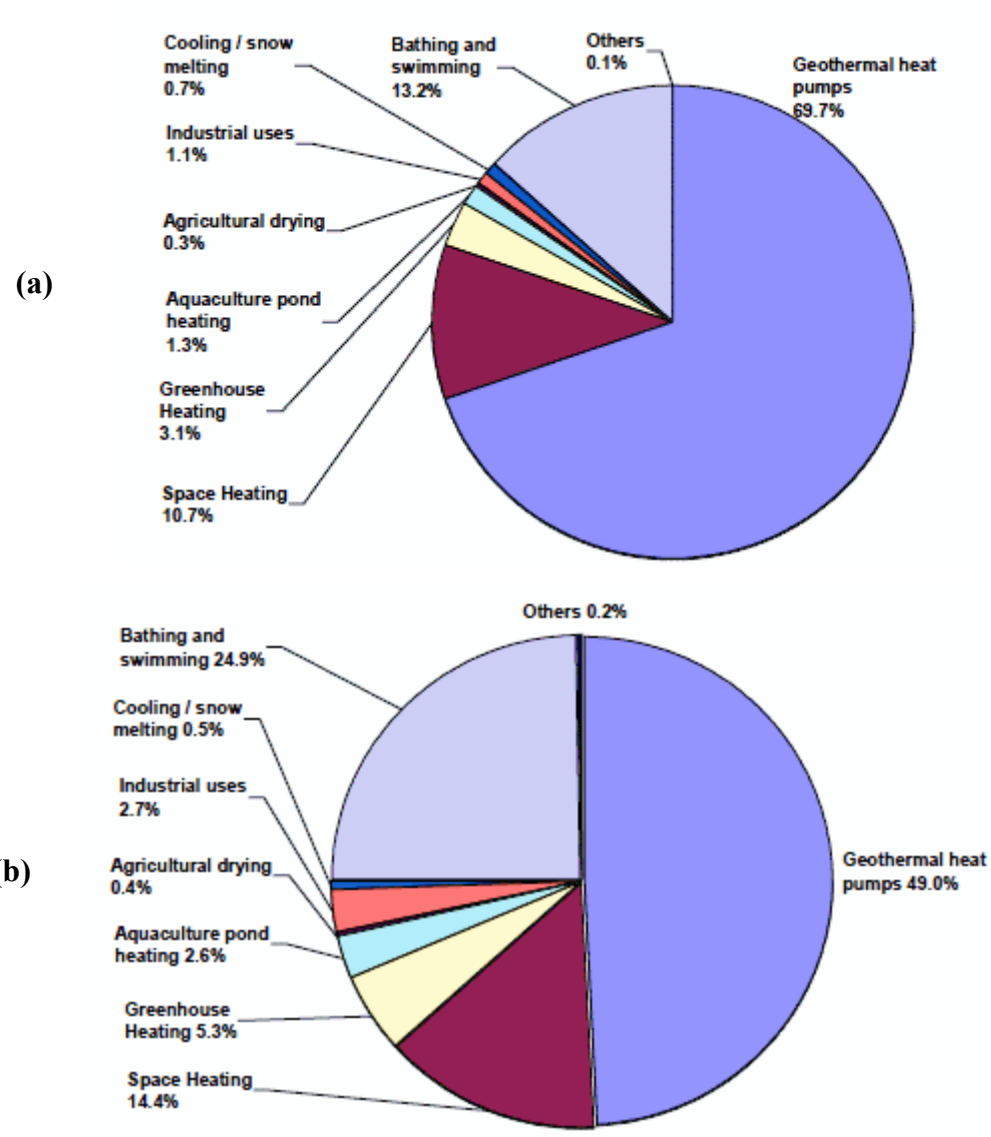

The shallow ground or upper 10 feet of the Earth's surface is warmer than the air above it in the winter and cooler in the summer. GHP can tap into this resource for heating and cooling the buildings. At deeper depths the temperature of the ground is constant throughout the year.

For example, in Kansas the ground temperature is nearly constant and equal to 50°F to 60°F (10°C to 15°C) at depths larger than 30 ft (9.14 m) from the ground surface regardless the climate (http://www.architectmagazine.com/technology/going-underground_o).

GHP systems consist of three parts:

1. The heat pump unit
2. The ground heat exchanger
3. The air delivery system

Figure 1.2 The three GHP system major components. Adapted from Clean Energy Project Analysis: RETScreen Engineering Cases Textbook (Minister of Natural Resources Canada 2001-2005)

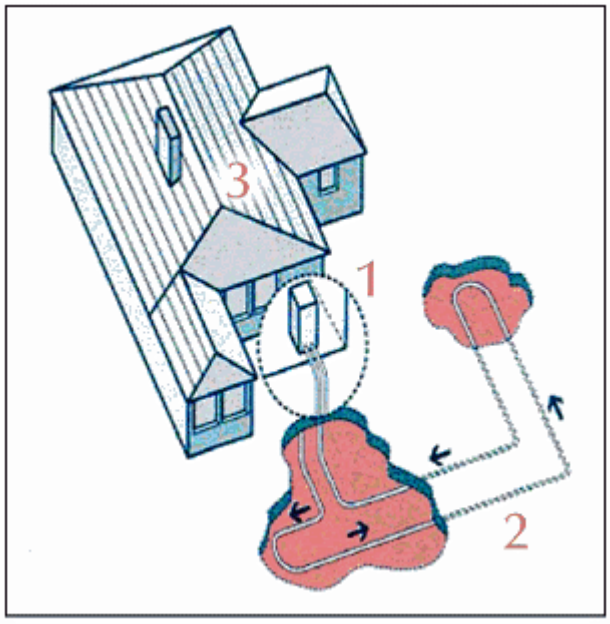

1. Heat pump
2. Earth connection
3. Heating/Colling distribution system

The heat exchanger is basically a system of pipes called a loop, which is buried in the shallow ground near the building. A fluid (usually water or a mixture of water and antifreeze) circulates through the pipes to absorb or relinquish heat within the ground. In the winter, the heat pump removes heat from the heat exchanger and pumps it into the indoor air delivery system. In the summer, the process is reversed, and the heat pump moves heat from the indoor air to the heat exchanger. The heat removed from the indoor air during the summer can also be used to heat water, providing a free source of hot water.

GHP uses much less energy than conventional heating systems, since they draw heat from the ground. They are also more efficient when cooling. Not only does this save energy and money, it reduces air pollution as well. All areas of the United States have nearly constant shallow-ground temperatures, which are suitable for geothermal heat pumps.

1.1.2 Type of Geothermal Heat Pump Systems

Geothermal systems can be installed in an open loop or closed loop. The type of geothermal systems installed depends on geological conditions, heating/cooling load, type of space to be heated/cooled, supply temperature from underground, and availability of ground water.

Open loop system

Open loop systems are used where an abundant supply of water from a well, pond, lake, or river is available. Water is pumped and circulated directly through the polyethylene piping. Once it has circulated through the system, the water returns to the ground through the well, a recharge well, or surface discharge.

Figure 1.3 An open loop geothermal system. Adapted from Geothermal Systems (Morris and Sheets, 2009)

Closed loop system

A closed loop system consists of underground continuous piping loops that are filled with an anti-freeze solution that helps transfer the ground temperature to the geothermal heat pump. A closed ground loop system can be installed either vertically or horizontally depending on the site conditions.

Figure 1.4 Closed loop geothermal system. Adapted from Geothermal Systems (Morris and Sheets, 2009)

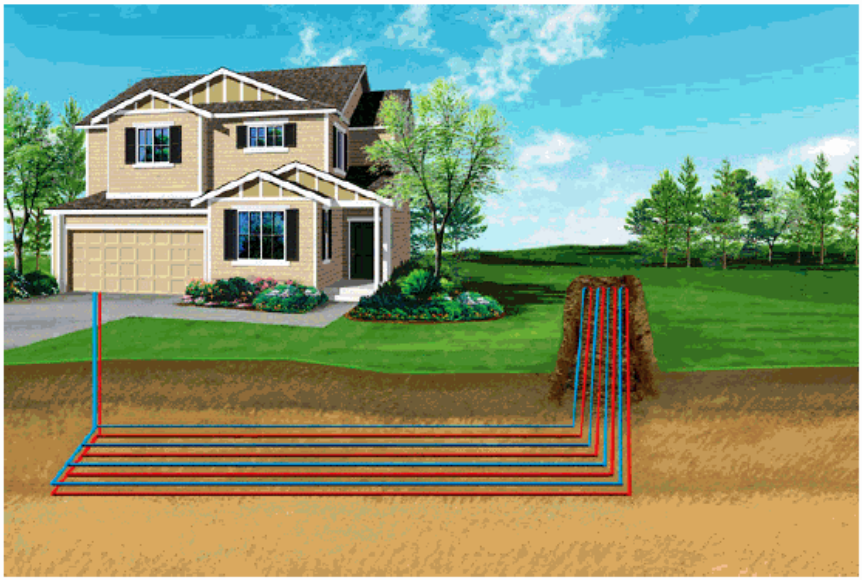

a. Horizontal loop geothermal system

b. Vertical loop geothermal system

c. Pond loop geothermal system

1.2 Research Objective

Ground-source heat exchange (GSHE) systems have been used for many years. They reduce the energy demand of heating and cooling systems compared with the traditional air-source heat pump systems. Thermo-active geotechnical systems such as energy foundations are a feasible approach to enhance implementation of GSHE systems by reducing installation costs through taking advantage of building foundation which is necessary for load transfer to the ground. Concrete has good thermal conductivity and thermal storage capacity, thus making it an ideal material for harvesting the heat from the ground. Although energy foundations are gaining acceptance in Europe, including the United Kingdom, Switzerland and Austria, their usage in U.S remains infrequent. One of the reasons for this might be currently limited understanding of the behavior of energy piles, and especially currently lacking knowledge about the pile-soil interaction of energy piles. In addition, the number of existing relevant case studies is extremely limited. To this end, the present study addresses uncertainties in the soil structure interaction in energy piles through computational modeling of a single energy pile. Specifically, the goals of the undertaken modelling efforts are:

1. To investigate the mechanical behaviors of three types of heat exchanger piles: floating pile, semi-floating pile, and end bearing pile.

2. To investigate the effects of soil layering and stiffness on the behavior of energy piles.

3. To study the effects of thermal properties of soils on deformation, stresses and strains in energy piles.

4. To evaluate the displacement, stresses and strains of the pile during heating and cooling cycles.

5. To deduce overall implications for design of heat exchanger piles.

1.3 Thesis Organization

The thesis contains organized in six chapters. Chapter 1 presents the concept of the ground energy systems in general and it briefly explains the main research objectives. Chapter 2 provides a literature review of a single energy pile subjected to thermal and mechanical loading. Chapter 3 is the introduction about the heat transfer in soils. Thermal properties of soils are discussed in this chapter, including thermal conductivity, coefficient of thermal expansion and heat capacity of the soils. Coupled thermo-hydro-mechanical computational modelling of a HEP is carried out in Chapter 4. Reinforced concrete pile and soils properties are presented in this chapter. Numerical modelling has been carried out on two different cases of pile heat exchangers: thermal loading only and mechanical and thermal loading when soils are responded as an isotropic elastic material and anisotropic elastic material. Chapter 5 presents the results of the computational modelling, which was performed to advance the knowledge about the soil structure interaction of energy piles. The overall conclusions and suggestions for future research are provided in Chapter 6. In addition, design recommendations are also presented in this chapter.

Chapter 2 - Literature Review

Over last 20 years heat exchanger piles (HEP) have been studied by various researchers to improve understanding of their behavior, including the related soil structure interaction. The research efforts have been mainly focused at numerical modeling and field testing. Table 2.1 shows most of the previous full scale field studies. They are discussed next.

Table 2.1 Previous studies on full scale field experiments on HEP

No. of case	Author / Year	Location of the project
1	Laloui et al. (2006)	Lausanne / Switzerland
2	Brandl, (2006)	Bad Schallerbach / Austria
3	Bourne-Webb et al. (2009)	Lambet College / London
4	McCartney and Murphy, (2012)	Denver / Colorado
5	Murphy et al. (2014)	US Air Force Academy
6	Sutman et al. (2014)	Richmond / Texas

2.1 Heat Exchanger Piles in the World

2.1.1 Laloui et al. (2006)

Laloui et al. (2006) conducted a study of an end bearing HEP by comparing in situ tests and results of numerical modelling. The field tests were carried out at the Swiss Federal Institute of technology (four story building) in Lausanne, Switzerland. The drilled HEP was 88 cm in diameter and 25.8 m in length. A coupled thermal-hydro-mechanical finite element model was developed and a single pile subjected to thermal loading, and thermal and mechanical loadings was analyzed. The soil was modelled as a Drucker Prager thermo elastic-plastic material while the HEP was assumed to behave as a thermo elastic material. The contact between the pile and soil was assumed to be perfectly rough. The HEP was embedded into a soil profile consisting of 4 different layers, which are underlain by the bedrock (Figure 2.1)

Figure 2.1 The soil profile and the instrumentation of the EPFL pile test (Laloui et al. 2006)

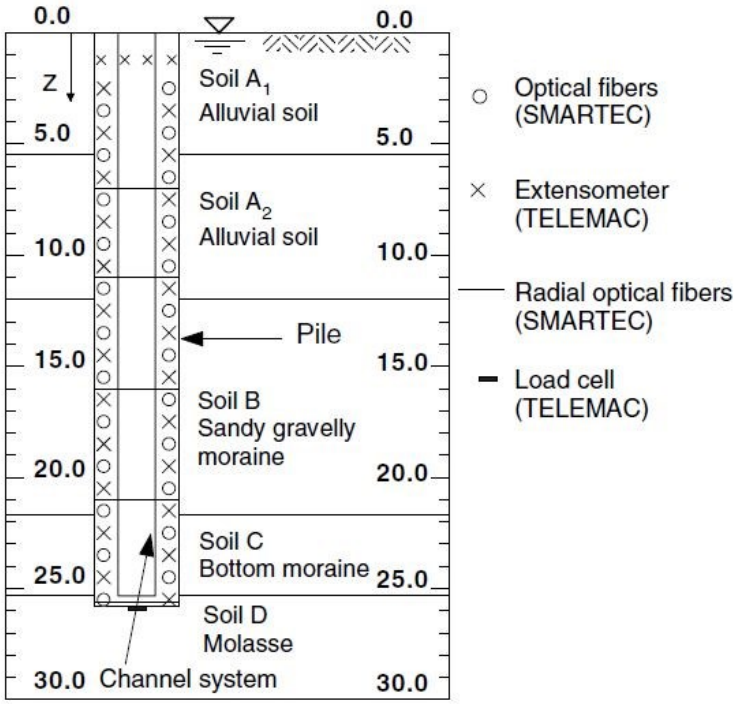

The results indicated that a large axial stress was generated at the end of a heating cycle at the pile tip. On the contrary, the mechanical load affected mostly the pile head. The axial stress induced by the thermal and mechanical load was larger than the one due to only mechanical load. If the stress induced by thermal and mechanical load is assumed to be a linear superposition of the stresses induced only by thermal and only by mechanical loads it turns out that the axial stress in the pile at the end of heating cycle is larger than stress induced by the axial compressive force applied at the pile head. The axial displacement, axial strain and stress in the pile depend on the soil layering and the types of soil present at the site. The heating and cooling cycles did not affect the pore pressure and effective stress in the surrounding soil.

Knellwolf et al. (2011) presented a new method of geotechnical analysis of HEP. This method is based on a one dimensional finite difference model that considers the shear stress at the soil-pile interface and the normal stress at the pile tip. The relationships between the shaft friction and shaft displacement, and tip stress and tip displacement are known. Knellwolf et al. (2011) introduced a degree of freedom of pile (n), which was defined as

$$n = \frac{\varepsilon_{th,o}}{\varepsilon_{th,f}} \tag{2.1}$$

where $\varepsilon_{th,f} = \alpha \Delta T$ is so called free thermal strain while ($\varepsilon_{th,o}$) is the observed axial strain, α is the coefficient of thermal expansion, ΔT is the net change in temperature. The latter is smaller than the free thermal strain since the pile is prevented from freely moving by the shear stress acting at the pile-soil interface. The axial stress is induced by the difference between the observed and free strain, which is given by:

$$\varepsilon_{th,d} = (n-1)\varepsilon_{th,f} \tag{2.2}$$

This in turn gives the following expression for the thermally induced axial stress:

$$\sigma_{th} = \varepsilon_{th,d} E_{pile} = (n-1)\alpha \Delta T E_{pile} \tag{2.3}$$

in which (E_{pile}) is the Young's modulus of the reinforced concrete pile. Knellwolf at el. (2011) neglected the self-weight of the pile in their analysis. Furthermore, the coefficient of thermal expansion of the pile (α) and its Young's modulus (E_{pile}) were not affected by the temperature and were constant along the pile length.

They concluded that the heating of the pile induced the additional compressive stresses in the pile and increased the mobilized shear stress. Furthermore, the cooling can release the shear stress mobilized during heating, thus possibly reversing the direction of the shear stress and perhaps even to a tensile stress in the pile.

Mimouni and Laloui, (2013) conducted investigation the impact of temperature difference on the mobilized bearing capacities of the energy piles. Their research was based on the load-transfer approach proposed by Seed and Reese, (1957) and Coyle and Reese, (1966) to estimate the bearing capacities of piles. The EPFL and Lambeth College test piles are modelled and analyzed in order to compare the results with the in situ tests data.

From the Menard pressuremeter modulus E_M, the slopes K_s and K_b of the first linear branch of the load-transfer curve shown in the Figure 2.2 are given by

$$K_s = \frac{2E_M}{D} \tag{2.4}$$

and $$K_b = \frac{11E_M}{D} \tag{2.5}$$

where D is the pile diameter.

Figure 2.2 Load-transfer curves used for (Mimouni and Laloui, 2013)

(a) shaft friction (b) base compression

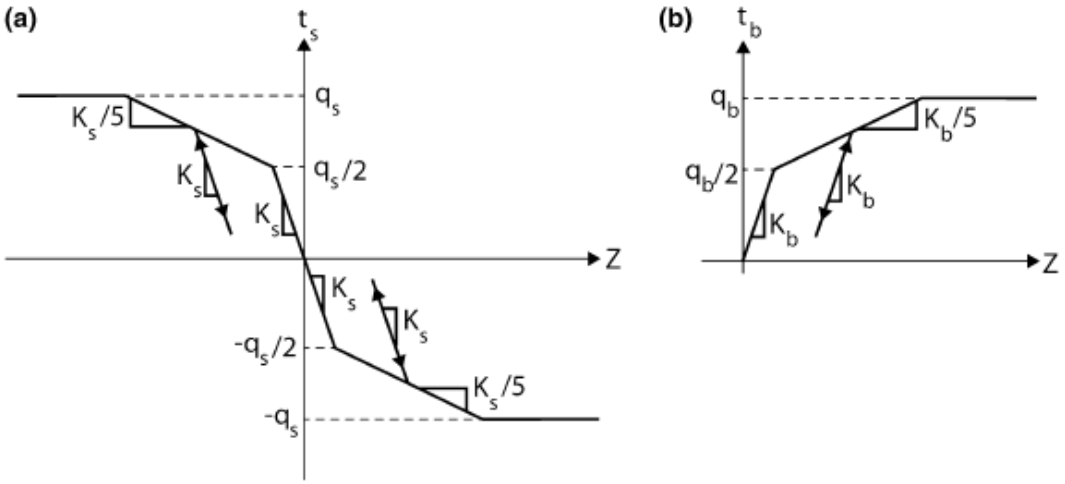

The ultimate bearing capacities consist of the ultimate shaft friction ($Q_{s,ult}$) and ultimate end bearing ($Q_{b,ult}$), which are given by

$$Q_{s,ult} = \pi D \int_0^L q_s dz \tag{2.6}$$

$$Q_{b,ult} = \frac{\pi D^2}{4} q_b \tag{2.7}$$

In the case of pile is subjected to a mechanical load (P), the head action (Q_h) include of the mechanical load (P) and the head reaction. It is given by

$$Q_h = P + \frac{\pi D^2}{4} K_h z_h \tag{2.8}$$

where K_h is the head stiffness and z_h is the head displacement of the pile. Figure 2.3 is the schematic of forces acting on a pile foundation.

They concluded that the mobilized bearing capacities of energy piles vary with temperature. This does not cause any geotechnical failure because the null point still exists during the thermal changes. Moreover, they found that increasing the factor safety of the HEP can raise the costs of the project, but it does not provide any advantages.

Figure 2.3 Schematic of forces acting on a pile foundation (Mimouni and Laloui, 2013)

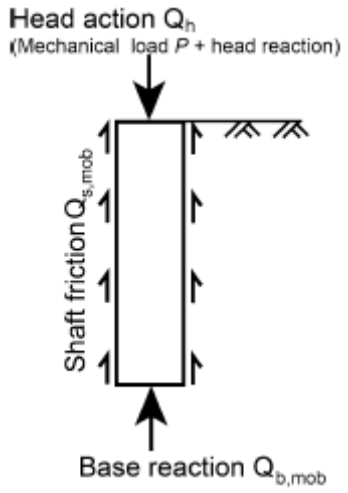

2.1.2 Bourne-Webb et al. (2009)

Bourne-Webb et al. (2009) presented the data collected during the field tests on the energy piles located at the Lambeth College in London. These field tests were designed to investigate the behavior of energy piles subjected to thermal, and combined thermal and mechanical loads. The pile head displacement, temperature and strain along the pile were recorded during the initial mechanical loading, at the end of first cooling period as well as at the end of the first heating period. The instruments used to record these data are optical fiber sensors, vibrating wire strain gauges and thermistors. Specifically, 18 vibrating wire strain gauges, six thermistors and five LVDTs and a load cell were recording continuously. The measurements provided basis for determination of the axial stresses in the pile.

The upper part of the test pile has the diameter of 0.61 m, while the diameter of the lower part is 0.55 m. The total length of the test pile is equal to 23 m. It was designed to carry the vertical force of 1200 kN as the working load. The temperature applied to the pile varied from the extreme values of –6^{o}C to 56^{o}C.

Bourne-Webb et al. (2009) concluded that in the thermodynamic design of the ground source heat pump system the pile acts as an infinitely long line source. It will emit the temperature in all directions. They concluded that the additional stresses in the pile that were induced due to the mechanical loading while the pile is heated could exceed the limiting value imposed by the design codes. They also found that the shear stresses mobilized at the pile/soil interface will significantly affect to the overall bearing capacity of energy piles.

Figure 2.4 Soil profile and instrumentation of the Lambeth College pile test (Bourne-Webb et al. 2009)

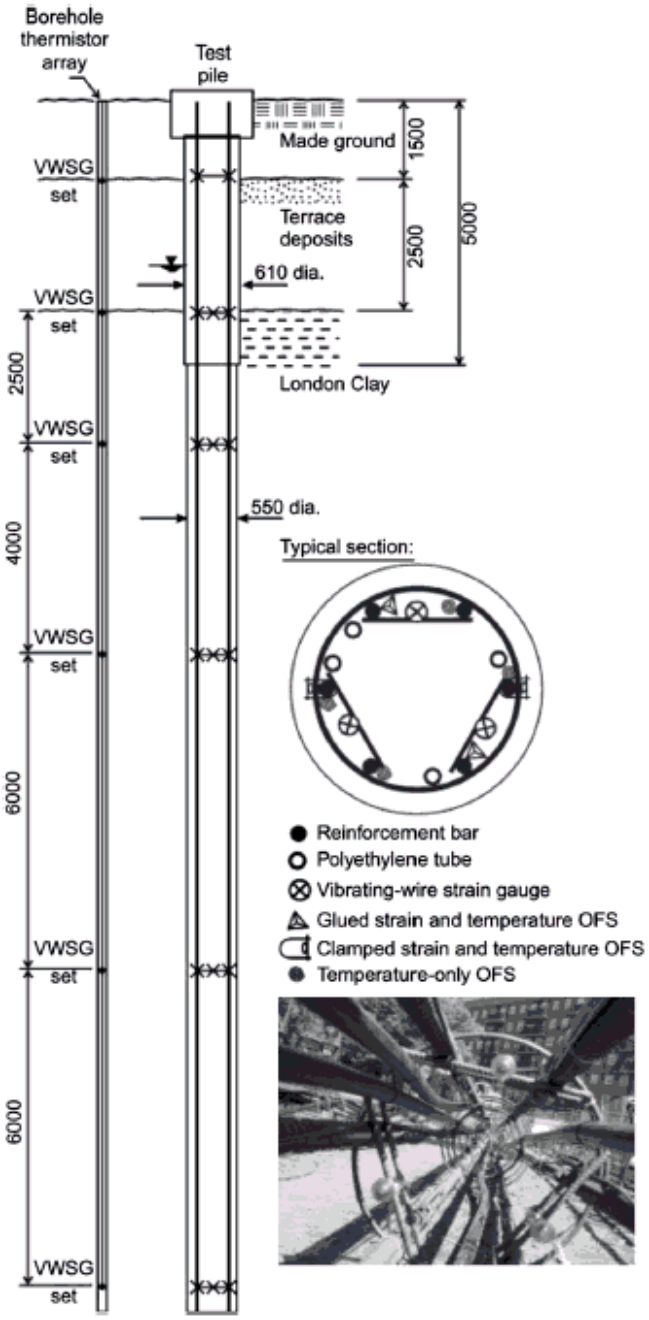

Additionally, Bourne-Webb et al. (2009) developed a simple descriptive framework for understanding the load-transfer mechanism and the behavior of energy piles under thermal, and mechanical and thermal loading.

2.1.3 Amatya et al. (2012)

Amatya et al. (2012) synthesized the published pile test results that involve three different sites. They developed simplified load transfer mechanisms for thermal, and combined thermal and mechanical loads for a single pile. Specifically, they focused on the change in axial stress, mobilized shaft friction, and effects of end restraints.

One of the field tests took place at the Lambeth College in South London (Figure 2.4). Two piles were constructed at the site, a 23 m long test pile and 30 m long heat sink pile. The mechanical load was applied to the test pile first. It was maintained for 46 days. The test pile was subsequently cooled for 31 days, which was followed by heating for 12 days. Finally, the pile was heated and cooled in daily cycles lasting three days.

The second test site was located in Lausanne (Switzerland). This is the field test described in the previous section. The location of the third filed test was Bad Schallerbach, Austria. The pile has a diameter of 1.2 m and the length of 9 m.

Figure 2.5 Soil profile of the Bad Schallerbach pile test (Amatya et al. 2012)

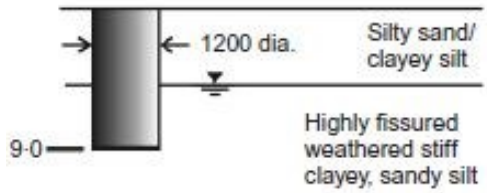

Amatya et al. (2012) concluded that heating and cooling of the piles induced the axial stress inside the pile, which was between about 50% and 100% of the theoretically fully restrained values. Although they found that stiffer soils seem to exhibit larger mobilization of shaft resistance they also indicated that methods for estimation of these effects needed to be developed. Finally, they stated that the heating and cooling of energy piles are not likely to have detrimental effects on buildings.

2.1.4 Suryatriyastuti et al. (2012)

Suryatriyastuti et al. (2012) used finite difference code FLAC^{3D} to simulate an energy pile under static loading. They used two different computational models: one with perfectly rough contact and the other with sliding contact along the soil-pile interface. The pile was 15 m

long and it has 0.6 m x 0.6 m square cross section. It was installed into the homogeneous soil. Both pile and soil were assumed to behave as the thermo-elastic materials. The domain was 15 m in wide and 30m in high. The pile was heated to 25^{o}C and subsequently cooled to 5^{o}C.

Figure 2.6 Finite difference model for an energy pile (Suryatriyastuti et al. 2012)

(a) Perfect contact (b) Sliding contact

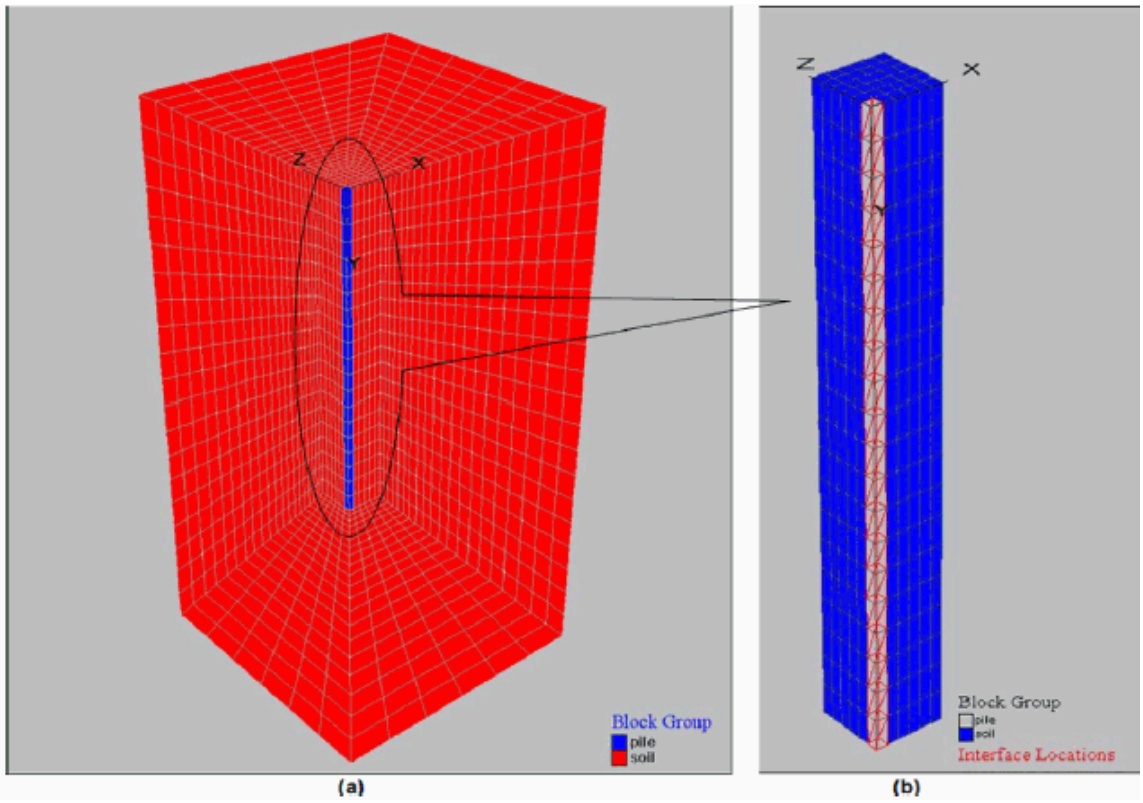

Suryatriyastuti et al. (2012) concluded that:

1. The stresses and displacement of the pile obtained from the model with the sliding contact are smaller than those obtained from the perfect contact.

2. During the cooling cycle the surface's settlement occurred and tensile forces developed in the pile. Opposite responses of the pile were found during the heating cycle.

3. Negative skin friction at the soil-pile interface was created for higher temperature differences.

4. Null point was located in the middle of the pile.

2.2 Geothermal Energy In The United States

2.2.1 Brettmann et al. (2013) and Sutman et al. (2014)

Brettmann et al. (2013) and Sutman et al. (2014) presented the results of the field tests on energy piles that were conducted in Richmond, Texas. The goal of this test was to investigate the long term thermal-mechanical behavior of the energy piles and evaluate the effects on the bearing capacity of the pile. Three 0.457 m diameter auger pressure grouted energy piles were installed in the soil profile that consisted of a top 9 m thick layer of stiff clay underlain by 9 m thick dense sand. Two of the piles (TP-1 and TP-3) were 15 m long and the third TP-2 was 9 m long. The fiber optic lines were installed in the center of the pile in order to measure both strain and temperature. Vibrating wire piezometers and thermistors were also installed in soil near each pile test. Figure 2.7 depicted the schematic layout of the test.

Figure 2.7 Schematic layout of the field test on energy pile (Sutman et al. 2014)

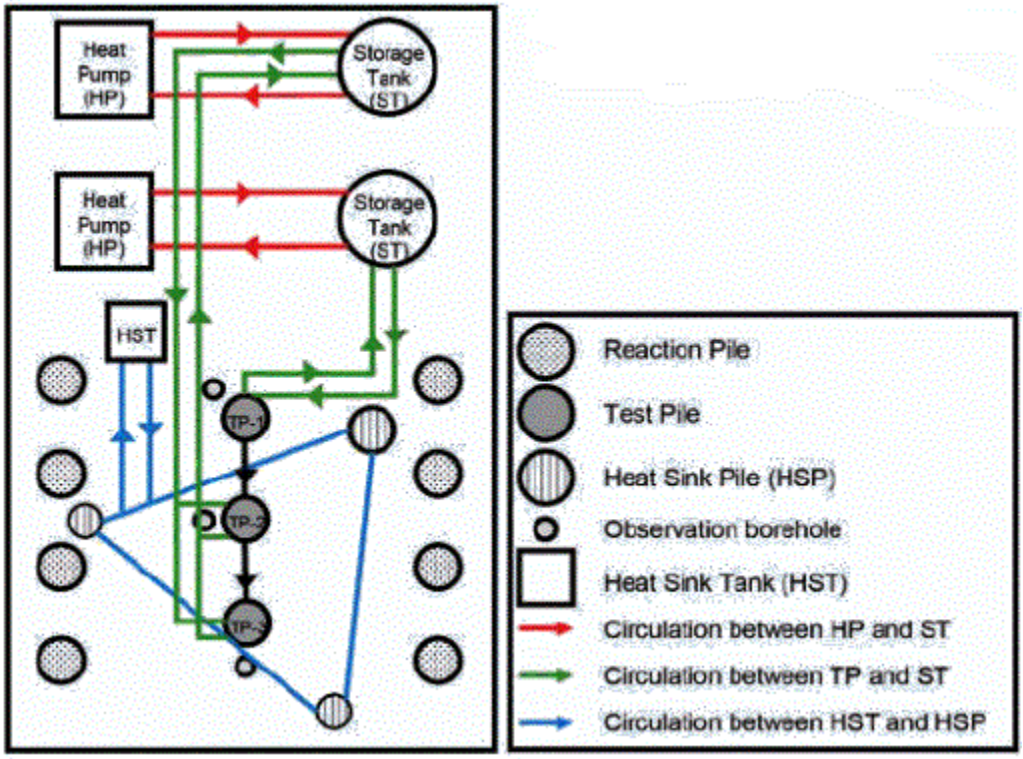

TP-2 represents the floating pile while TP-1 and TP-3 represent for end bearing piles. In TP-1, the mechanical load of 287.5 tons or 2,558 kN was applied first in order to find the ultimate bearing capacity. The pile was subsequently unloaded before applying five heating and

cooling cycles. During thermal loading, the temperature of the heat exchange fluid was increased to a maximum of 43°C and decreased to a minimum temperature of 8°C. The pile was subsequently loaded to failure. Figure 2.8 show the temperature cycles imposed on the piles.

Figure 2.8 Temperature imposed on the energy piles (Sutman et al. 2014)

(a) TP-1 (b) TP-3

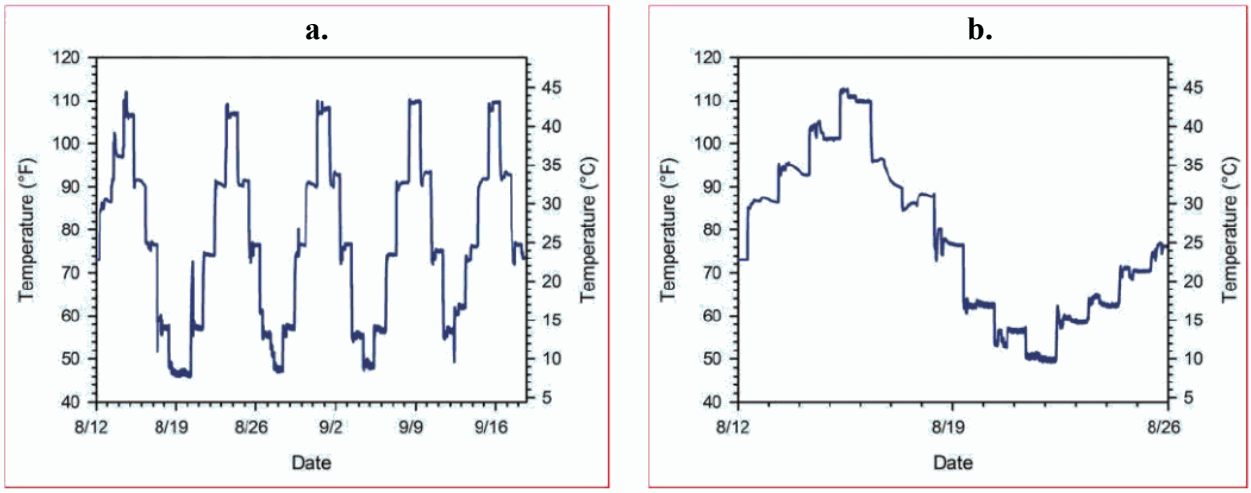

For TP-2 and TP-3, a single thermal cycle was applied for two weeks. The maximum temperature was 45°C and the minimum temperature was 8°C. The design load of 287.5 tons (2,558 kN) was applied on these two piles before the thermal loading stage and it was kept during this stage. Some of the first results of this research are presented in Figure 2.9.

In the TP-1 test, before thermal cycles, the deflection of the pile of 20.3 mm was recorded at the maximum load before thermal cycles were applied. After the thermal cycles, the deflection of the pile was 26.67 mm. Thus, the thermal induced an increase of 6.35 mm in the displacement of the pile.

During the TP-3 test, the deflection of the pile after thermal loading was around 0.65 in (16.5 mm) at the maximum loading. The computational modelling will need to be carried out in the future of the long-term thermal-mechanical behavior and performance of these energy piles.

Figure 2.9 Displacement and load of the pile before and after thermal cycles (Sutman et al. 2014)

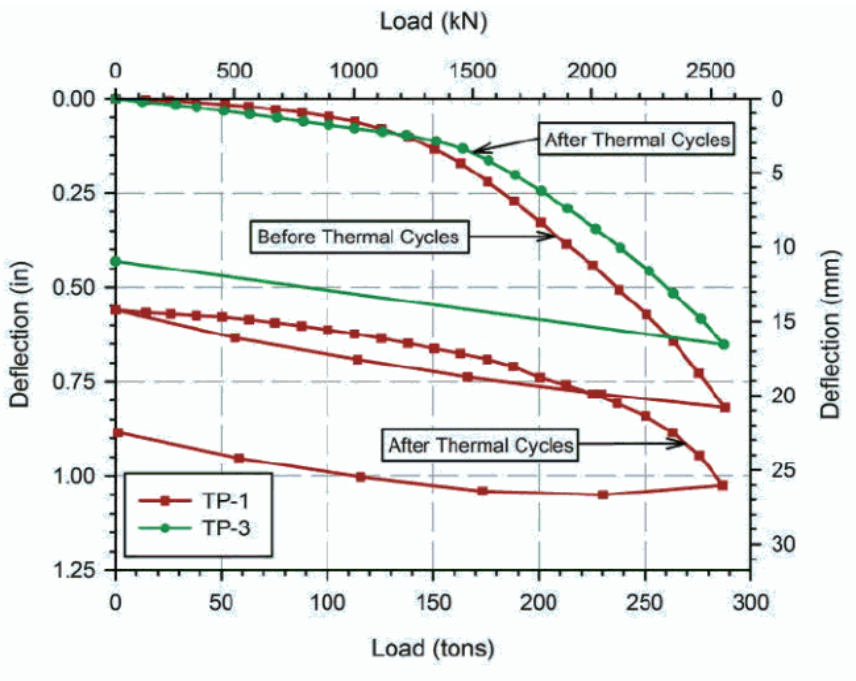

2.2.2 Murphy et al. (2014)

Murphy et al. (2014) performed the field tests on piles that supported the one story building at the US Air Force Academy. Eight drilled shafts of 0.61 m in diameter and 15.2 m in length were constructed to support the building. Three of them (foundation 1, 3 and 4) were instrumented with the strain gauges and thermistors to measure the strain and the temperature distribution during the heating and cooling cycles. The soil profile consist of a 1 m thick sandy fill, followed by the 1 m thick dense sand, which is underlain by the sandstone layer extending to the maximum depth explored. The 0.91 m in depth and 0.61 m in wide grade beam was placed on the top of the drilled shaft and around the perimeter of the building. Figure 2.10 is presented the location of the foundation.

Figure 2.10 Locations of the energy foundations (Murphy et al. 2014)

(a) Plan view of the building (b) Grade beam (c) Heat exchange system

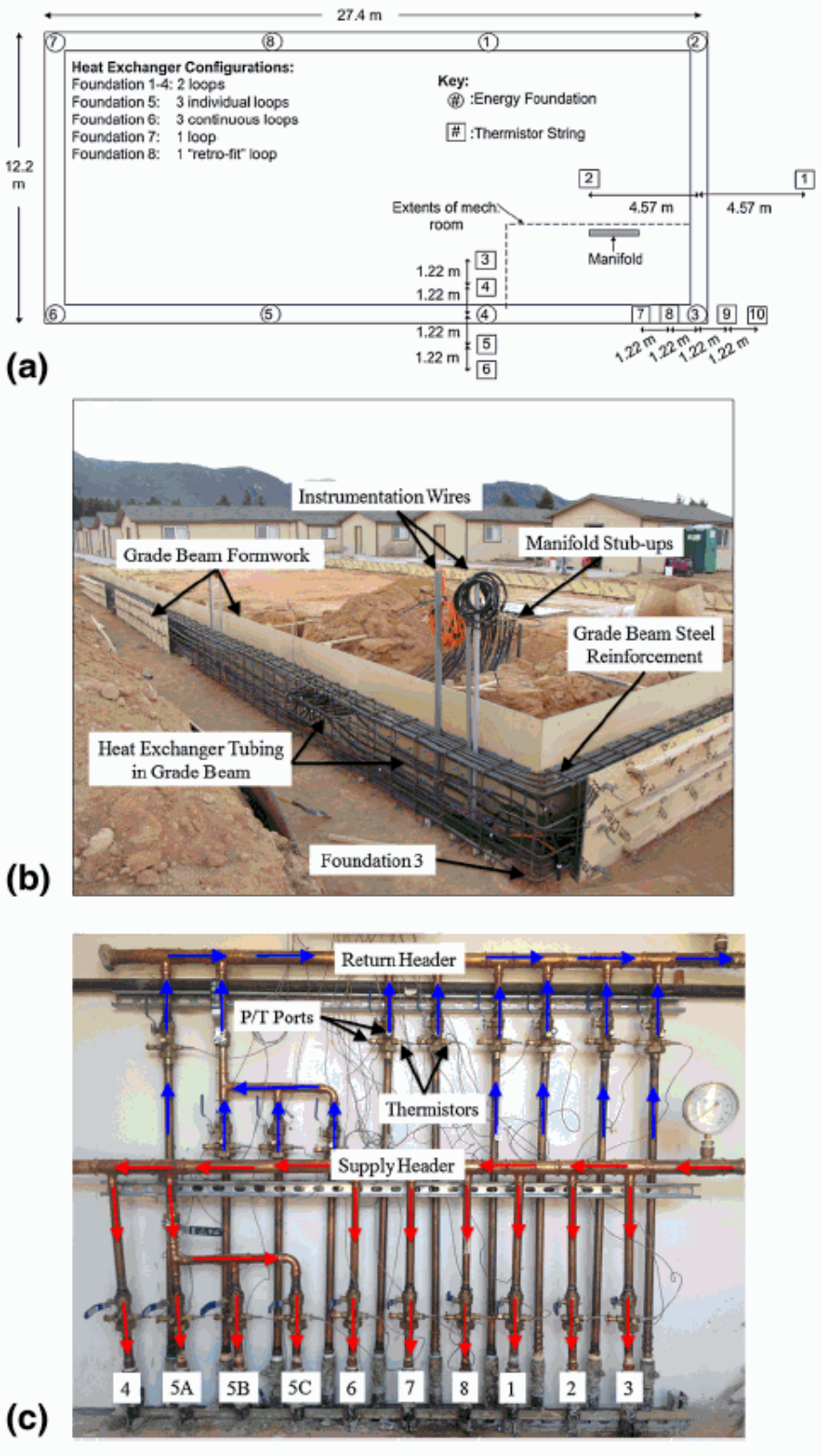

The temperature distributions at different depths of foundations 1, 3 and 4 are shown in Figure 2.11. The lowest temperature was recorded at the bottom of the foundations.

Figure 2.11 Foundations temperatures during the tests (Murphy et al. 2014)

(a) Foundation 1 (b) Foundation 3 (c) Foundation 4

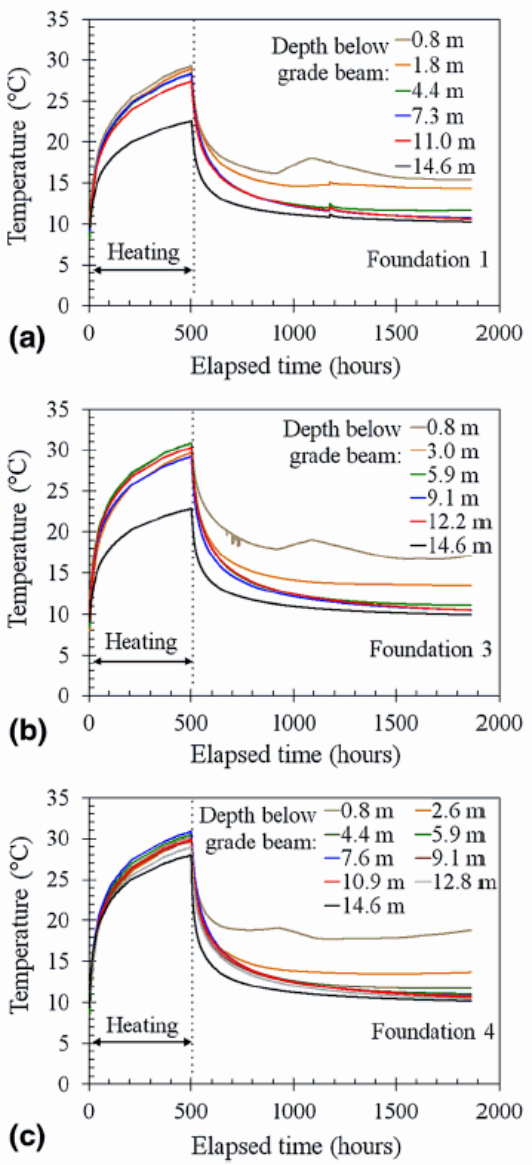

The axial strain, ε measured by the vibrating wire strain gauge can be calculated from

$$\varepsilon = -Gf^2 \tag{2.4}$$

where $G = 3.304 \times 10^{-3}$ is the gauge factor and f is the resonant frequency. Therefore, the strain induced by the thermal load, (ε_T) was calculated as follows

$$\varepsilon_T = [(\varepsilon_i - \varepsilon_o)B + \alpha_s \Delta T] \quad (2.5)$$

where $B = 0.975$ was the calibration factor; ε_i, ε_o were the axial strains measured at time i and at the initial stage, respectively. ΔT is the change in temperature and $\alpha_s = -12.2\ \mu\varepsilon/^oC$ is the coefficient of thermal expansion of the gauge. During the heating period, the thermal strain is negative, indicating that the foundation expanded, as in Figure 2.12.

Figure 2.12 Thermal axial strain during heating and cooling cycles (Murphy et al. 2014)

(a) Foundation 1 (b) Foundation 3 (c) Foundation 4

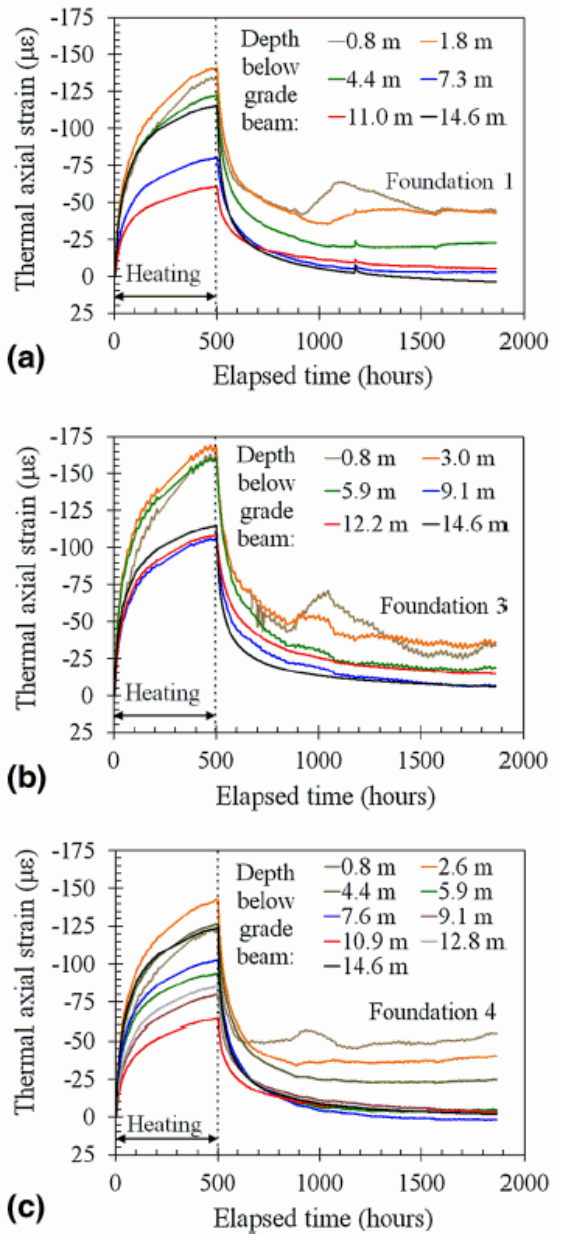

Figure 2.13 Thermal axial strain versus depth at different temperature (Murphy et al. 2014)

(a) Foundation 1 (b) Foundation 3 (c) Foundation 4

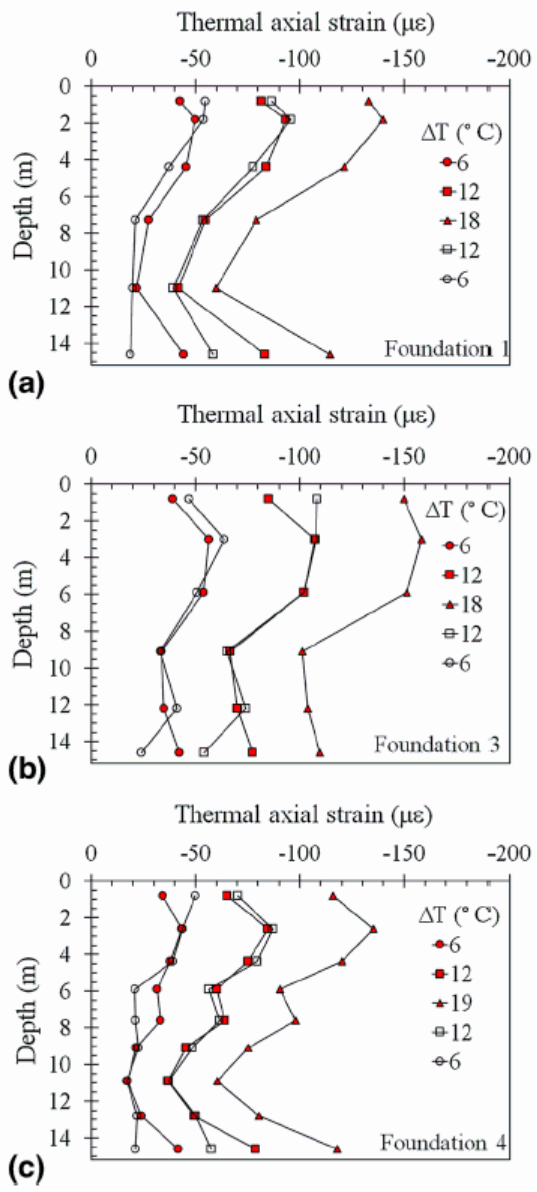

The thermal axial strain was not constant with depth because of the mobilization of the skin friction (Figure 2.13). Similarly to the measurements recorded by Laloui et al. (2006) and Bourne-Webb et al. (2009). Moreover, the strains at the head and toe of the foundation were larger than at other locating, thus indicated that the sandstone at the toe may be soft. If the foundations were fully restrained, the maximum stress in the pile due to the temperature difference of 18^{o}C would be 6.58 MPa. However, thermal axial stress in the foundations 1, 3 and

4 were lower than this value, indicating that the piles were not completely restrained. The axial stresses increased with depth until around 11 m, after 11 m axial stresses decreased. The maximum stresses are about 33% of the compressive strength of the reinforced concrete used in this study ($f_c^{'} = 21\,\text{MPa}$). Figure 2.14 shows the thermal axial stress versus depth in foundations 1, 3 and 4 at different temperatures.

Figure 2.14 Thermal axial stress versus depth at different temperature (Murphy et al. 2014)

(a) Foundation 1 (b) Foundation 3 (c) Foundation 4

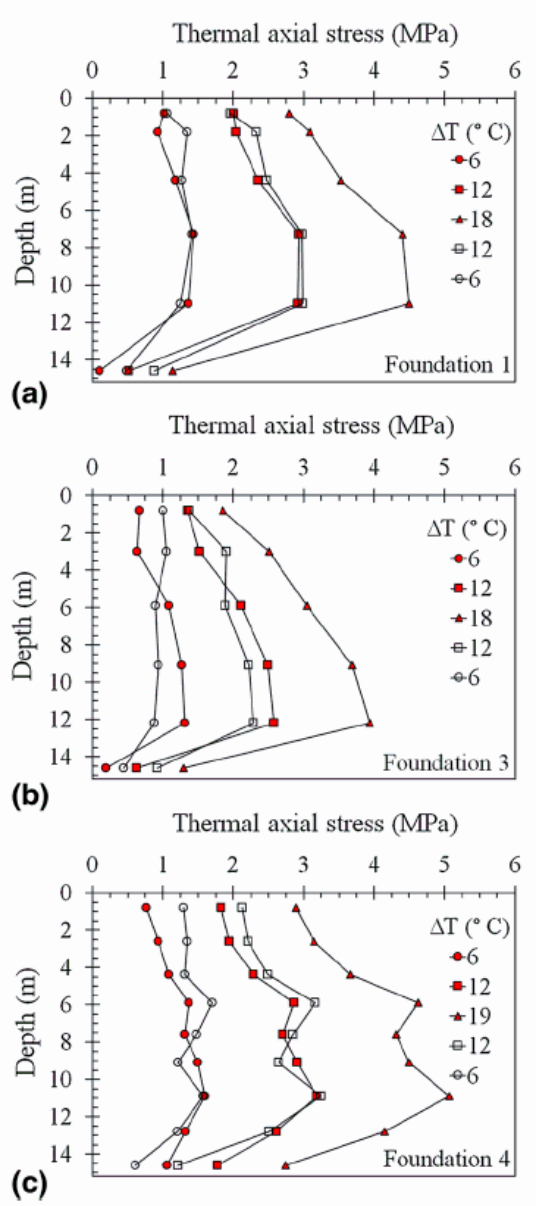

The shear stress resistance induced by the temperature can be calculated from the thermal axial stress, σ_T as

$$f_{s,mob,j} = \frac{(\sigma_{T,j} - \sigma_{T,j-1})D}{4\Delta l} \tag{2.6}$$

where D is the diameter of the pile and Δl is the space between the gauges. In Figure 2.15, the mobilized shear stress is smaller than 150 kPa because of the weakness sandstone layer. The skin friction was negative in the upper part and positive in the lower part of the pile.

Figure 2.15 Shear stress versus depth at ΔT = 18°C (Murphy et al. 2014)

(a) Foundation 1 (b) Foundation 3 (c) Foundation 4

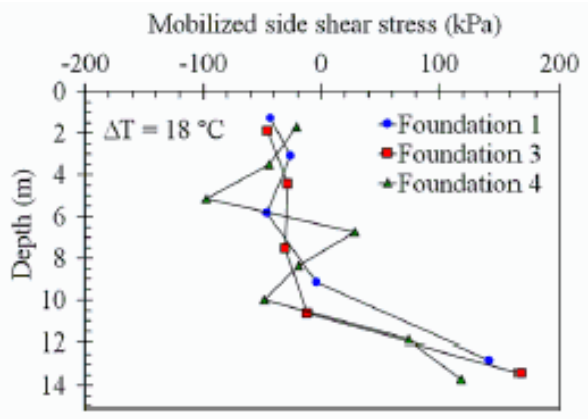

Assuming the pile toe was not moved, the relative thermal axial displacement due to thermal calculated as follows

$$\delta_{T,i} = \delta_{T,i-1} + \frac{1}{2}(\varepsilon_{T,i-1} + \varepsilon_{T,i})\Delta l \tag{2.7}$$

where $\delta_{T,i}$ is the thermal axial displacement at the midpoint between gauges, $\varepsilon_{T,i}$ is the thermal axial strain at the location of gauge i. The vertical head displacement of the foundation was from –1.3 to –1.7 mm for the maximum temperature imposed on the foundation as in Figure 2.16. This displacement was not affected the operation of the building.

Figure 2.16 Thermal axial displacement at different temperature (Murphy et al. 2014)

(a) Foundation 1 (b) Foundation 3 (c) Foundation 4

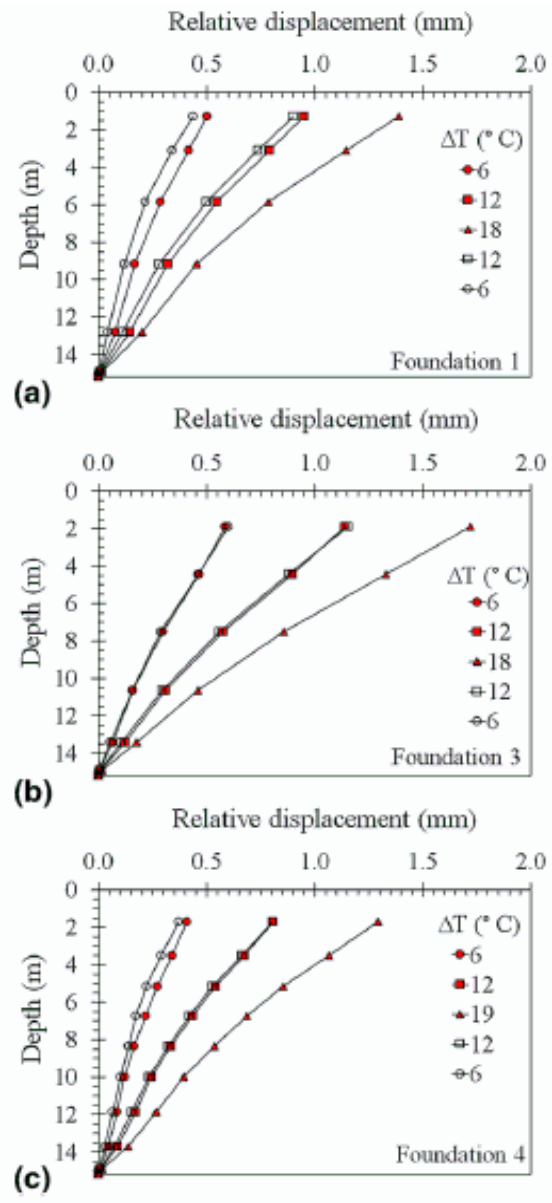

The significant conclusions resulting from this study are:

1. The temperatures in the foundations 1, 3 and 4 were constant with depth, except on the top due to the effect of the surface temperature and at the bottom due to the present of the sandstone.

2. The thermal axial strains induced in piles by the temperature change were smaller than the predicted free expansion strain.

3. Maximum thermally induced compressive stress ranged from 4 to 5.1 MPa at the depth between 11 and 12 m.

4. The thermal axial displacement was not affected by the operation of the building. The vertical head displacement of the foundation ranged from –1.3 to –1.7 mm for the maximum temperature imposed on the foundation while the pile toe was assumed to be restrained.

5. The thermal-plastic deformations did not occur along the foundation-subsurface interface.

Chapter 3 - Heat transfer in soils

3.1 Introduction

In general, heat transfer occurs when the temperature differences exist between two locations. The heat flows from warmer to cooler region. Heat transfer in soils plays a significant role in many engineering problems. Thus, understanding the thermal behavior of soils is helpful for solving these problems. The three mechanisms of heat transfer in soils are conduction, convection and radiation.

Conduction is the transfer of heat that is accomplished by colliding of hotter molecules with cooler molecules. When heat is transferred through conduction, the substance itself does not flow. The heat is rather transferred internally by vibrations of atoms and molecules. Electrons can also carry heat, which is the reason metals are generally very good heat conductors. Metals have many free electrons, which move around randomly. These electrons can easily transfer heat from one part of the metal to another. The amount of heat transfer by true conduction increases with increases in both, a dry density and degree of saturation of a soil.

The basic law of thermal conduction is the Fourier's law which states that the heat flux q (W/m^2) is proportional to the temperature gradient T ($^oC/m$, $°K/m$). It is described by the following equation

$$q = -\lambda \frac{dT}{dz} \tag{3.1}$$

where λ is the thermal conductivity (W/m/°K). The minus sign indicates that the temperature decreases in the direction of heat transport and, hence, the temperature gradient is a negative quantity.

Convection is the movement of heat in the fluid that is caused by temperature differences. Hotter fluid moves away from the source due to a decrease of density and it is replaced by the cooler denser fluid. While free convection is due to the fact that hotter fluids are less dense than cooler fluids, forced convection does not depend on density differences. In this case the fluid motion is forced an external source such like a pump or other mechanical devices.

Radiation is the heat transfer by electromagnetic waves. Heat is transferred from one particle to another through waves that are generated by the hotter particle through its vibration.

Figure 3.1 shows the various mechanisms of heat transfer in soils as they relate to the grain size and degree of saturation. Thus, according to the Figure 3.1 the main mechanism of heat transfer in soil is by conduction.

Figure 3.1 The various mechanisms of heat transfer in the ground as related to soil grain size and degree of saturation (Farouki, 1981)

1. Thermal redistribution of moisture 2. Vapor diffusion due to moisture gradients
3. Free convection in water 4. Free convection in air 5. Heat radiation
6. Heat conduction

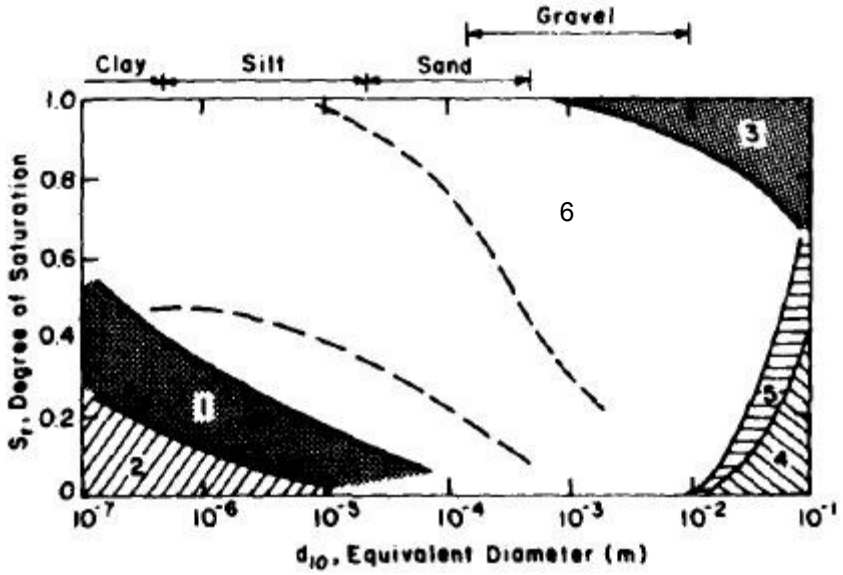

In Figure 3.2, below a depth of 10 – 15 m the ground temperature remains constant, which corresponds to the values between 10 – 15^{o}C in Europe and 20 – 25^{o}C in tropics. Both of these situations still permit economical heating and cooling of buildings by use of thermo–active foundations. Moreover, radiation effects decrease with depth.

Figure 3.2 Heat transfer mechanism and the distribution of temperature with depth (Brandl, 2006)

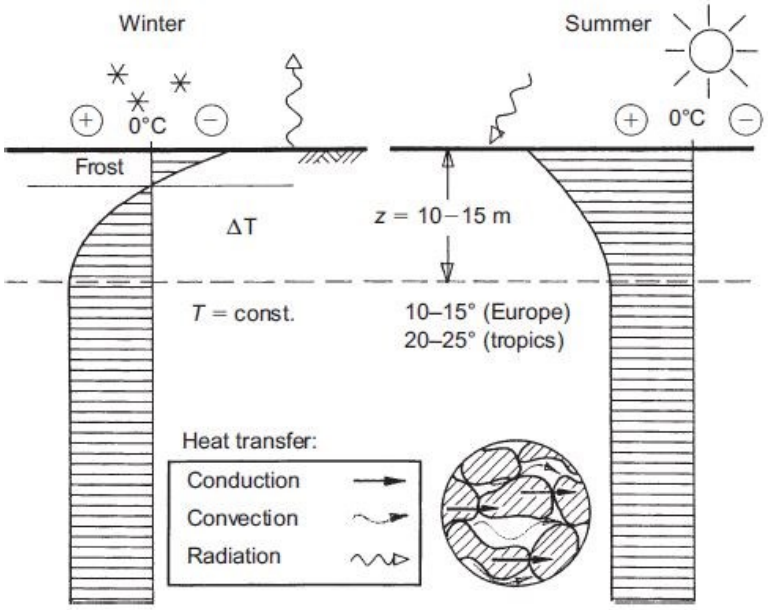

In the case of heat exchanger piles, Lee (2009) state that the main heat transfer mechanisms are conduction and convection as illustrated in Figure 3.3 below.

Figure 3.3 Heat transfer mechanism in HEP (Lee, 2009)

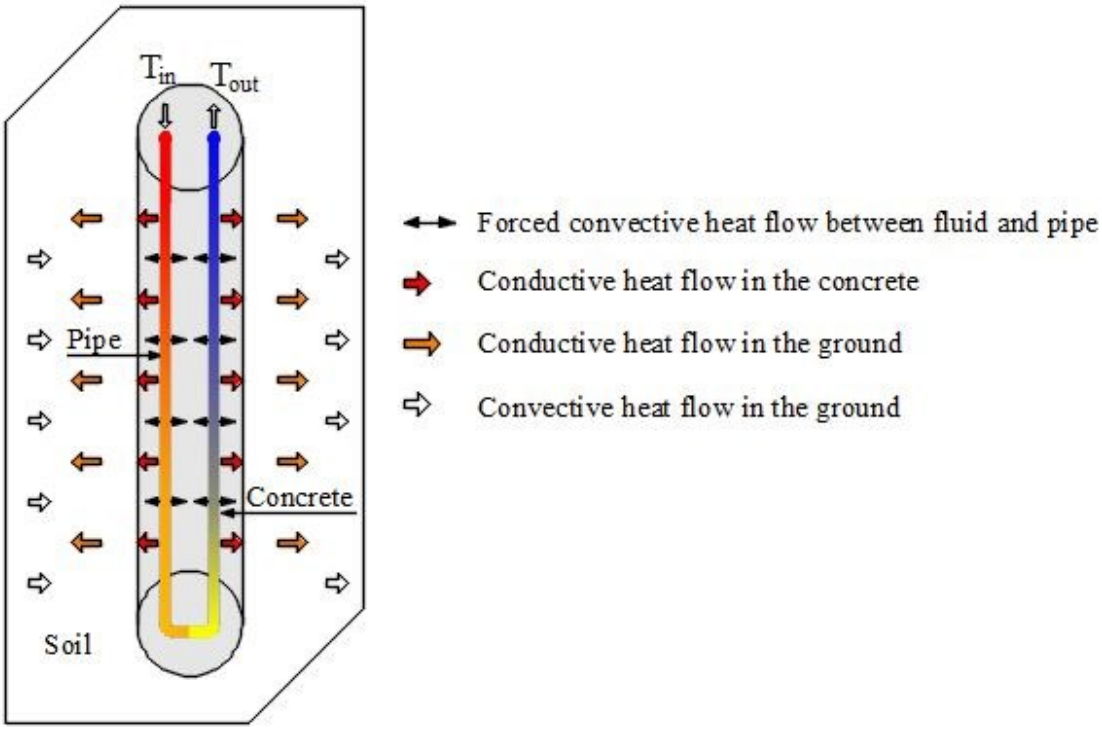

3.2 Thermal properties of soils

Soils react to thermal changes in the form of heating and/or cooling. Thermal properties of soils such as thermal conductivity, coefficient of thermal expansion and heat capacity influence the transfer of heat in a soil. These thermal properties depend on the type of soil, its water content and saturation, and its density. Table 3.1 shows typical values of thermal parameters for different types of soil minerals and other soil constituents.

The values of thermal conductivities for soils are much higher compared to the air and water. Thus, it is evident that the heat flow must be predominantly through the solids. The thermal conductivity λ, heat capacity C and density ρ of the soil are temperature dependent parameters.

Table 3.1 Thermal properties of some materials at 10°C and ice at 0°C (Van Wijk & De Vries, 1963)

Materials	Thermal conductivity, λ (mcal $cm^{-1}sec^{-1}\ ^oC^{-1}$)	Heat capacity, C (cal $cm^{-3}\ ^oC^{-1}$)	Density, ρ (g cm^{-3})
Quartz	21	0.48	2.66
Clay minerals	7	0.48	2.65
Organic matter	0.6	0.6	1.3
Water	1.37	1	1
Ice	5.2	0.45	0.92
Air	0.06	0.0003	0.00125

3.2.1 Thermal conductivity

The most important thermal soil parameter is its thermal conductivity λ ($Wm^{-1}{}^{\circ}K^{-1}$). It is defined as a quantity of heat transfer through unit area per unit time under a unit temperature gradient. Values of thermal conductivities of different soils are listed in Table 3.2.

Table 3.2 Thermal properties of different soils (Ghildyal and Tripathi, 1987)

Soil	Degree of Saturation (%)	Thermal Conductivity (mcal $cm^{-1}s^{-1}\ ^oC^{-1}$)	Thermal Diffusivity ($10^{-3}cm^2s^{-1}$)

Sand, wet	23	4.35	12.6
Sand, dry	-	0.35	1.5
Loam, wet	75	4.25	6.0
Loam, dry	-	0.45	1.8
Clay, wet	38	1.40	3.2
Clay, dry		0.25	1.5
Peat, wet	66.66	0.82	1.2
Peat, dry	-	0.11	1.3

Water has a higher thermal conductivity than air, a wet soil has a higher thermal conductivity than a dry soil. Thermal conductivity of soils increases when the degree of saturation or dry density increases.

The thermal conductivity is not always constant. The following are the main factors that influence the thermal conductivity of soils:

1) Mineralogy: Quartz has the highest thermal conductivity compared to other minerals, so quartz sands have higher conductivity than sands containing other minerals.
2) Dry density: Soils with a greater dry density generally have a greater thermal conductivity.
3) Gradation: Well graded soils transfer heat better than poorly graded soils because smaller sized particles can fit into the spaces between the larger sized particles, thus increasing the density and enhancing the particle to particle contacts.
4) Water content: Water has twenty times larger thermal conductivity than air and thus its presence in soil affects the thermal properties of soils. Consequently, dry soils have lower thermal conductivity than wet soils. Also, thermal conductivity increases with increased water content.

The relationship between thermal conductivity, and water content and dry density for saturated and unsaturated soils is shown in Figure 3.4. For the preliminary design of energy foundations, thermal conductivity can be estimated from the Figure 3.4.

Kersten, (1949) conducted tests on soils and crushed rock and gave the empirical equations for computing the thermal conductivities in terms of water content w (%) and dry

density ρ_d (g/cm^3). For coarse grained soils (silt and clay content < 20%), the thermal conductivities are given by

Unfrozen (+4°C) soils: $$\lambda = 0.1442(0.7\log w + 0.4)(10)^{0.6243\rho_d} \quad (3.2)$$

Frozen (-4°C) soils: $$\lambda = 0.01096(10)^{0.8116\rho_d} + 0.00461(10)^{0.9115\rho_d} w \quad (3.3)$$

For fine grained soil (50% or more silt and clay), the thermal conductivities are given by

Unfrozen soils: $$\lambda = 0.1442(0.9\log w - 0.2)(10)^{0.6243\rho_d} \quad (3.4)$$

Frozen soils: $$\lambda = 0.001442(10)^{1.373\rho_d} + 0.01226(10)^{0.4994\rho_d} w \quad (3.5)$$

3.2.2 Thermal expansion

The coefficient of thermal expansion α is defined as a change of length (*dL*) with respect to temperature change (*dT*), per unit length:

$$\alpha = \frac{1}{L_0}\frac{dL}{dT} = \frac{d\varepsilon}{dT} \quad (3.6)$$

where L_0 is the length at some reference temperature, $dL/L_0 = d\varepsilon$, and ε is the normal strain.

3.2.3 The heat capacity of soils

The heat capacity *C* (cal/cm^3 °C) of a soil sample is the amount of heat required to rise its temperature by 1°C. It is the product of the specific heat *c* (cal/g °C) and the density ρ (g/cm^3):

$$C = c\rho \quad (3.7)$$

Soil consists of different constituents, including solids, water, and air. The heat capacity of the soil can be computed expressed as:

$$C = C_s x_s + C_w x_w + C_a x_a \quad (3.8)$$

where x_s, x_w, x_a are the volume fractions, and C_s, C_w, C_a are the heat capacities of solids, water, and air, respectively.

From Table 3.1 above, the heat capacity of water is larger compared to the heat capacities of air and solids. The heat capacity of air can usually be neglected. By dividing the solid constituents into mineral and organic fractions Equation (3.5) simplifies to:

$$C = C_m x_m + C_o x_o + C_w x_w \quad (3.9)$$

where "*m*" indicates mineral constituents and "*o*" indicates organic constituents.

According to De Vries (1963), an average value of C_m of about 0.46 for soil minerals at 10°C and $C_o = 0.6$ for organic soils. Equation (3.5) then becomes:

$$C = 0.46x_m + 0.6x_o + (cal\ cm^{-3}\ ^oC^{-1})x_w \tag{3.10}$$

Figure 3.4 Thermal conductivity against dry density and water content for different soils (Brandl, 2006)

(a) coarse-grained soil, frozen (b) coarse-grained soil, unfrozen

(c) fine-grained soil, frozen (d) fine-grained soil, unfrozen

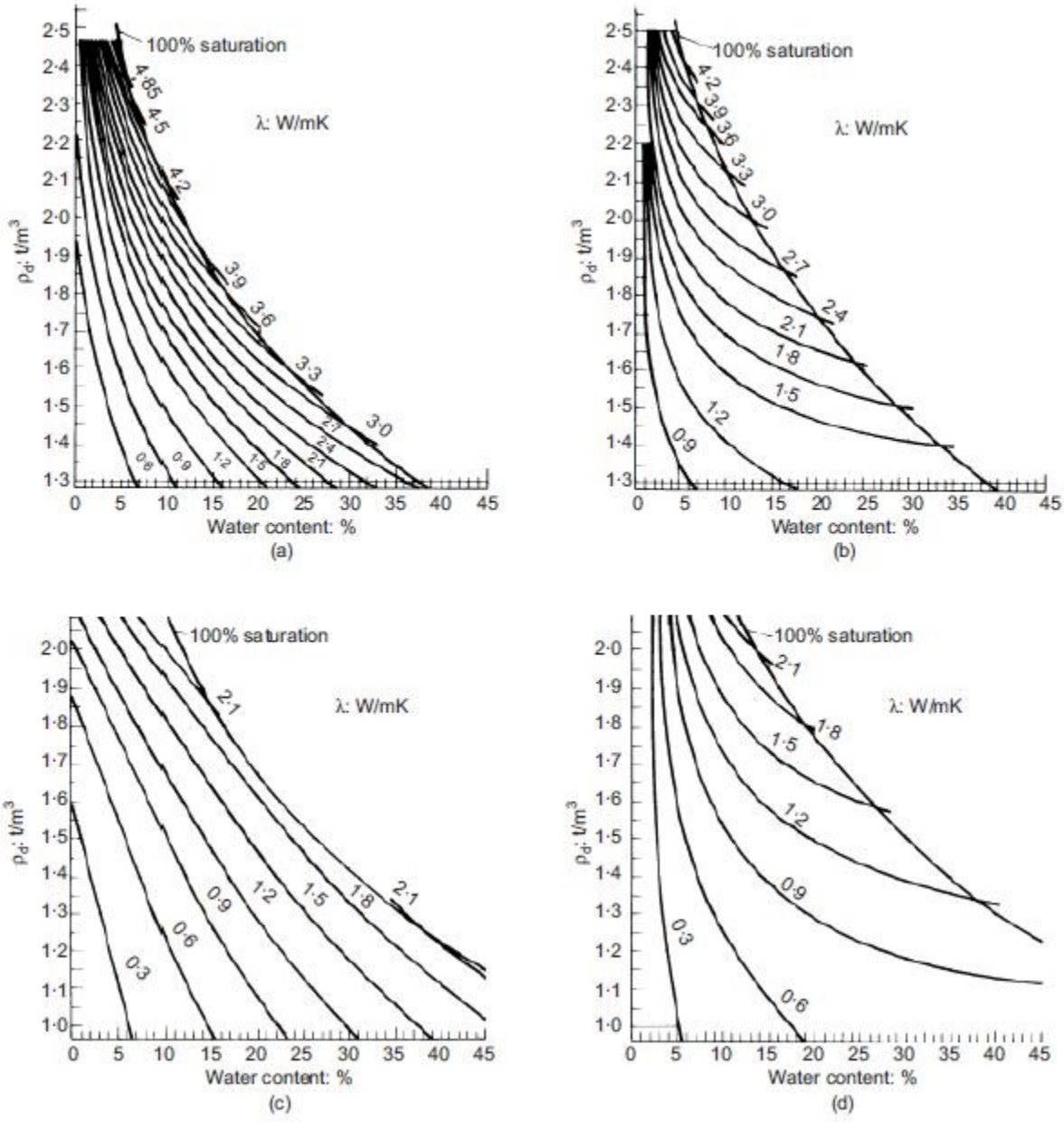

3.3 Thermal properties of rock

Rocks can be divided into four basic rock types according to mineral content or degree of metamorphosis: sedimentary, volcanic, plutonic, and metamorphic (Clauser, 2006). For sedimentary rocks (such as limestone, sandstone, shale and rock salt), thermal conductivity is controlled by porosity and sediment type. For volcanic rocks (such as basalt), porosity is the controlling factor on thermal conductivity. The two other rocks are generally much less porous. Therefore, the controlling factor is mainly by the mineral phase. For the plutonic rocks (such as granite) with high feldspar content have a low conductivity comparing to the one with low feldspar content. For metamorphic rocks (such as quartzites) quartz content controls thermal conductivity. Low quartz content rocks towards to have low conductivity. The other factors that influence the thermal conductivity of rock are:

Pressure: When the overburden pressure is increased, fractures and micro-cracks begin to close that reduces thermal contact resistance as well as porosity.

Partial saturation: a rapid increase in conductivity with increasing saturation.

Anisotropy: Thermal conductivity of sedimentary and metamorphic rocks is often anisotropic due to the conditions of their formation.

Table 3.3 is illustrated the thermal conductivity and heat capacity of different rock types.

Table 3.3 Thermal properties of different rock types (Sundberg, 1988)

Rock type	Specific heat (J/kg/K)	Thermal Conductivity (W/m K)
Sandstone (Mesozoic)	2000 – 950	2.3 – 4.5
Sandstone (Cambro-silur)	1000 – 900	4.0 – 6.0
Sandstone (Pre-cambrium)	1000 – 850	4.0 – 6.5
Shale (Mesozoic)	2200 – 1100	1.5 – 3.0
Shale (Cambro-silur)	1600 – 950	2.0 – 3.5
Limestone (Mesozoic)	2200 – 950	1.5 – 2.8
Limestone (Cambro-silur)	1150 – 850	2.8 – 3.3
Granite		2.85 – 4.15
Granodiorite		2.85 – 3.85
Quartite		5.35 – 8.10

According to Richter and Simmons, (1974) thermal expansion of rock depends on the heating rates, previous maximum temperatures, mineralogical composition, the initial porosity of the rock, and crystal orientation. Table 3.4 shows the coefficient of thermal expansion for different rock types.

Table 3.4 Thermal expansion of some rocks (after Berest and Vouille, 1988)

Rock types	Thermal expansion, α (10^{-6}/K)
Basalt	5.4
Lime stone	2.5 – 20
Granite	7.5 – 9
Sand stone	10
Marble	5.4 – 7
Salt	40

Chapter 4 - Computational modeling

4.1 Introduction

In geotechnical engineering computational modelling is the important tool for solving many problems encountered in the practice including evaluation of slope stability, analyzing groundwater seepage, predicting displacements, stresses and strains around excavations, under buildings, roads and railroads, as well as around tunnels.

Perhaps the most recent application of computational modeling in geomechanics is related to energy foundations. This most often requires a coupled thermal-hydro-mechanical analysis to be carried out, thus predicting distribution of stresses, strains, displacements and pore pressures in and around the energy piles. Before a particular computational method or approach can become widely accepted it needs to be validated and verified against the full scale field tests and possibly against analytical solutions if they are available.

To this end, the version 6.13-2 of ABAQUS/Standard has been used herein for the computational modelling task. ABAQUS/CAE (Complete Abaqus Environment) allows defining geometry, material properties, boundary conditions and generating a mesh in an interactive friendly environment. The output data can also be viewed in the CAE.

The Biot type model is used to arrive to fully-coupled equations that govern evolution of heat flow, solid displacement and pore pressure of a body subjected to mechanical, hydraulic and thermal loading. Equilibrium is governed by momentum conservation equation, which is given by

$$div\sigma_{ij} + b_i = 0 \tag{4.1}$$

where σ_{ij} is the total Cauchy stress tensor and b_i is body force. The effective stress tensor is given by Terzaghi's principle of effective stress as

$$\sigma_{ij} = \sigma'_{ij} - u\delta_{ij} \tag{4.2}$$

where δ_{ij} is the Kroenecker delta, u is the pore water pressure, which is positive in compression. The normal components of the effective stress tensor σ'_{ij} are negative in compression.

Mass conservation is described by a continuity equation

$$\frac{1}{Q}\left(\frac{\partial u}{\partial t}\right)-\frac{1}{Q_t}\left(\frac{\partial T}{\partial t}\right)+div(v_i^s)+div(v_i^{rf})=0 \tag{4.3}$$

where T is the temperature, v_i^s and v_i^{rf} are velocity of solid, and relative velocity of fluid with respect to solid.

$$Q=\frac{1}{n\beta_f+(1-n)\beta_s} \tag{4.4}$$

where β_f and β_s are the compressibilities of fluid and solid at constant temperature respectively, while n is the porosity. Q^t is given by

$$Q^t=\frac{1}{n\beta_f^t+(1-n)\beta_s^t} \tag{4.5}$$

where β_f^t and β_s^t are coefficients of thermal expansion of fluid and solid at constant temperature respectively. It is assumed that the temperatures of the fluid and solid are equal.

As stated by Laloui et al. (2006), in the case of HEP the heat convection might be neglected. Thus, the heat conduction takes the following form

$$\lambda div(gradT)=C\frac{\partial T}{\partial t} \tag{4.6}$$

It is noted that the temperature (T) can be solved independently from equation (4.6) because it is the only unknown function appearing in equation (4.6). The solid displacement and pore pressure are coupled through equation (4.1) and (4.3).

4.2 Case study

As pointed out earlier (Chapter 2) only few field tests involving HEPs are currently available. For the purpose of computational modeling field tests that were conducted on an end bearing HEP located in Lausanne, Switzerland were selected. A four story 100 m x 30 m building was constructed at the Swiss Federal Institute of Technology. It is supported by 97 drilled piers. The in situ test was conducted on a heat exchanger pile, which is located at the side of the building.

This site was selected for computational modeling due to abundance of the available experimental data. In addition to the experimental data collected during the full scale field tests

(Laloui et al. 2003; Laloui et al. 2006; Knellwolf et al. 2011), additional data from relevant laboratory tests are available as well (Laloui et al. 1999). Specifically, the availability of the results of conventional triaxial compression tests performed on samples extracted from few different depths enabled the computational model to produce a rather independent prediction from the field test results. Consequently, if the agreement between the response predicted independently by the computational model and the actual measured response is satisfactory then the former method is sound and acceptable.

A site investigation was performed in September 1997 (Laloui et al. 1999). Ground water table was located at the top surface of the soil. The soil profile that resulted from the field and lab investigations is depicted in Figure. 4.1 and it consists five different layers (Laloui et al. 2006), which are given as follows:

A1, A2: alluvial soil (soft clay) B: sandy gravel moraine (soft sandy, gravelly clay)

C: ground moraine (stiff sandy, gravelly clay) D: molasses (weak sandstones, shales)

Figure 4.1 Soil profile and the instrumentation of the tested pile (Laloui et al. 2006)

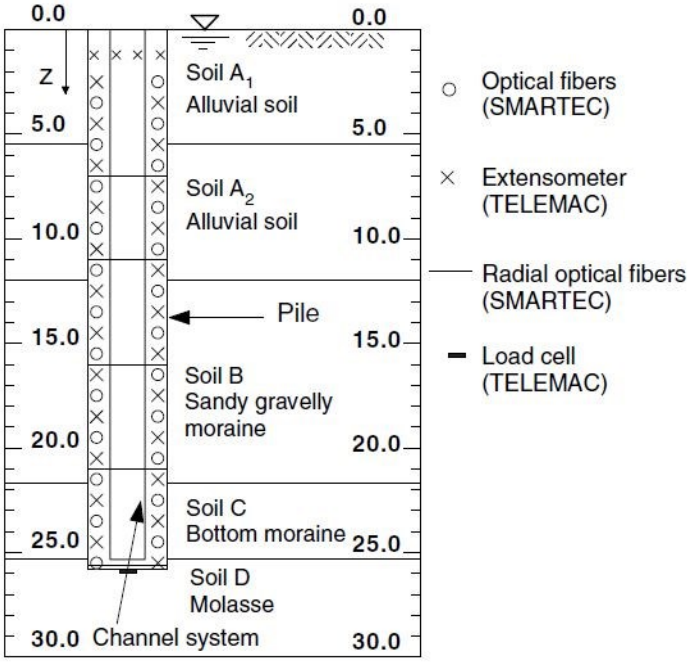

Based on ASTM D2487, the results from grain size distribution and Atterberg limit tests conducted on the samples taken from depth 12, 16, 20, 22, 25 and 26 m indicate these soils are lean clay (CL). Figure. 4.1 also indicates the instrumentation used to collect the data during the field tests.

4.2.1 Model Description

A coupled elastic thermo-hydro-mechanial finite element analyses were conducted for a single HEP. To this end, a 2D (axisymmetric) finite element (FE) model was created using the finite element software ABAQUS/CAE 6.13-2. Due to the symmetry of geometry, load and soil profile only a half of the longitudinal pile section with a radius of 0.5 m and a length of 26 m was modelled. The selected model size of 10 m x 52 m resulted from the size sensitivity studies. The FE model consists of a total of 6,489 nodes and 2,080 elements. The pile was modelled by using CAX8R: 8 node biquadratic axisymmetric quadrilateral elements. The soil was modelled by using CAX8RP: 8 node axisymmetric quadrilateral biquadratic displacement, bilinear pore pressure element. The contact between the pile and soil was assumed to be perfectly rough.

Figure 4.2 FE model and the boundary conditions of the Laussane HEP

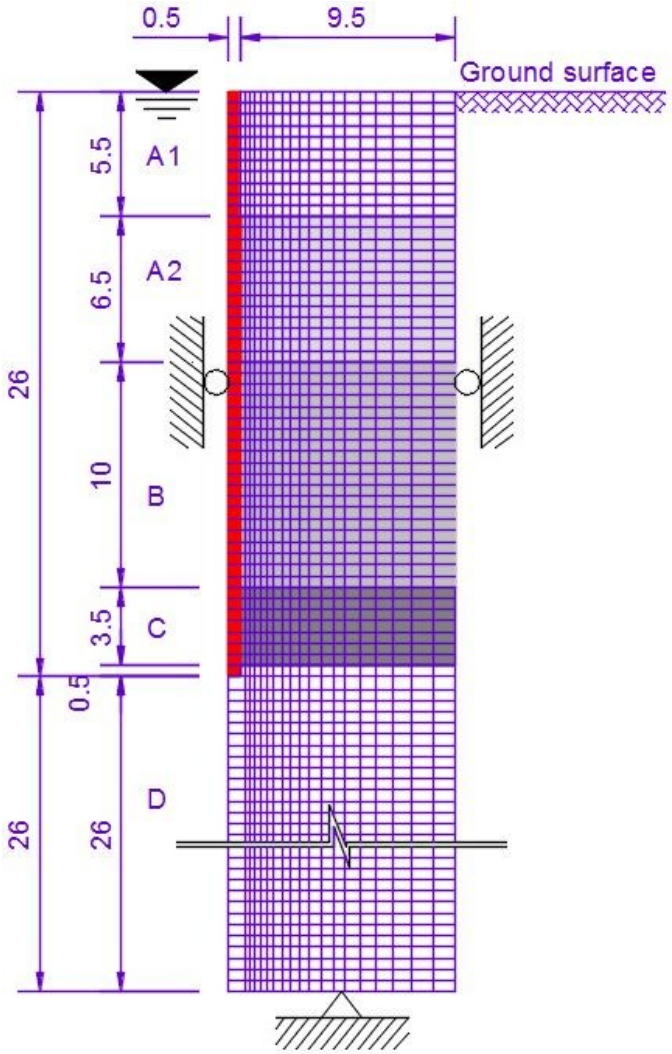

The motion in horizontal direction was not allowed along vertical boundaries and bottom side of the domain depicted in Figure 4.2. In addition, horizontal displacements were also prevented at the bottom side. Drainage was allowed at the top of the domain.

A temperature history was prescribed along the outer boundaries of the pile while a constant temperature was prescribed on the top soil surface. Heat flow was allowed to flow through the remaining part of the boundary.

Coupled thermal-hydro-mechanical analysis is performed in two runs. In the first run, the HEP was subjected to a thermal loading consisting only of a single heating/cooling cycle. This step captured the heat transfer from the pile into the surrounding soil. The end of the first run was taken as the initial condition for the second run, which comprised a coupled displacement-pore pressure (or hydro-mechanical) analysis, thus giving the stresses, strains and pore pressures induced by the thermal loading from the first run.

4.2.2 Temperature imposed on the pile

Although the actual temperature of the pile varied versus depth (Knellwolf et al. 2011), it was assumed similarly to Laloui et al. (2006) that the temperature was constant versus depth for the purpose of computational modeling. The HEP was heated to a maximum of 21^{o}C during the heating phase, which lasted 12 days. This was followed by a cooling phase, during which the pile was cooled to 3^{o}C as shown in Figure 4.3 that depicts the temperature history of Test 1 (T1) (Laloui et al. 2006).

In the case of Test 7 (T7) (Laloui et al. 2006) the pile was subjected to mechanical load of 1000 kN, which was applied at the pile head over a time period of 8 months. This was followed by thermal loading, during which the pile was heated to a maximum of 14^{o}C, which lasted 22 days. Finally, the pile was cooled to 2^{o}C as shown in Figure 4.4.

Figure 4.3 The history of temperature imposed on the pile (thermal loading only)

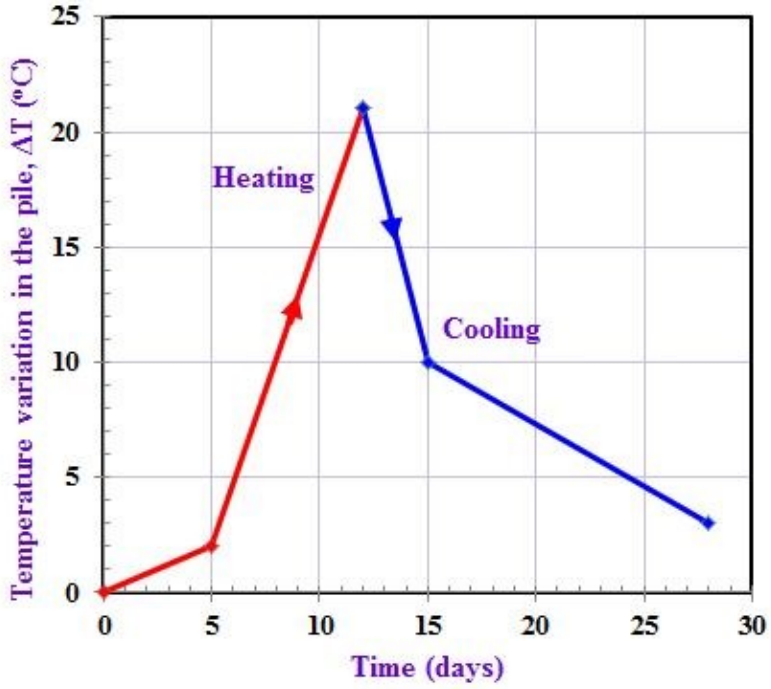

Figure 4.4 The history of temperature imposed on the pile (mechanical and thermal loading)

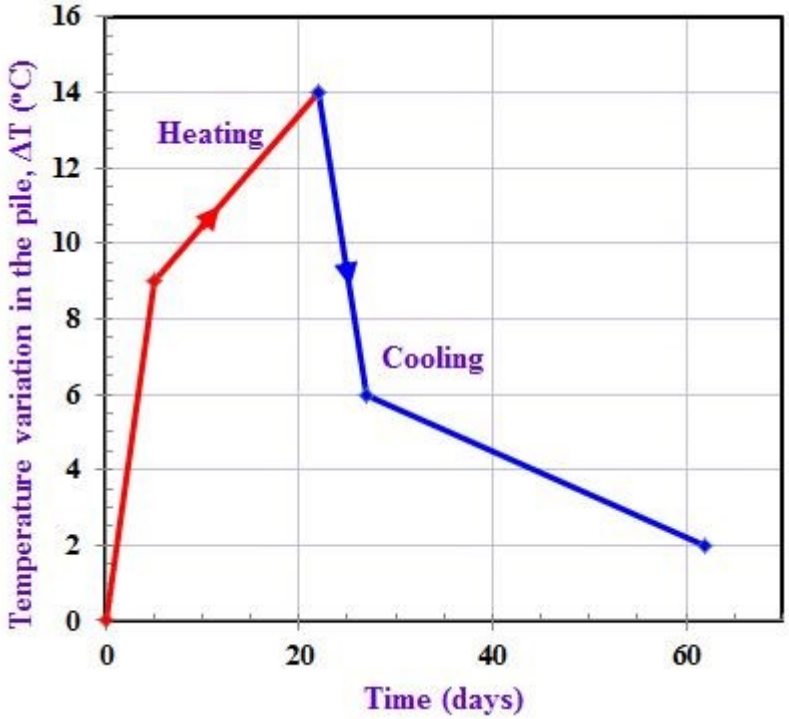

4.3 Concrete properties

The drilled pile is 88 cm in diameter and it has the length of 25.8 m. The integrity tests registered an increase in the pile diameter towards the pile tip. Thus, similarly to the FE analysis conducted by Laloui et al. (2006) for the purpose of computational modeling it was assumed that the pile diameter was equal to 1 m and constant with depth. Based on the laboratory test and cross-hole ultrasonic transmission tests, the known percentage of reinforcing steel, and the Young's modulus of steel, it was found that Young's modulus of the pile was equal to 29,200 MPa (Laloui et al. 2006). The additional properties of the reinforced concrete pile are taken from Lalaoui et al. (2006) and they are listed in Table 4.1.

In the FE model, the stress-strain relationship of the pile is assumed to be linear elastic. The pile is considered impervious and its weight is neglected in order to capture the effects of thermal loading only and to properly compare them to the measurements from test T1 (Laloui et al. 2011).

Table 4.1 Reinforced concrete pile properties (Laloui et al. 2006)

Property	**Reinforced concrete pile**
Young's modulus, E (MPa)	29,200
Poisson's ratio, ν	0.177
Mass density, ρ (kg/m^3)	2,500
Coefficient of thermal expansion, α (^{o}C^{-1})	1x10^{-5}
Heat capacity, C (J/m^3 ^{o}C)	2x10^6
Thermal conductivity, λ (W/m/^{o}C)	2.1

4.4 Soil properties

In the FE model, the soils are also assumed to behave as linear elastic materials. This is a reasonable assumption at this point since neither the thermal nor mechanical loads are excessive. In the case of thermal loading only the shear stress acting at the soil-pile interface does not seem to reach the threshold value corresponding to slipping and thus, the departure from the elastic state. This threshold is likely not to be exceeded even during the mechanical loading because the

direction of the axial displacement is reversed during the heating in case that it follows directly after the mechanical loading.

4.4.1 Isotropic elastic model

The effective Young's modulus (E') and Poisson's ratio (ν') describe an elastic response of isotropic materials. However, the alternative pair of elastic constants: the effective bulk (K') and shear (G') moduli are often used to describe the elastic deformation of an isotropic material. The bulk modulus describes the resistance to change in size, while the shear modulus describes the resistance to change in shape. In isotropic elasticity, the relationships between the two pairs of elastic constant are given by:

$$K' = \frac{E'}{3(1-2\nu')} \tag{4.7}$$

$$G' = \frac{E'}{2(1+\nu')} \tag{4.8}$$

It is noted that the superscript prime denotes the actual physics based material properties, which are used in effective stress analysis (ESA) that is conducted in the present study. The elastic constants of soil layers A1, A2, B, C and D were determined from the conventional triaxal compression tests (CTC) that were carried on several samples taken from different depths (Laloui et al. 1999).

Laboratory tests included two types of triaxial compression tests, drained (CIDC) and undrained (CIUC). CIDC test was conducted on the sample recovered from the depth of 12 m while CIUC tests were conducted on the sample taken from the depth of 16 m and additional test, for which a sample was most likely recovered from the depth of 22 m. Effective (E') and undrained (E_u) Young's moduli were determined from the slopes of unloading-reloading lines in deviator stress versus axial strain plots from CIDC and CIUC respectively.

The effective Poisson's ratio (ν') was determined from the negative ratio between increments of radial and axial strains obtained during unloading-reloading cycles in CIDC. This resulted in effective Poisson's ratio (ν') equal to 0.22.

For determination of the effective Poisson's ratio from CIUC tests the following relationship between the effective and undrained Young's moduli was used

$$E' = \frac{1+\nu'}{1+\nu_u} E_u \tag{4.9}$$

and $\nu_u = 0.5$ where determination of E_u was described in the paragraph above. Finally, using the isotropic elasticity the effective Poisson's ratio can be solved for from the following equation:

$$\Delta\varepsilon_1 = \frac{1}{E'}\left[\Delta\sigma_1' - \nu'\left(\Delta\sigma_2' + \Delta\sigma_3'\right)\right] \tag{4.10}$$

The increments of principal effective stresses in Equation (4.10) where determined from deviatoric stress (q) versus axial strain (ε_1), and deviatoric stress versus mean effective stress (p') plots from Laloui et al. (1999). Combining Equations (4.9) and (4.10) resulted in the effective Poisson's ratio (ν') of 0.5. This implies that the soils located at depths of 16 and 22 m are truly incompressible, which is not realistic. Thus, the procedure for determination of the effective Poisson's ratio, which is based on isotropic elasticity, must be incorrect, thus rendering these soils anisotropic. Consequently, two types of analyses were performed in this study, one assuming that all soils are isotropic elastic and the other assuming that two soil layers are anisotropic elastic. Furthermore, additional analyses were conducted whereby the bedrock was overlain by a single equivalent single isotropic and anisotropic soil. Table 4.2 lists the effective stiffness moduli for isotropic elastic model that were obtained in accordance with the above procedure. The additional materials properties shown in Table 4.2 were obtained from Laloui et al. (2006). The effective bulk and shear moduli of the bedrock (soil D) were taken as the mid-range value from Laloui et al. (2006).

Table 4.2 Soil properties

Property	**Soil A1**	**Soil A2**	**Soil B**	**Soil C**	**Soil D**
Bulk modulus, K' (MPa)	113.10	113.10	983.33	1,383.33	1,860
Shear modulus, G' (MPa)	77.87	77.87	19.80	27.85	1,675
Poisson's ratio, ν'	0.22	0.22	0.49	0.49	0.157
Mass density, ρ (kg/m^3)	2,000	1,950	2,000	2,200	2,550
Coefficient of thermal expansion, α (^{o}C^{-1})	1x10^{-5}	1x10^{-5}	1x10^{-4}	1x10^{-4}	1x10^{-6}
Heat capacity, C (J/m^3 ^{o}C)	2.4x10^6	2.4x10^6	2.4x10^6	2.4x10^6	2.0x10^6
Thermal conductivity, λ (W/m/^{o}C)	1.8	1.8	1.8	1.8	1.1

4.4.2 Anisotropic elastic model

As explained above results of CIUC tests on soils B and C indicated that they are most likely not isotropically elastic. Soils are typically transversely isotropic materials. For such materials the one of the physical properties is symmetric about a vertical axis, which is normal to the plane of isotropy. Consequently, the number of independent elastic constants for transversely isotropic material is five. Graham and Houlsby, (1983) proposed a method to compute the elastic parameters for a transversely isotropic soil. The corresponding relationship between the stress and mechanical strain increments is then given by:

$$\begin{bmatrix} d\varepsilon_{xx} \\ d\varepsilon_{yy} \\ d\varepsilon_{zz} \\ d\gamma_{yz} \\ d\gamma_{zx} \\ d\gamma_{xy} \end{bmatrix} = \begin{bmatrix} 1/E_h & -\nu_{hh}/E_h & -\nu_{vh}/E_v & 0 & 0 & 0 \\ -\nu_{hh}/E_h & 1/E_h & -\nu_{vh}/E_v & 0 & 0 & 0 \\ -\nu_{vh}/E_v & -\nu_{vh}/E_v & 1/E_v & 0 & 0 & 0 \\ 0 & 0 & 0 & 1/G_{vh} & 0 & 0 \\ 0 & 0 & 0 & 0 & 1/G_{vh} & 0 \\ 0 & 0 & 0 & 0 & 0 & 2(1+\nu_{hh})/E_h \end{bmatrix} \begin{bmatrix} d\sigma'_{xx} \\ d\sigma'_{yy} \\ d\sigma'_{zz} \\ d\tau_{yz} \\ d\tau_{zx} \\ d\tau_{xy} \end{bmatrix} \tag{4.11}$$

where *x*,*y* and *z* denotes two horizontal coordinate axes and z is a vertical axis. Since all soil samples retrieved during the site investigation were oriented in vertical direction only three elastic parameters can be determined (Graham and Houlsby, 1983). Similarly Wood, (1990) provides the following simplified material description, which is suitable for modeling transversely isotropic soils in case when only vertically oriented samples are available for triaxial testing. It is given by:

$$\begin{bmatrix} d\varepsilon_{xx} \\ d\varepsilon_{yy} \\ d\varepsilon_{zz} \\ d\gamma_{yz} \\ d\gamma_{zx} \\ d\gamma_{xy} \end{bmatrix} = 1/E^* \begin{bmatrix} 1/\alpha^2 & -\nu^*/\alpha^2 & -\nu^*/\alpha & 0 & 0 & 0 \\ -\nu^*/\alpha^2 & 1/\alpha^2 & -\nu^*/\alpha & 0 & 0 & 0 \\ -\nu^*/\alpha & -\nu^*/\alpha & 1 & 0 & 0 & 0 \\ 0 & 0 & 0 & 2(1+\nu^*)/\alpha & 0 & 0 \\ 0 & 0 & 0 & 0 & 2(1+\nu^*)/\alpha & 0 \\ 0 & 0 & 0 & 0 & 0 & 2(1+\nu^*)/\alpha^2 \end{bmatrix} \begin{bmatrix} d\sigma'_{xx} \\ d\sigma'_{yy} \\ d\sigma'_{zz} \\ d\tau_{yz} \\ d\tau_{zx} \\ d\tau_{xy} \end{bmatrix} \tag{4.12}$$

where E^* and ν^* are the modified values of Young's modulus and Poisson's ratio for the soil, while α is the parameter describing the amount of anisotropy that is present. In equation (4.12), the isotropic E' and ν' values have been replaced by modified parameters E^* and ν^* that describe an anisotropic soil. Also, by setting $\alpha = 1$ in equation (4.12) isotropic material is recovered.

Furthermore, for α > 1 the soil is stiffer horizontally than vertically and for α < 1 the soil is stiffer vertically than horizontally.

It follows from equation (4.12) that:

$$d\varepsilon_{xx} = \frac{1}{E^*}\left(\frac{1}{\alpha^2} d\sigma'_{xx} - \frac{\nu^*}{\alpha^2} d\sigma'_{yy} - \frac{\nu^*}{\alpha} d\sigma'_{zz} \right) \tag{4.13}$$

$$d\varepsilon_{yy} = \frac{1}{E^*}\left(-\frac{\nu^*}{\alpha^2} d\sigma'_{xx} + \frac{1}{\alpha^2} d\sigma'_{yy} - \frac{\nu^*}{\alpha} d\sigma'_{zz} \right) \tag{4.14}$$

$$d\varepsilon_{zz} = \frac{1}{E^*}\left(-\frac{\nu^*}{\alpha} d\sigma'_{xx} - \frac{\nu^*}{\alpha} d\sigma'_{yy} + d\sigma'_{zz} \right) \tag{4.15}$$

By assuming that the principal stresses act on vertical and horizontal planes in the CTC test a deviatoric stress (*q)* is given by

$$dq = d\sigma'_{zz} - d\sigma'_{xx} \tag{4.16}$$

And mean effective stress (*p′*) is given by:

$$3\,dp' = d\sigma'_{zz} + d\sigma'_{xx} + d\sigma'_{yy} = d\sigma'_{zz} + 2d\sigma'_{xx} = d\sigma'_{zz} + 2d\sigma'_{yy} \tag{4.17}$$

And volume constraint in undrained CTC on saturated soil gives:

$$d\varepsilon_v = d\varepsilon_{xx} + d\varepsilon_{yy} + d\varepsilon_{zz} = 2d\varepsilon_{xx} + d\varepsilon_{zz} = 2d\varepsilon_{yy} + d\varepsilon_{zz} = 0 \tag{4.18}$$

dq, dp' and $d\varepsilon_{zz}$ can be obtained from the triaxial test results preferably during the unloading-reloading cycle. Specifically, $d\sigma'_{xx}$, $d\sigma'_{yy}$ and $d\sigma'_{zz}$ can be calculated from equations (4.16) and (4.17) while $d\varepsilon_{xx}$ and $d\varepsilon_{yy}$ can be computed from equation (4.18). By combining equations (4.13) or (4.14) and (4.15), modified values of Young's modulus (*E**) and Poisson's ratio (ν^*) can be obtained while assuming a certain value of the anisotropy parameter (α). By comparison between equations (4.11) and (4.12), it can be found that $E_v = E^*$, $E_h = \alpha^2 E^*$, $\nu_{vh} = \nu^*/\alpha$, $\nu_{hh} = \nu^*$ and $G_{vh} = \alpha E^*/2(1+\nu^*)$, which provide the material parameters for ABAQUS. They are listed in Table 4.3.

Figures 4.5 and 4.6 show the relationship between the anisotropy parameter α and modified Poisson's ratio ν^* for soils B and C, respectively. Based on Figures 4.5 and 4.6 the value of α equal to 0.4 was selected to represent the most anisotropic soil, while maintaining the value of ν^* not smaller than 0.1. The goal was to conduct the analyses for two extreme cases represented by α value of 0.4 and 1.

It is noted that transverse isotropy is assumed with respect to the relationship between the stress and mechanical strain only. However, coefficient of thermal expansion in the plane of transverse isotropy is equal to the one in the direction perpendicular to the plane. Thus, the material is isotropic with respect to thermal strain.

Table 4.3 Anisotropic elastic parameters for different values of α

Soil Types	α	$E_h = E_h$ (MPa)	E_v (MPa)	ν_{vh}	ν_{hh}	G_{vh} (MPa)	G_{hh} (MPa)
B	0.4	8.97	56.06	0.1310	0.0524	10.83	4.33
C	0.4	12.92	80.74	0.1940	0.0776	15.08	6.03

Figure 4.5 Anisotropy parameter α versus ν^* for soil B

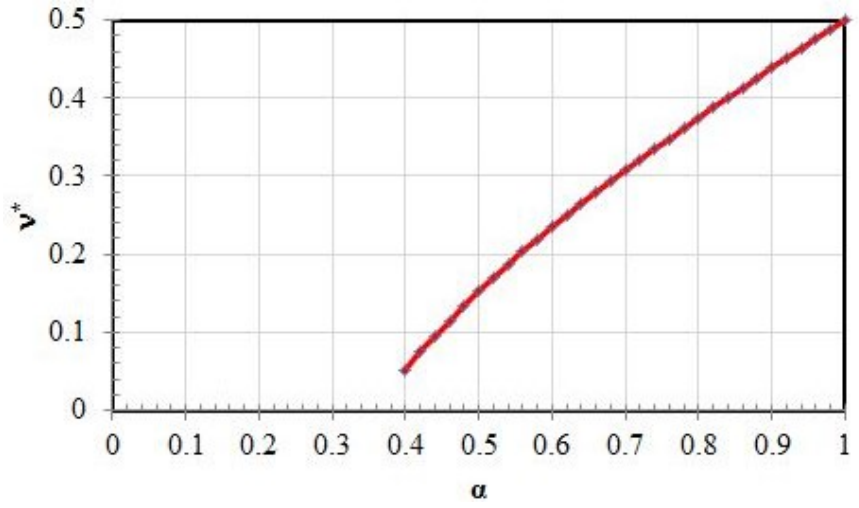

Figure 4.6 Anisotropy parameter α versus ν^* for soil C

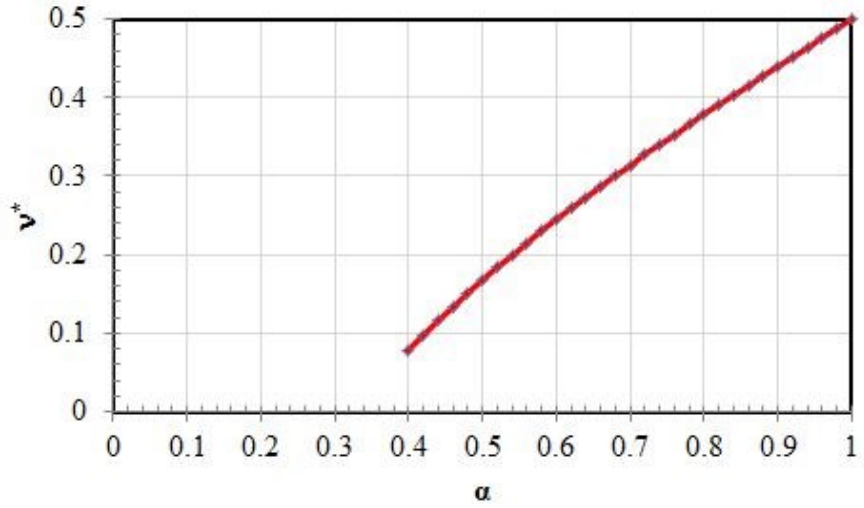

Chapter 5 - Results and Discussion

A 2D axisymmetric finite element analyses of a single HEP are performed by using the finite element software ABAQUS/CAE 6.13-2. This chapter presents the results along with the relevant experimental data. Additional discussion is also included.

5.1 Temperature distribution

The temperature fields after heating and cooling period are presented in this section.

5.1.1 Isotropic elastic model

The temperature in the pile was assumed constant with depth in the FE model. The temperature distributions in the surrounding soil was captured at the end of the heating and cooling periods corresponding to 21^{o}C and 3^{o}C, respectively for test T1 presented in Figure 5.1.

Figure 5.1 The distribution of temperature into the soil

(a) at the end of heating phase (b) at the end of cooling phase

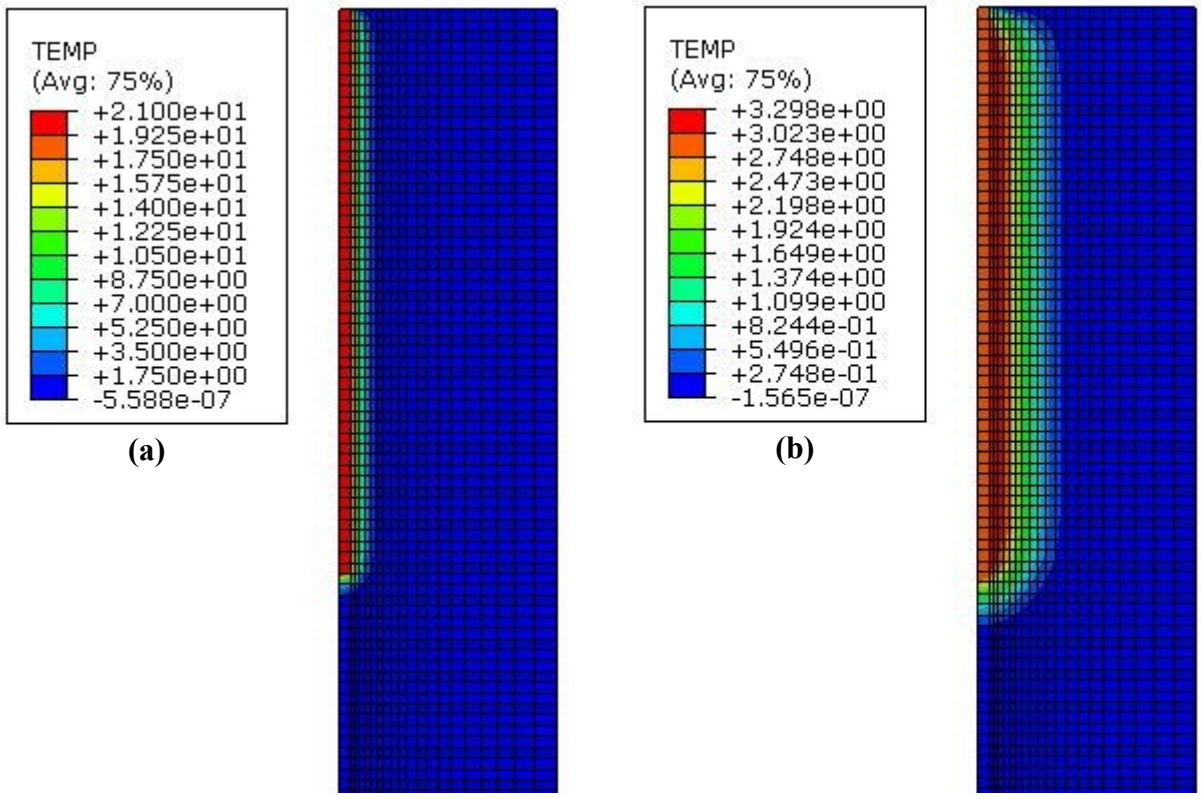

Figure 5.2 shows the deformation and distribution of the temperature into the soil at the end of heating and cooling phase.

Figure 5.2 The deformation and distribution of temperature into the soil
(a) at the end of heating phase (deformation scale factor 1711)
(b) at the end of cooling phase (deformation scale factor 1711)

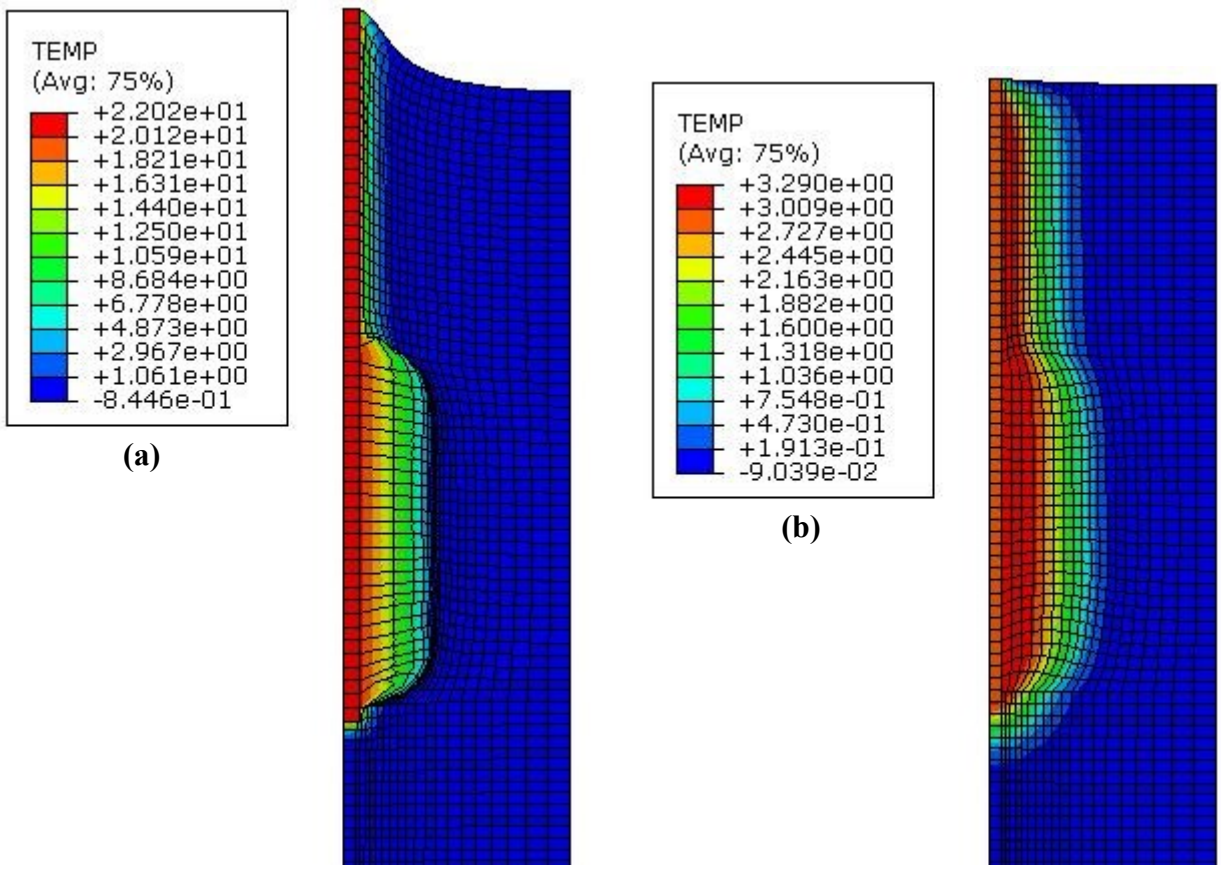

Thus, the temperature in the pile varied with time only. Due to the presence of the bedrock D, heating and cooling in the vicinity of the pile occurs mainly in the horizontal direction. At the end of heating phase (21^{o}C), the maximum temperature difference in the soil is approximately 17^{o}C while the minimum temperature difference is 0^{o}C at a distance of 2 m from the pile. At the end of cooling phase (3^{o}C), the maximum temperature difference in the soil is approximately 3.3^{o}C while the minimum temperature difference is 1^{o}C at a distance of 4 m from the pile edge.

5.1.2 Anisotropic elastic model

Compared to the isotropic elastic model, the maximum and minimum temperature difference in the soil are equal at the ends of the heating and cooling periods. However, the strain in the soils, which is shown in Figures 5.2 and 5.3 are different below the depth of 12m. This is due to different elastic properties of the isotropic and anisotropic soils.

Figure 5.3 The deformation and distribution of temperature into the soil
(a) at the end of heating phase (deformation scale factor 1711)
(b) at the end of cooling phase (deformation scale factor 1711)

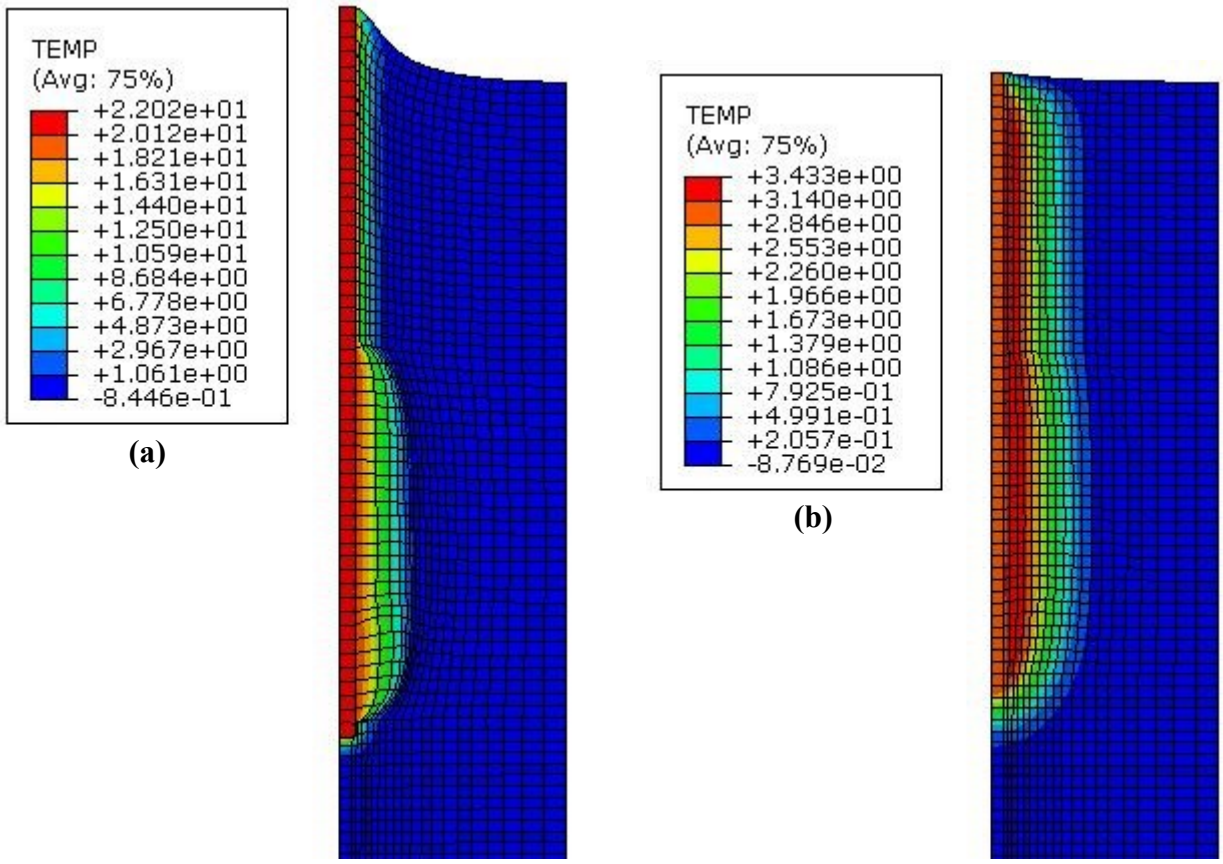

5.2 The behavior of HEP due to thermal loading only (T1)

Each set of results is presented in two groups. The first group shows the response of the HEP in the isotropic elastic soils. The second group shows the response of the HEP in the anisotropic elastic soils. Each group depicts the displacements of the pile head and tip versus

time, and displacement versus depth. This is followed by the axial strain in the pile at the end of heating (21^{o}C) and cooling (3^{o}C) phases. The axial stress in the pile at 13.4^{o}C is also plotted versus depth, as well as the shear stress in the soil next to the pile at 21^{o}C and 3^{o}C. Finally, the vertical strain in the pile versus depth at 13.4^{o}C was also plotted.

According to Knellwolf et al. (2011), maximum deviations of temperatures measured in the pile were not constant versus depth. They showed that the maximum deviations of temperature around the average value, was ± 2^{o}C. Thus, the vertical head and tip displacements, vertical strain and stress were plotted for the average temperature, and ± 2^{o}C.

5.2.1 Isotropic elastic model

5.2.1.1 Displacements

The displacements of the pile head and tip in isotropic elastic soils are shown in Figure 5.4. These results agree very well with the field measurements obtained by optical fibers. The predicted head displacements are smaller than the measurement obtained from the extensometers during the heating phase. The predicted maximum upward displacements of the pile head range from 2.7 mm to 3.4 mm while they are only around 0.2 mm for the pile tip. These values correspond to the maximum temperature difference increase of 21^{o}C. Figure 5.5 depicts the vertical displacement of the pile versus depth at the end of the heating phase (21^{o}C), and at the end of the cooling phase (3^{o}C). The null point of the pile was located approximately at 24.5 m depth at the end of heating period. It changed the location to about 25.5 m depth at the end of cooling phase.

Figure 5.4 Vertical displacements of the pile head and tip versus time (T1)

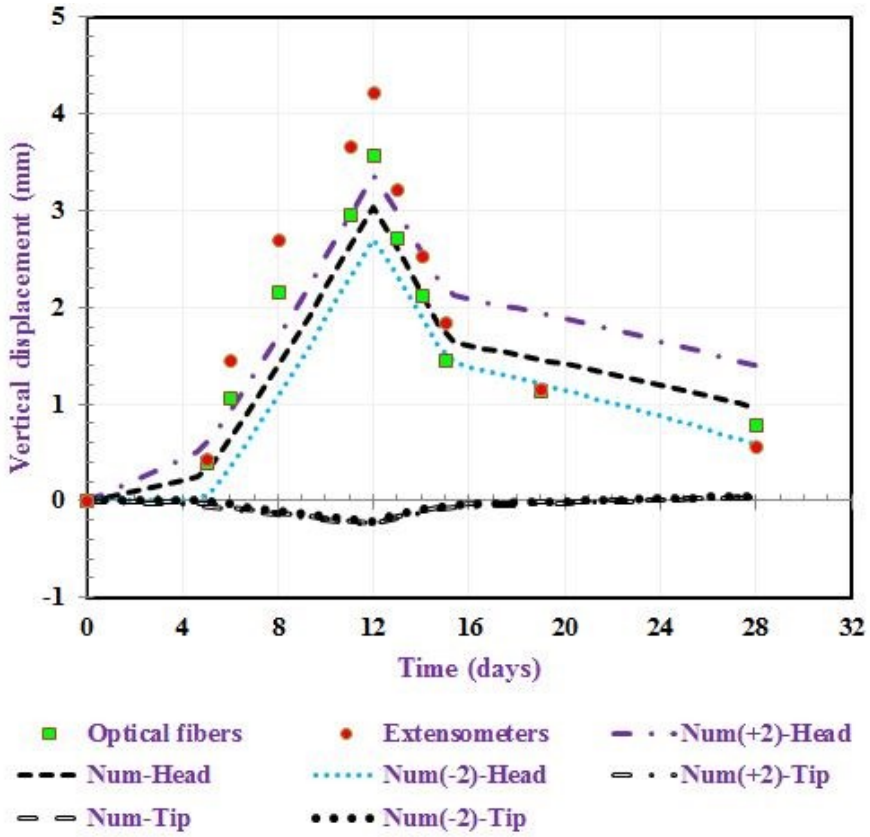

Figure 5.5 Vertical displacement of the pile versus depth at 21°C and 3°C (T1)

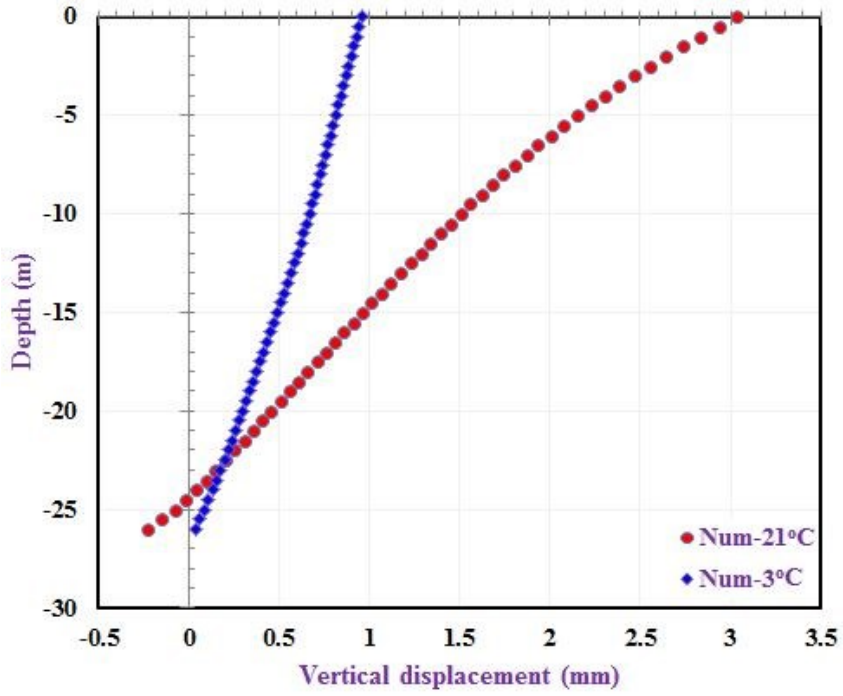

5.2.1.2 Strains

The predicted radial strains (at depth of 16 m) in the Figure 5.6 are much lower than the measured ones. It should be noted that the trend of the predicted radial strains follow the trend of the temperature history imposed on the pile. The predicted maximum radial strain is 230 μm, and the strains do not return to zero at the end of the cooling cycle. It is noted that temperature difference does not return to zero at the end of cooling cycle either. One of the reasons for this disagreement might be due to pile diameter is not being constant with depth while in the FE model it is assumed to be constant.

Figure 5.6 Radial strain in the pile at depth of 16 m during thermal loading (T1)

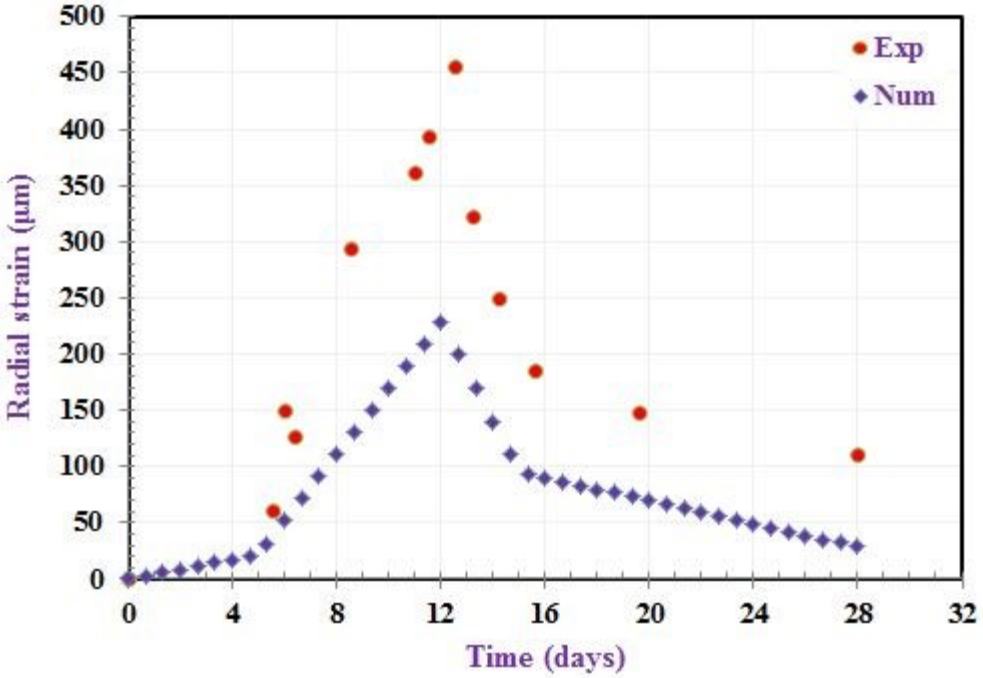

The effects of heating and cooling cycles on the strains in the pile are presented in the Figures 5.7 to 5.9. The vertical strains predicted by the computational model were slightly lower than the experimental data obtained from both devices: optical fibers (OF) and vibrating wire strain gauges (VWSG) at the end of heating phase. Figure 5.7 indicates that the maximum vertical strain occurred at the pile head. The minimum vertical strain at the end of heating period was located at around 19 m. Figures 5.7 to 5.9 also show that vertical strains are not constant with depth.

Figure 5.7 Vertical strain in the pile versus depth at 21°C (T1)

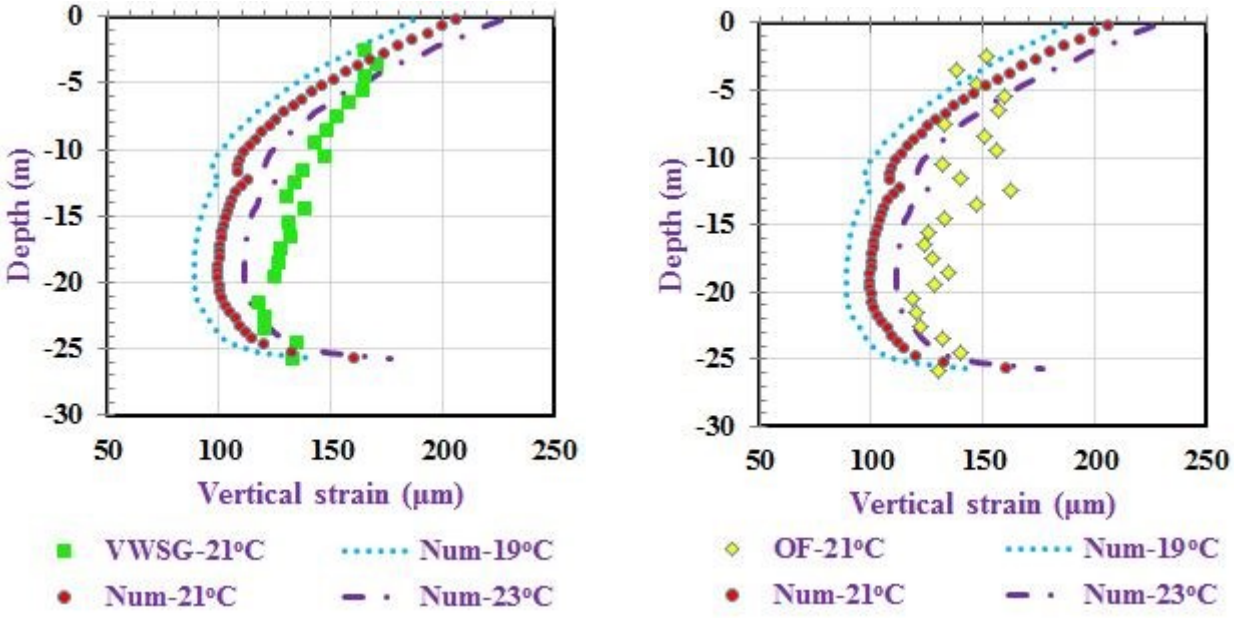

Figure 5.8 Vertical strain in the pile versus depth at 3°C (T1)

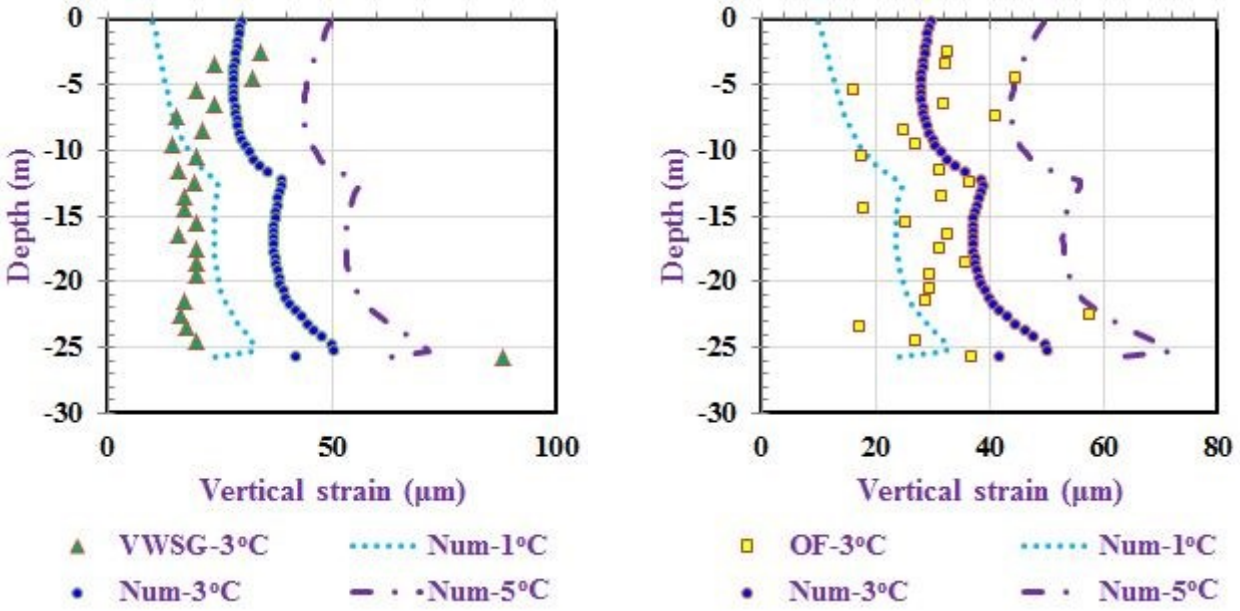

The vertical strains in the pile versus depth at 13.4°C are presented in Figure 5.9. The strains predicted for the pile temperature that is 2°C lower than the average fit the strains measured by VWSG very well. The minimum vertical strain was located at around 19 m. This depth corresponds to the location maximum compressive stresses at this temperature as shown in Figure 5.10.

Figure 5.9 Vertical strain in the pile versus depth at 13.4°C (T1)

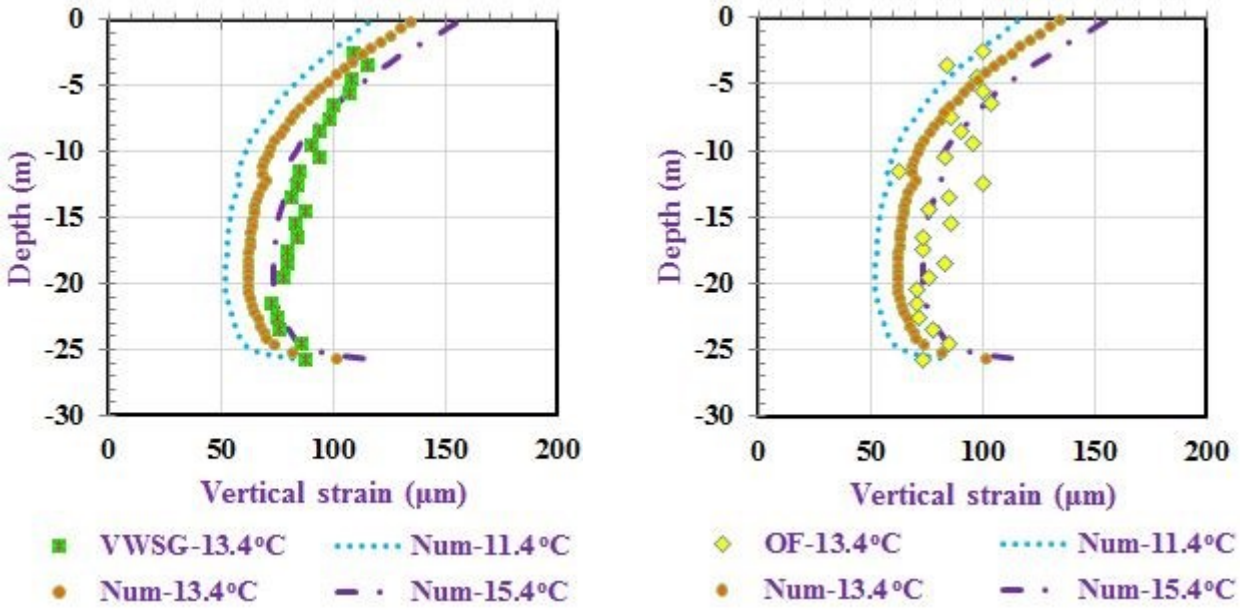

5.2.1.3 Stress

As was mentioned previously, vertical stresses in the pile are not directly measured. They are calculated from vertical strains *ε(z)*, which was measured by VWSG and OF as follows

$$\sigma(z) = E_{pile}[\varepsilon(z) - \alpha\Delta T] \tag{5.1}$$

Figure 5.10 Vertical stress in the pile versus depth at 13.4°C (T1)

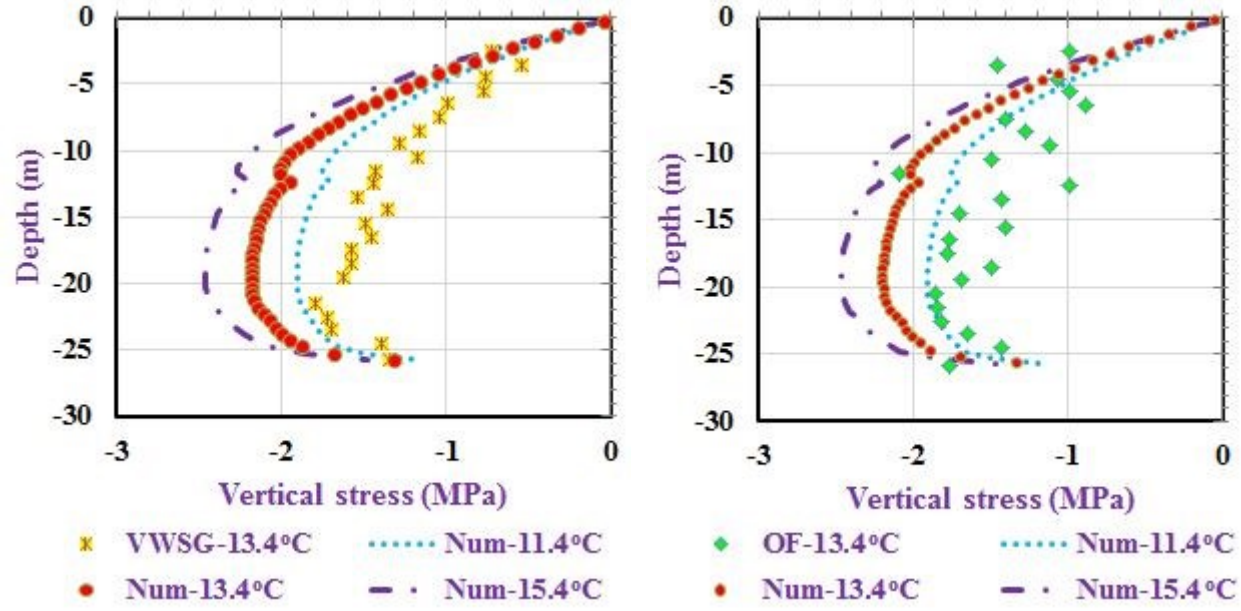

It is noted that one dimensional state of stress and strain is assumed in equation 5.1. Figure 5.10 shows the comparison between measured and predicted vertical stresses at a temperature difference of 13.4^{o}C. Predicted stresses are larger than measured ones. The changes in the slopes of stress diagrams at depth of 12 m are due to the boundary between layers A2 and B. The boundary is located at depth of 12 m.

Shear stresses next to the pile are depicted in Figure 5.11. At the end of heating phase, the positive shear stresses develop in the upper portion of the pile, while the negative shear stresses are generated in the lower portion. The maximum shear stress occurs near the pile tip at the end of heating phase because the pile is embedded 0.5 m into the bedrock. The minimum shear stress develops at the pile head. However, numerical integration of shear stresses over the shaft area resulted in the negative skin frictions in the amount of -1,091 kN at the end of heating phase. Conversely, the skin friction reversed to the positive value of 208.2 kN at the end of cooling phase. The changes in the slopes of shear stress diagrams at depth of 12 m that are depicted in Figure 5.11 are due to boundary between layers A2 and B.

Figure 5.11 Shear stress next to pile versus depth at 21^{o}C and 3^{o}C (T1)

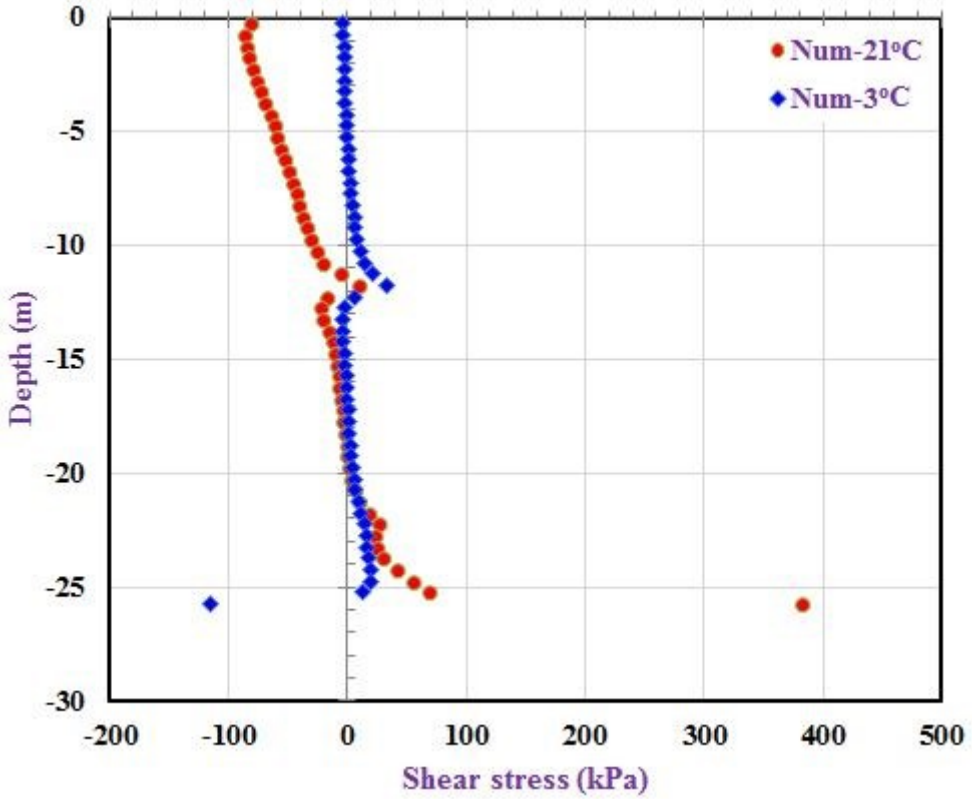

5.2.1.4 Equivalent soil

Additional analysis was performed for the end bearing pile embedded in an equivalent homogeneous soil. Since soil layers A1, A2, B and C together provide the shaft friction, the bulk modulus (K_{eq}) and shear modulus (G_{eq}) of the equivalent homogeneous soil are computed as

$$K_{eq} = \frac{\sum_{i=1}^{4} L_i}{\sum_{i=1}^{4} L_i / K_i} \tag{5.2}$$

$$G_{eq} = \frac{1}{\sum_{i=1}^{4} 1/4G_i} \tag{5.3}$$

where K_i, G_i and L_i are bulk modulus, shear modulus and depths of individual soil layers (A1, A2, B and C).

It is assumed that the specific heat of the equivalent soil (c_{eq}) for the entire volume is equal to the sum of specific heat over the volumes of individual soil layers as follows

$$c_{eq} = \frac{\sum_{i=1}^{4} c_i \rho_i L_i}{\sum_{i=1}^{4} \rho_i L_i} \tag{5.4}$$

where c_i and ρ_i are the heat capacities and mass densities of individual soil layers (A1, A2, B and C).

The remaining properties of the equivalent soil are given by

$$X_{eq} = \frac{\sum_{i=1}^{4} X_i L_i}{\sum_{i=1}^{4} L_i} \tag{5.5}$$

where X_i stands for coefficients of thermal expansion (α_i), thermal conductivities (λ_i), mass densities (ρ_i) and permeabilities (k_i) of individual soil layers (A1, A2, B and C).

Equation (5.5) is based on the assumption that the total flow of heat and water through the entire layered system is equal to the sum of the flows through individual layers. It has also been assumed the thermally induced volume changes of the equivalent soil are equal to the sum of thermally induced volume changes of the individual layers. Finally, a mass density of the

equivalent soil was obtained as a volume average of the mass densities of the individual soil layers.

The numerically predicted displacement of the pile head in this case is closer to the field measurements during the heating phase than in the case of the actual layered soil profile (Figure 5.12). The predicted maximum upward displacements of the pile head range from 3.1 mm to 3.9 mm. The maximum predicted displacement at the pile toe are all 0.2 mm. The null point of the pile in Figure 5.13 was located approximately at a depth of 24.5 m at the end of the heating period.

Figure 5.12 Vertical displacement of the pile head and tip versus time (T1)

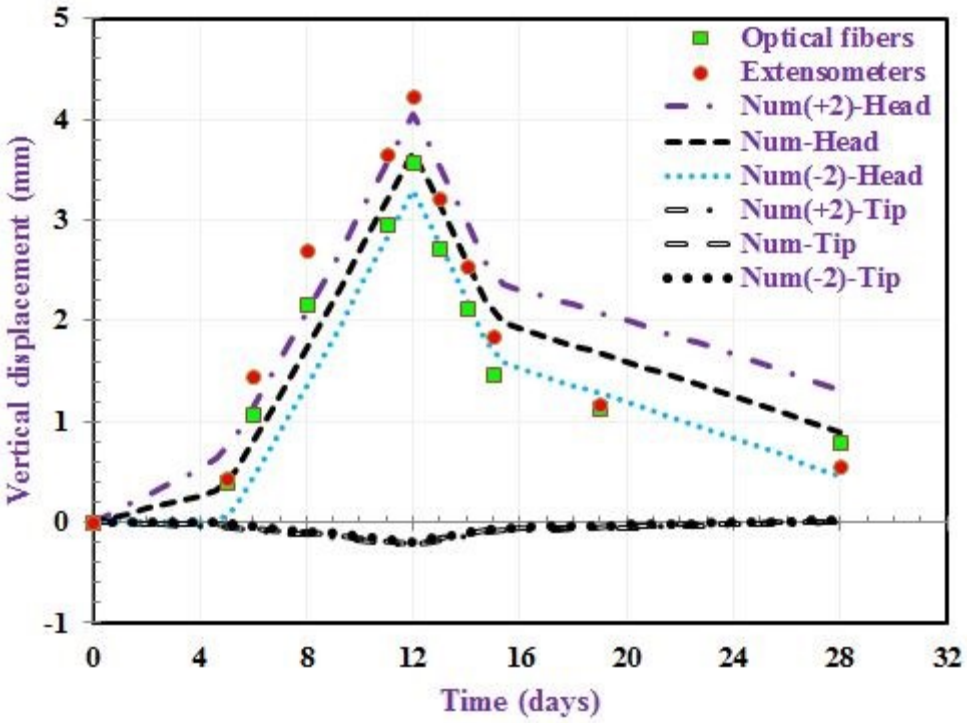

Figure 5.13 Vertical displacement of the pile versus depth at 21°C and 3°C (T1)

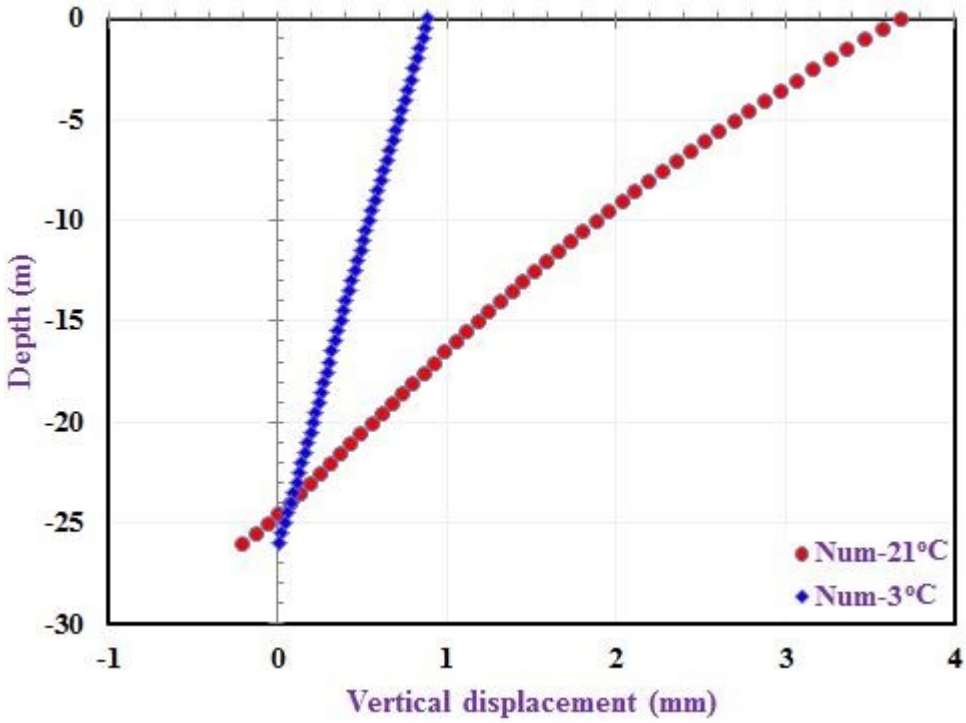

Figure 5.14 Vertical strain in the pile versus depth at 21°C (T1)

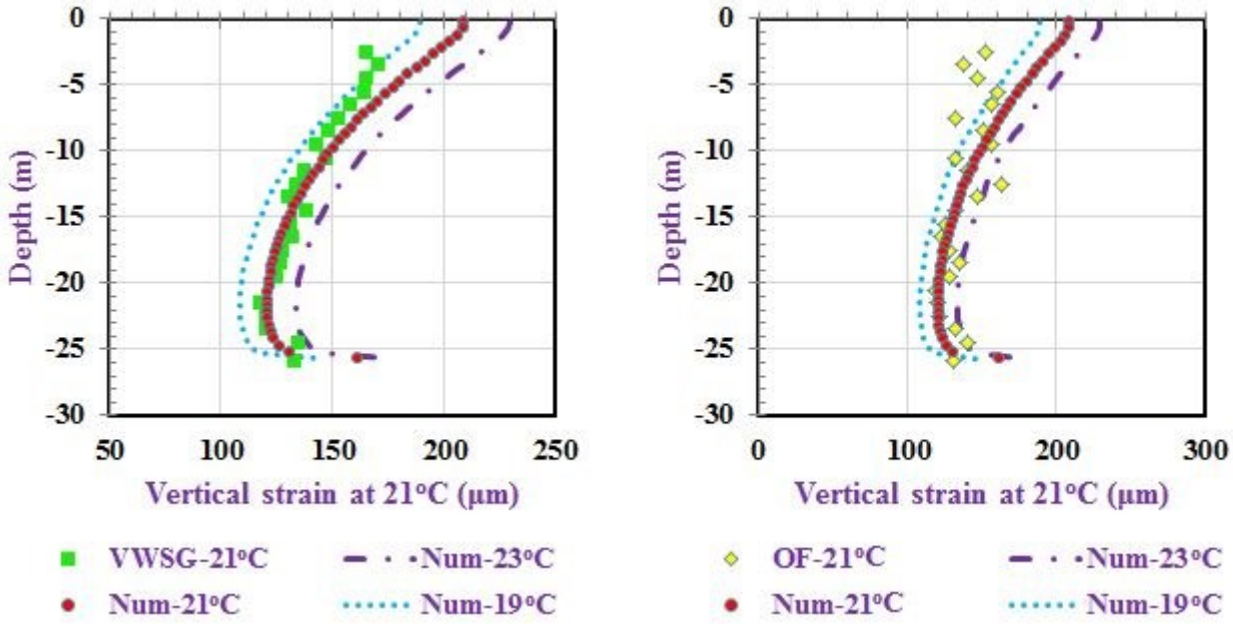

The predicted radial strains in most cases do not change significantly. However, the predicted vertical strains in the present case are closer to the measured strains as compared to the actual layered soils. As noted previously, the maximum temperature deviation from the average

value is ± 2°C. Taking this into account, the computational predictions depicted in Figure 5.14 through 5.16 are very good. It is noted that measurements are not available a couple meter depths close to the ground surface.

Figure 5.15 Vertical strain in the pile versus depth at 3°C (T1)

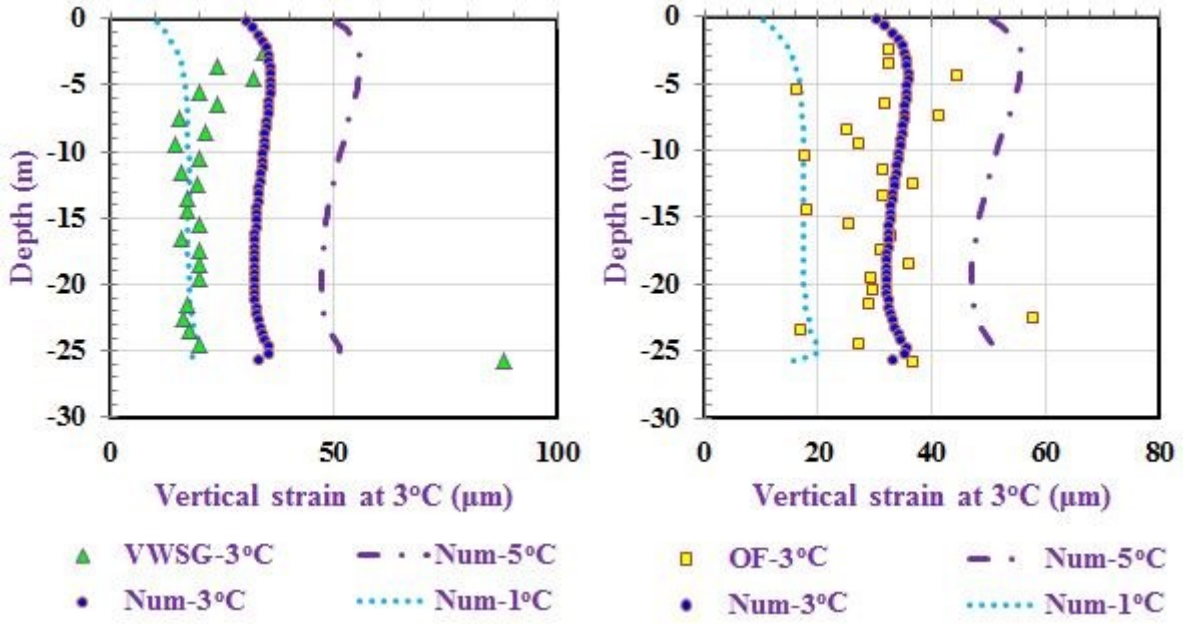

Figure 5.16 Vertical strain in the pile versus depth at 13.4°C (T1)

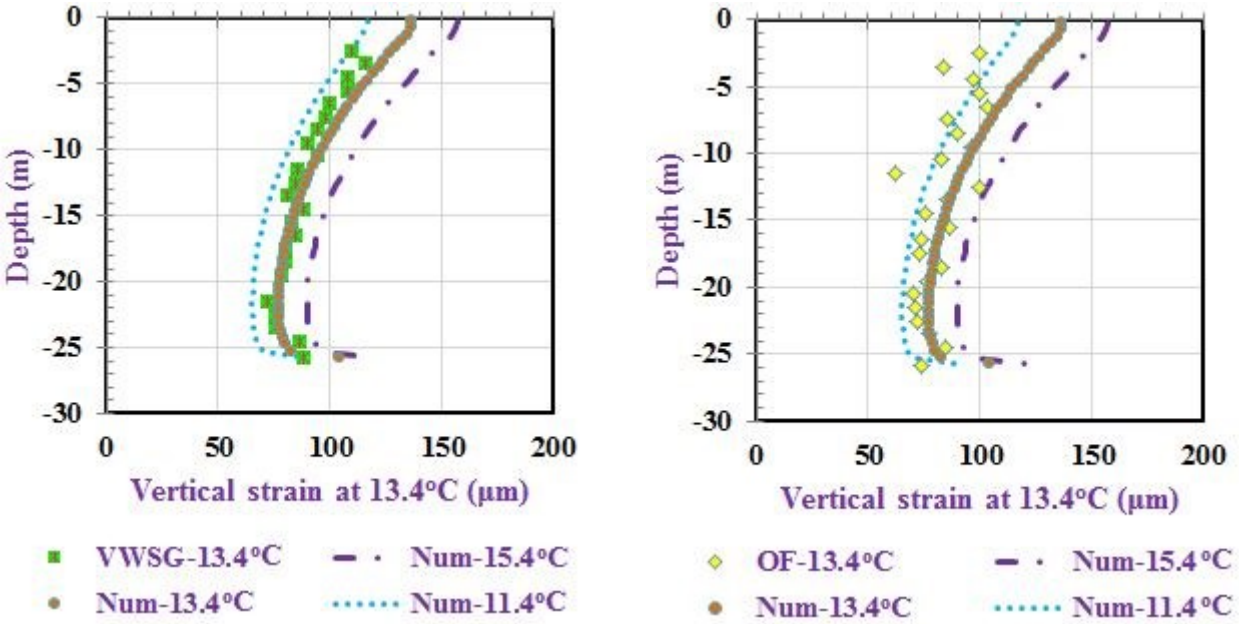

Predicted vertical stresses at 13.4°C are very close to the measured ones. In this case the vertical stress distribution versus depth is captured with a smooth response curve because a single homogeneous soil is underlain by the bedrock. The stress at the pile head is zero since no mechanical load is applied.

Figure 5.17 Vertical stress in the pile versus depth at 13.4°C (T1)

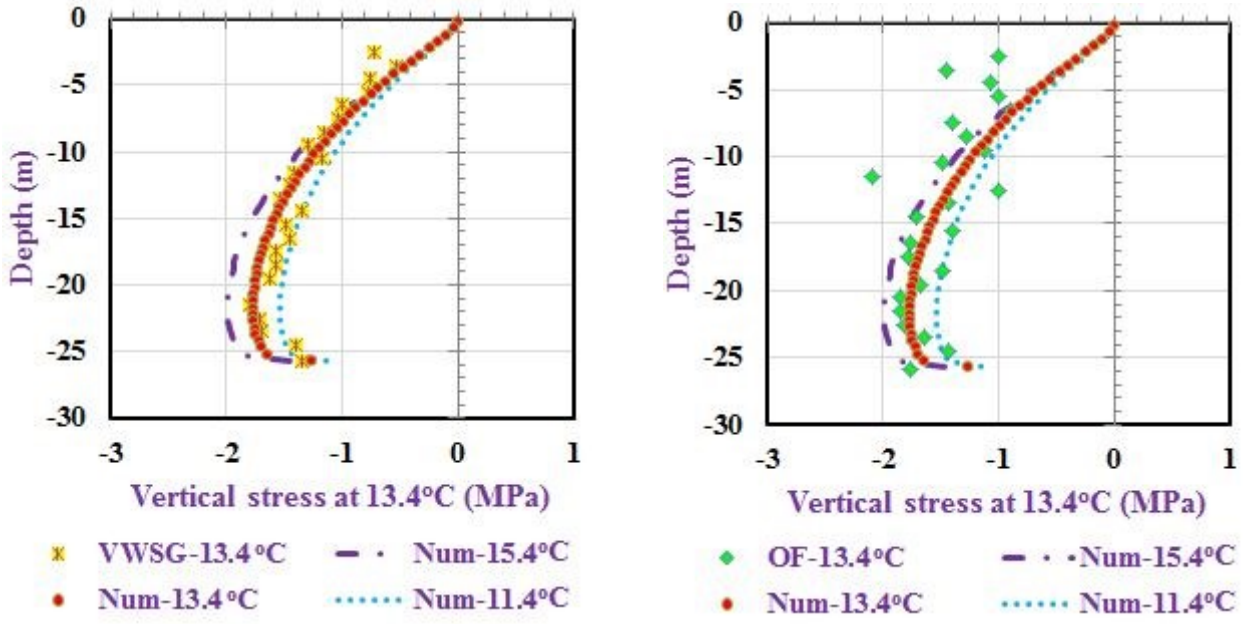

Shear stresses next to the pile are depicted in Figure 5.18. Again, the positive shear stresses develop in the upper approximately 2/3 of the pile length. The maximum positive shear stress develops at the pile tip at the end of the heating phase. The resultant of the negative skin friction is equal to -1,724 kN, thus the magnitude of negative skin friction force is larger in the case of equivalent soil in comparison with a layered soil. At the end of cooling phase, the resultant of the skin friction reversed to the positive value of 47.2 kN.

Figure 5.18 Shear stress next to pile versus depth at 21°C and 3°C (T1)

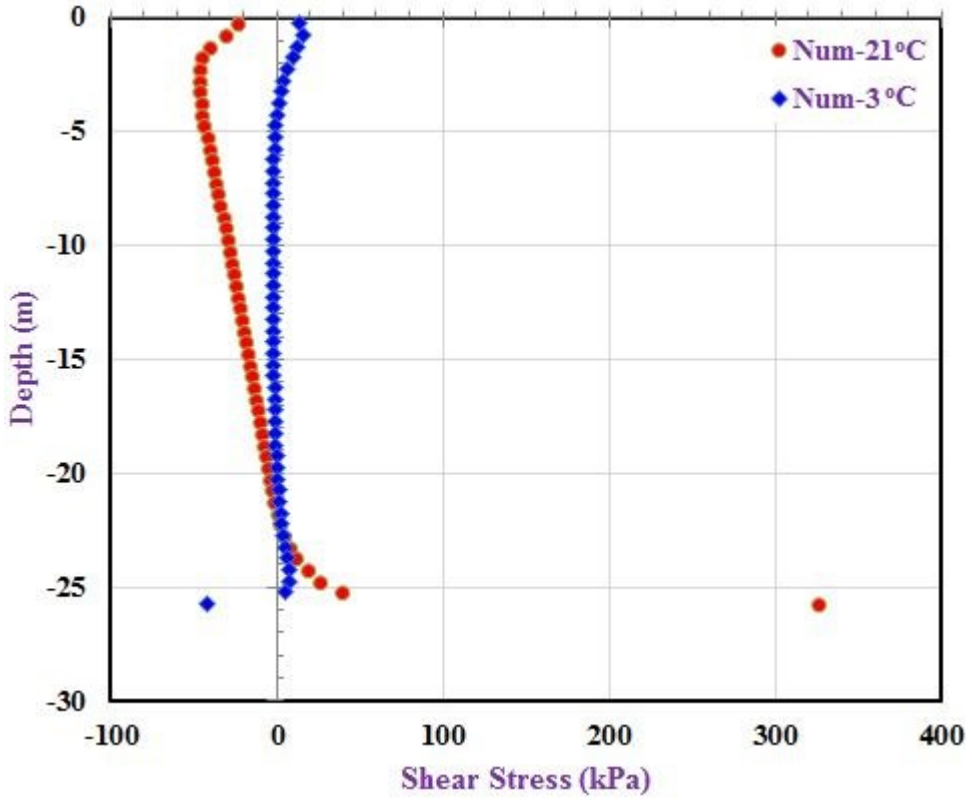

5.2.2 Anisotropic elastic model

5.2.2.1 Displacement

The displacements of the pile toe for anisotropic elastic model are almost equal to those predicted by the isotropic elastic model. There is an improvement in the predicted maximum upward displacements of the pile head which now range from 3.2 mm to 3.9 mm comparing to the previous range from 2.7 mm to 3.6 mm in the isotropic case. The vertical displacements of the pile versus depth at the end of the heating phase (21°C), and at the end of the cooling phase (3°C) are shown in Figure 5.20. The null point of the pile remains at the depth of 24.5 m depth at the end of the heating period.

Figure 5.19 Vertical displacements of the pile head and tip versus time (T1)

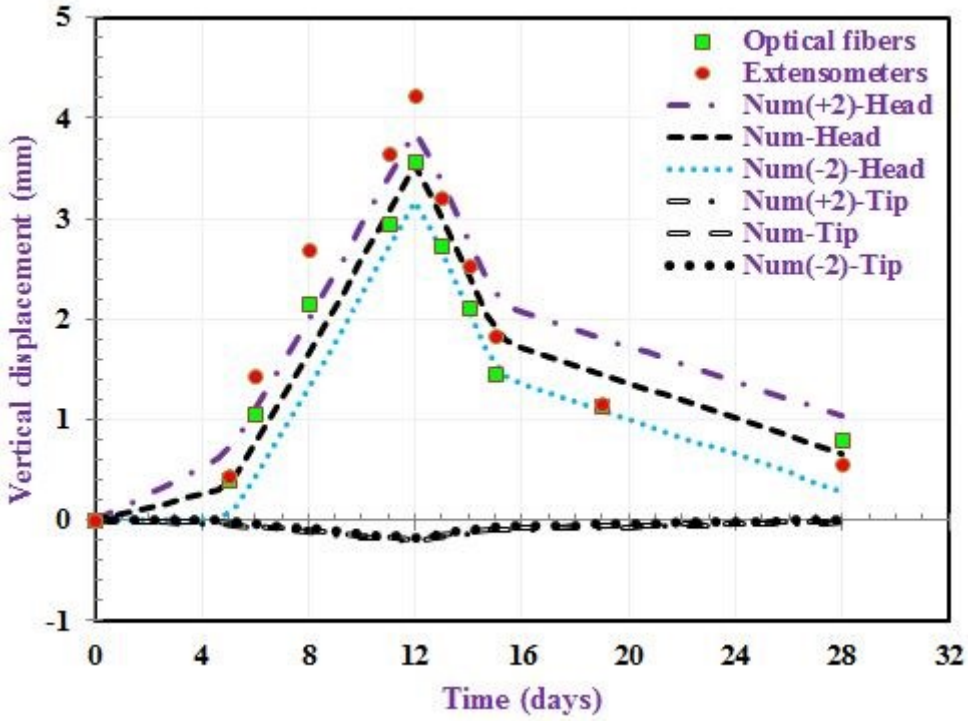

Figure 5.20 Vertical displacement of the pile versus depth at 21°C and 3°C (T1)

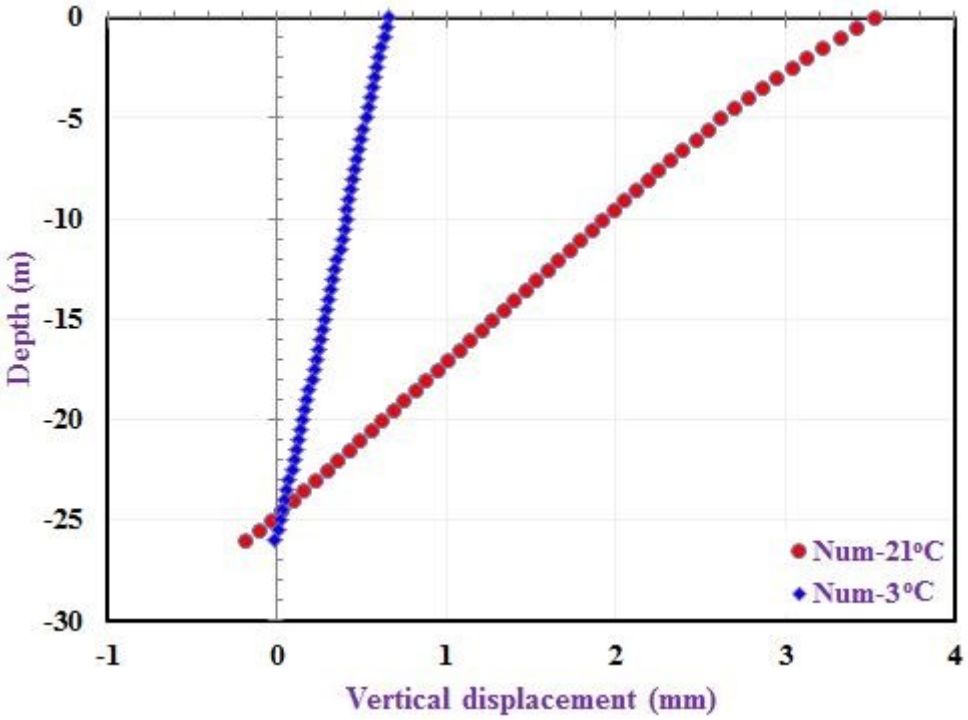

5.2.2.2 Strain

The anisotropic elastic model predicted very good to excellent of vertical strains in the pile as depicted in Figures 5.21 to 5.23. The measured data is still in the range of the upper and lower limits of the strains at 21°C, 3°C and 13.4°C, except the point at 25.8 m depth at 3°C. It is because the large difference in vertical strains measured at depths of 25 m and 25.5 m that the VWSG measured at 25.5 m was affected by a malfunction of the VWSG.

Figure 5.21 Vertical strain in the pile versus depth at 21°C (T1)

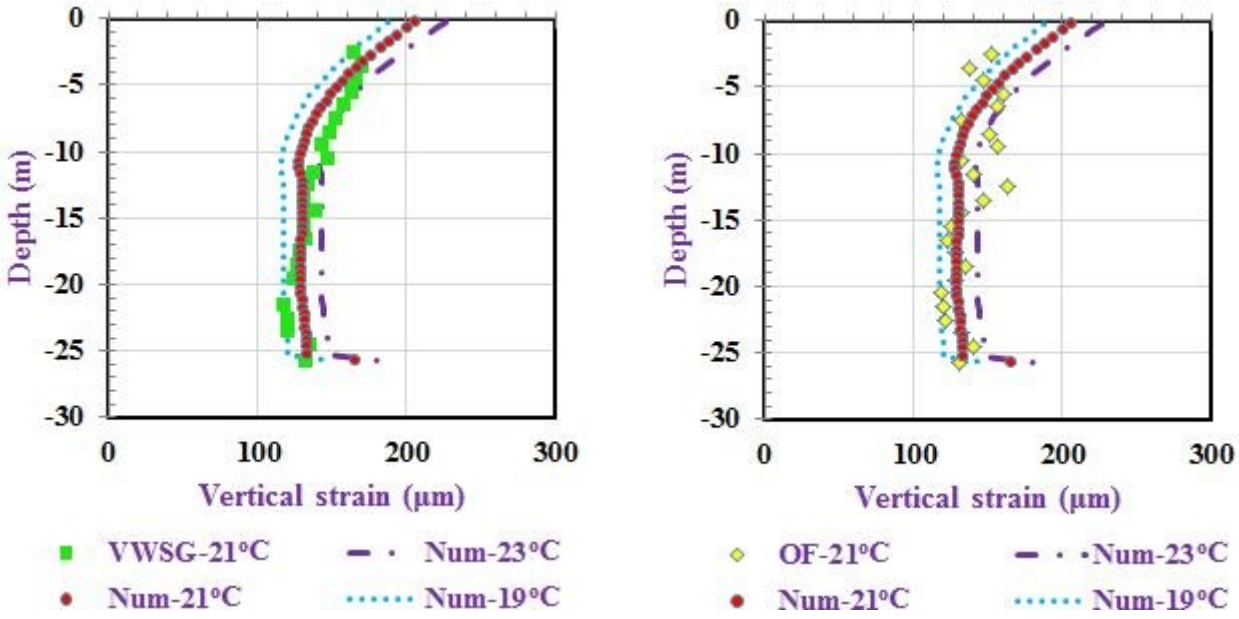

Figure 5.22 Vertical strain in the pile versus depth at 3°C (T1)

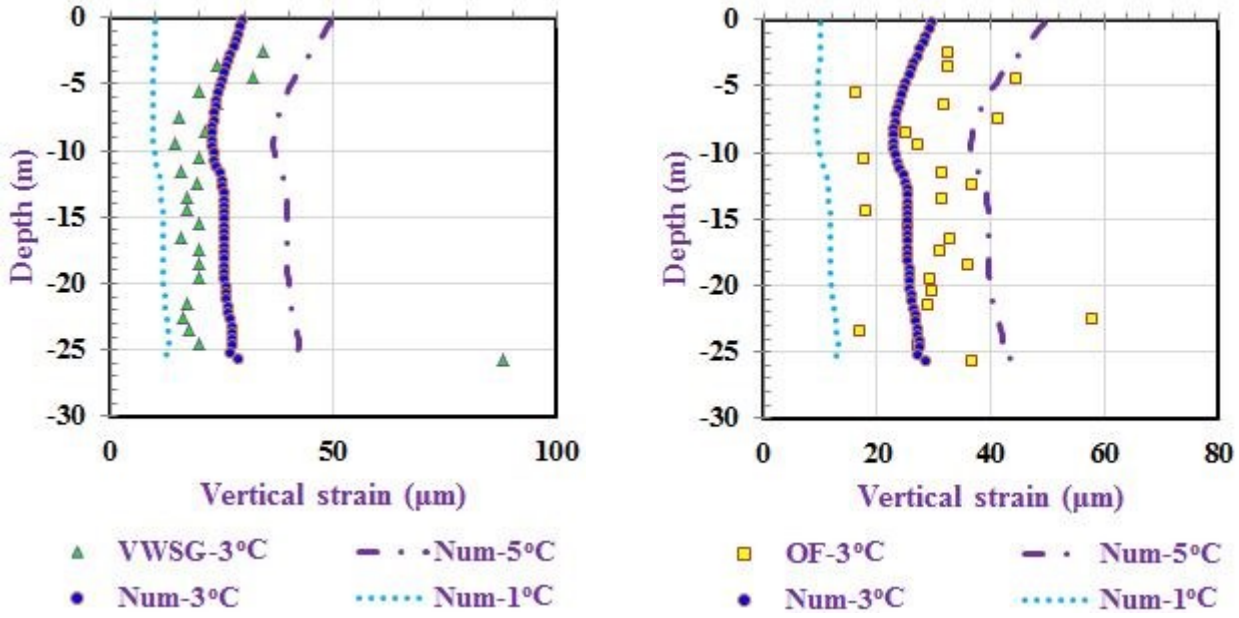

Figure 5.23 Vertical strain in the pile versus depth at 13.4°C (T1)

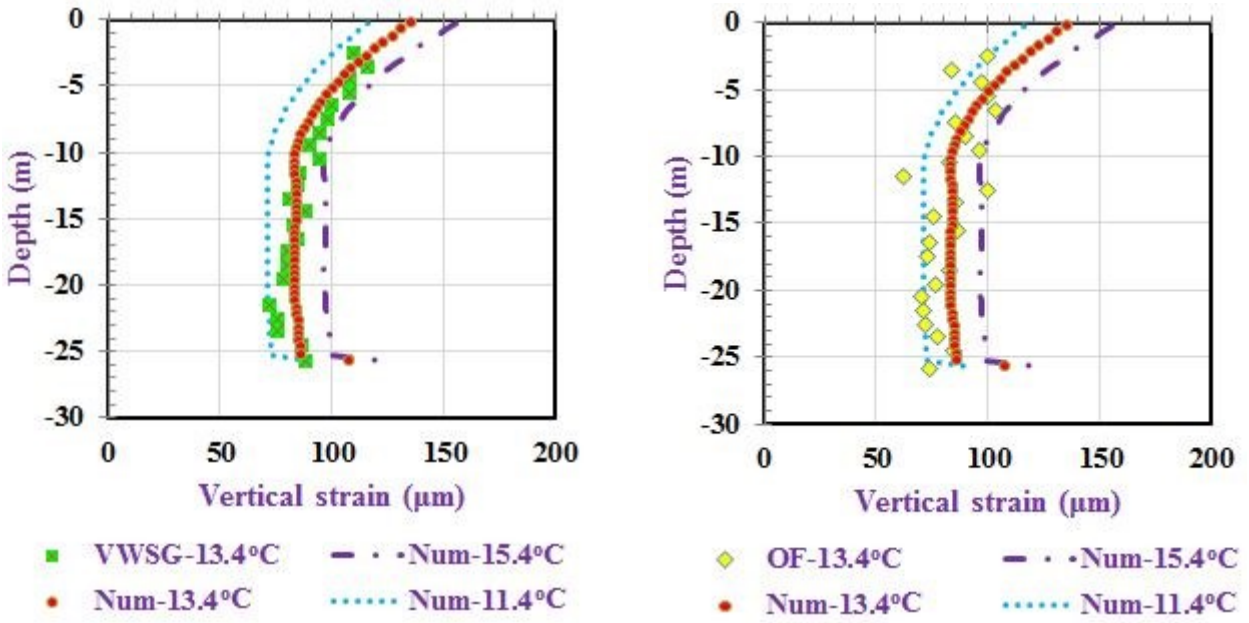

5.2.2.3 Stress

In addition to improved predictions of vertical strains, the anisotropic elastic model also provides improved predictions of vertical stresses. Figure 5.24 presents the vertical stress versus depth at 13.4°C. Anisotropic soils are located between depth of 12 m and 25.5 m. The predicted vertical stresses in the pile are nearly constant from 12 m to 22 m (in soil B) and then they slightly decrease to 1.5 MPa at the depth of 25.5 m.

Negative shear stresses (Figure 5.25) develop in the soils A1 and A2 at the end of heating period. In the soil B the shear stresses are nearly equal to zero while they become slightly positive in soil C. However, the magnitude of the positive shear stress in soil C is insignificant.

Figure 5.24 Vertical stress in the pile versus depth at 13.4°C (T1)

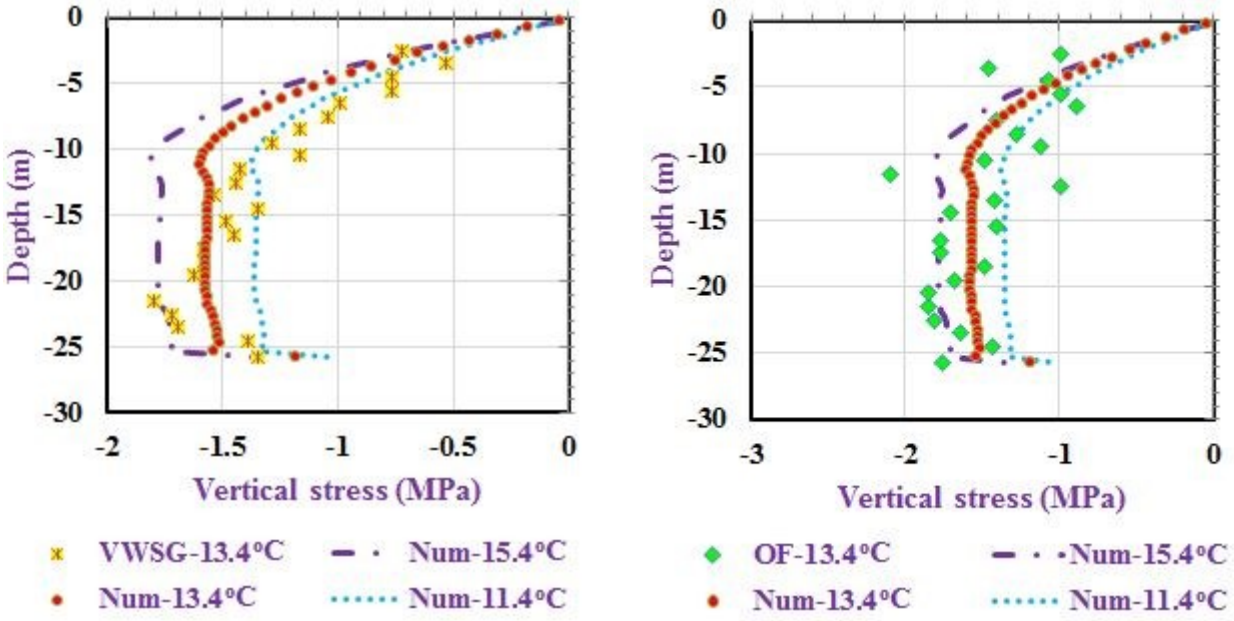

Figure 5.25 Shear stresses next to pile versus depth at 21°C and 3°C (T1)

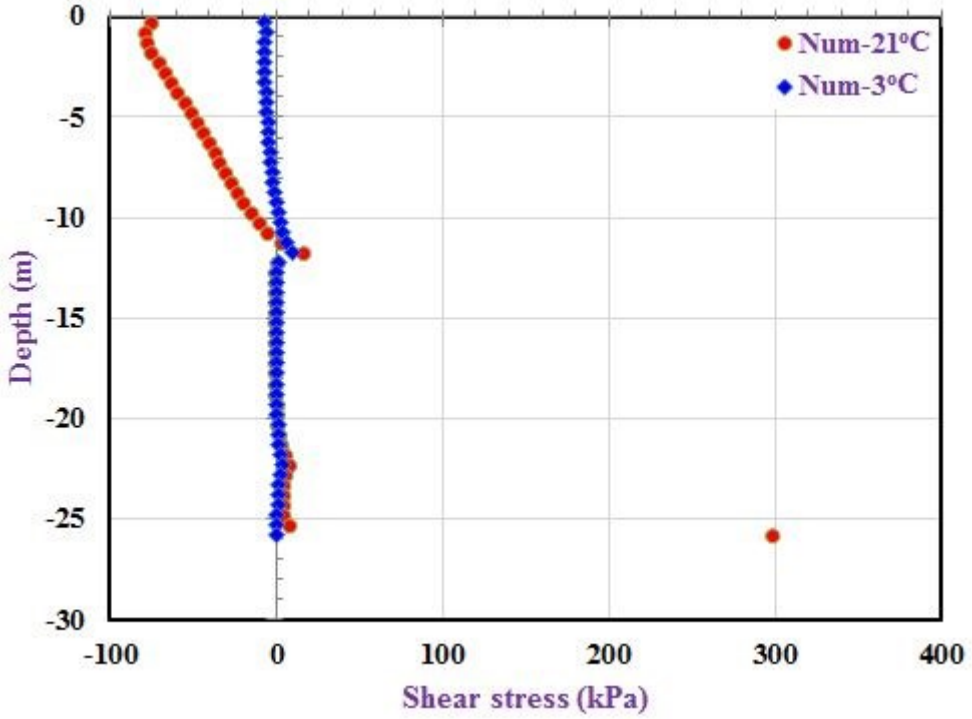

5.3 The behavior of HEP due to mechanical and thermal loading (T7)

During test T7, the HEP was subjected to a mechanical load in the form of a vertical force, which increased approximately linearly to 1000 kN during eight months. The corresponding temperature history was shown in Figure 4.4. The vertical force of 1000 kN remained applied at the pile head during the heating and cooling cycles. The HEP was heated to a maximum of 14^{o}C, and cooled down to 2^{o}C.

5.3.1 Isotropic elastic model

5.3.1.1 Displacement

Vertical displacements of the pile head and tip versus time and depth are shown in Figures 5.26 and 5.27 respectively. The end of the mechanical loading corresponds to the vertical force of 1000 kN, the predicted corresponding vertical head displacement is –0.7 mm (Figure 5.26). At the maximum temperature of 14^{o}C, the predicted head displacement ranged from 1.4 mm (for $\Delta T = 12^{o}C$) to 2.2 mm (for $\Delta T = 14^{o}C$). The pile tip displacement is almost zero at the end of the mechanical load step, while it is approximately equal to 0.11 mm at the end of heating period. In Figure 5.27, the null point is found at 25 m depth at the peak temperature of 14^{o}C. At the end of cooling phase (2^{o}C), no null point is found.

5.3.1.2 Strain

Compressive strains are predicted to develop at the end of mechanical loading (Figure 5.28) with the minimum value of –50 μm at the pile head. At the peak temperature of 14^{o}C, there is a very good agreement between the experimentally measured and computationally predicted values. The maximum tensile strain due to the combined mechanical and thermal loading develops at the pile tip. It is noted that the vertical thermal strain in Figure 5.28 was obtained by deducting mechanically induced strain from those induced by a combined thermal and mechanical loads. Figure 5.29 shows the upper and lower limit of the vertical strain in the pile versus depth in comparison to the measured values.

Figure 5.26 Vertical displacements of the pile head and tip versus time (T7)

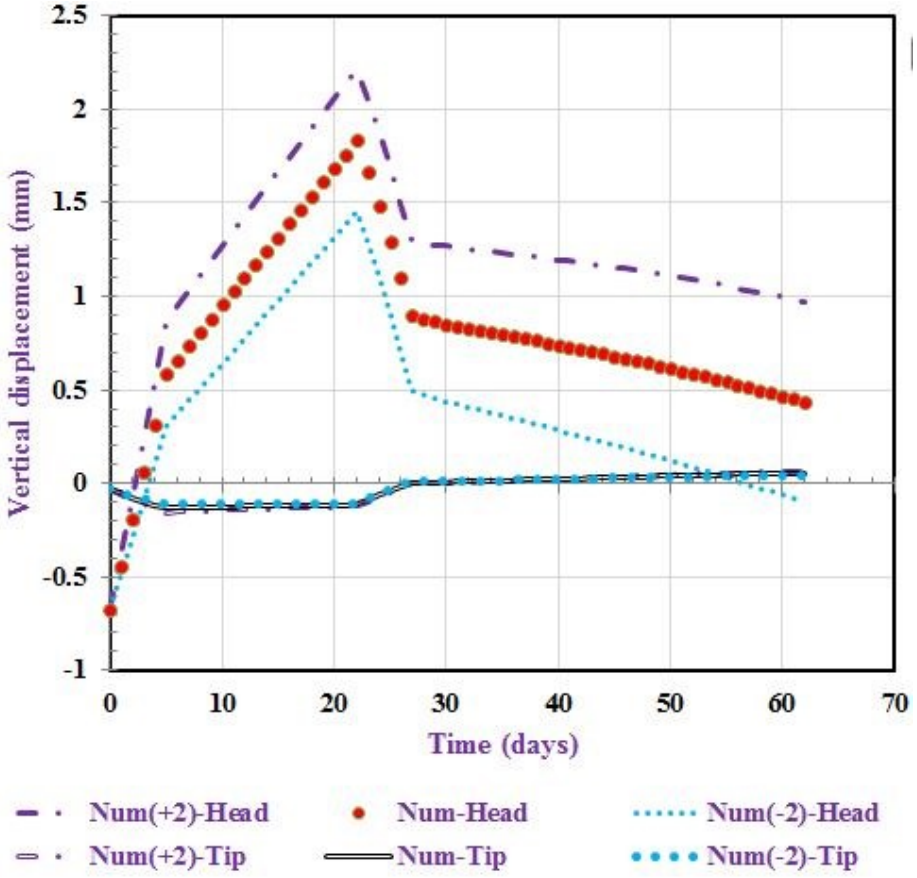

Figure 5.27 Vertical displacement of the pile with depth at 14°C and 2°C (T7)

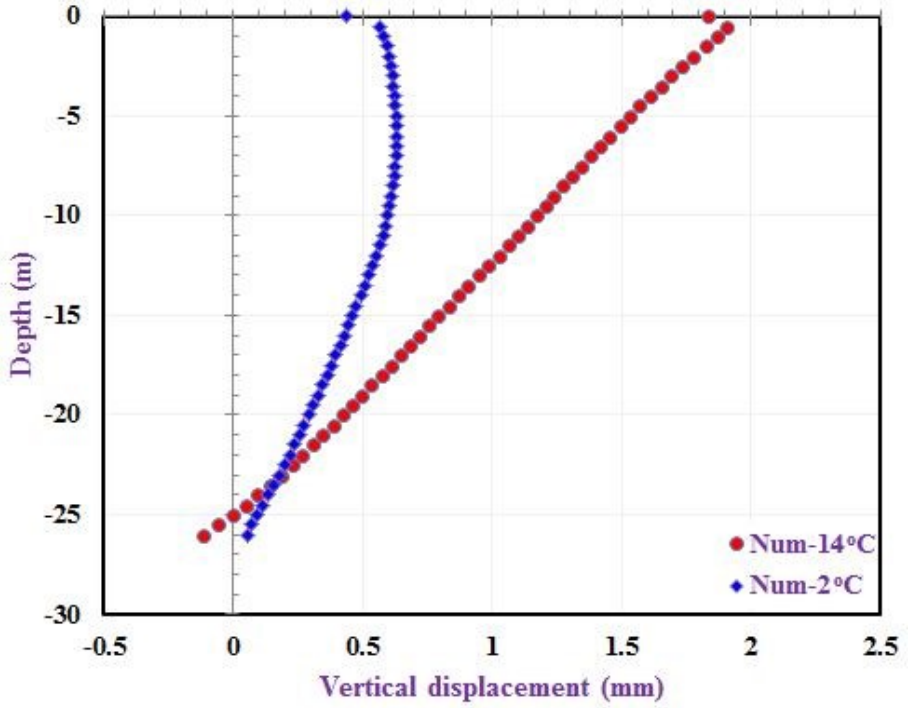

Figure 5.28 Vertical strain in the pile versus depth at 14°C (T7)

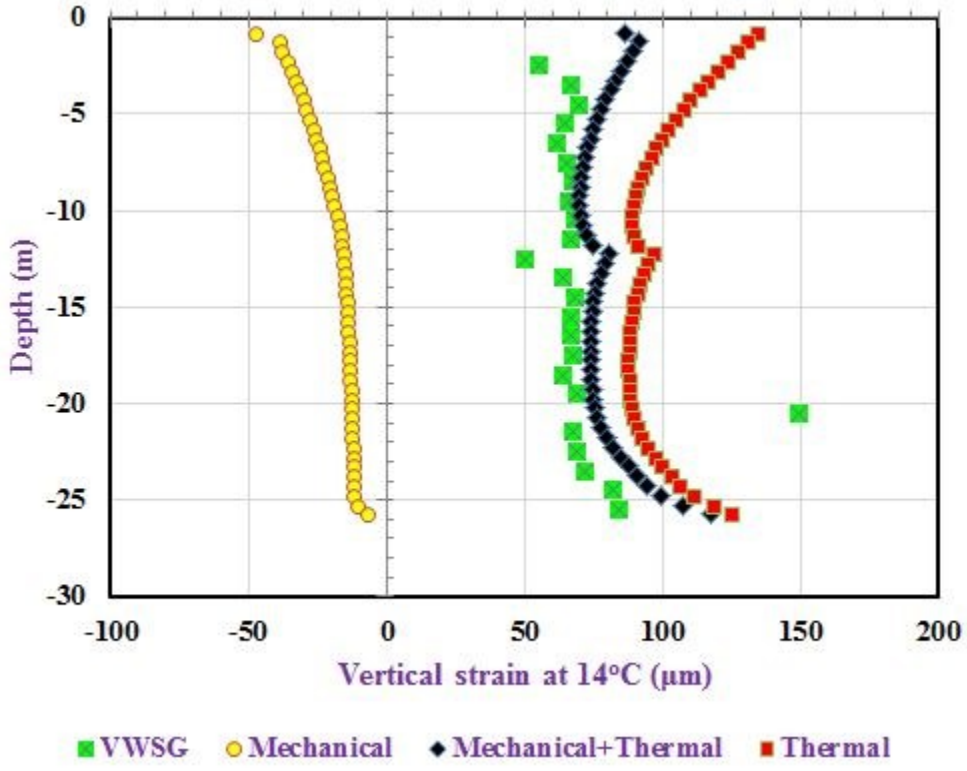

Figure 5.29 Vertical strain in the pile versus depth at the end of heating phase (T7)

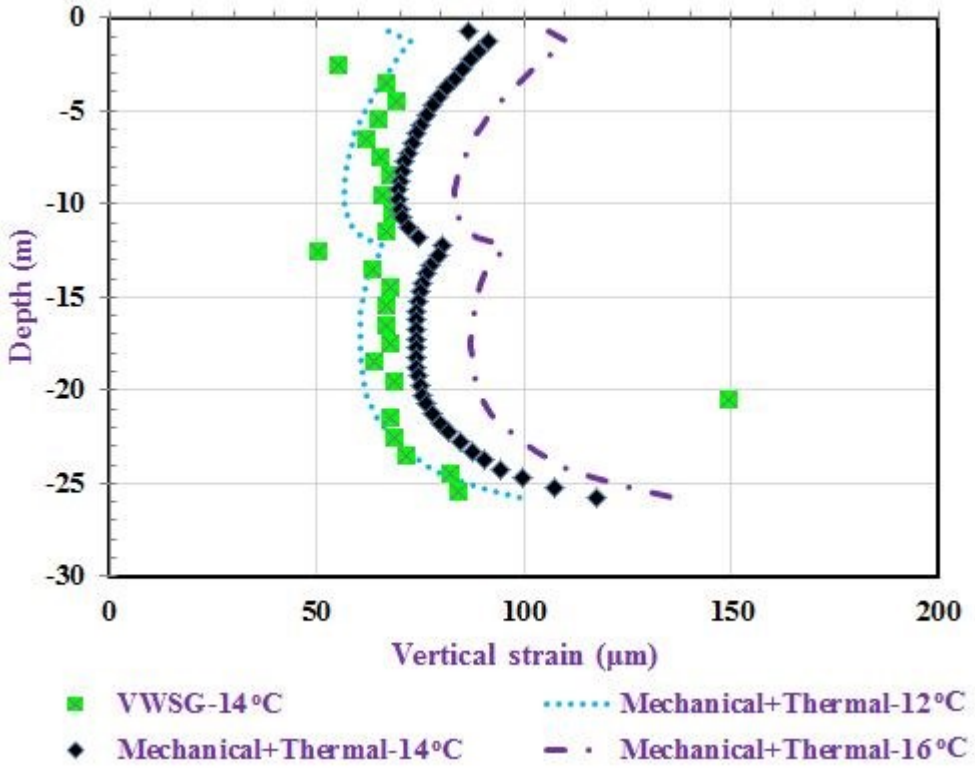

At the minimum temperature of 2°C, the predicted vertical strains in the pile are compressive from the pile head to a depth of 6 m. Below this depth, the vertical strains are tensile with the maximum value of 45 μm at the pile tip (Figure 5.30). The lower limit of the vertical strain at the end of cooling phase is very close to the experimental data (Figure 5.31).

Figure 5.30 Vertical strain in the pile versus depth at 2°C (T7)

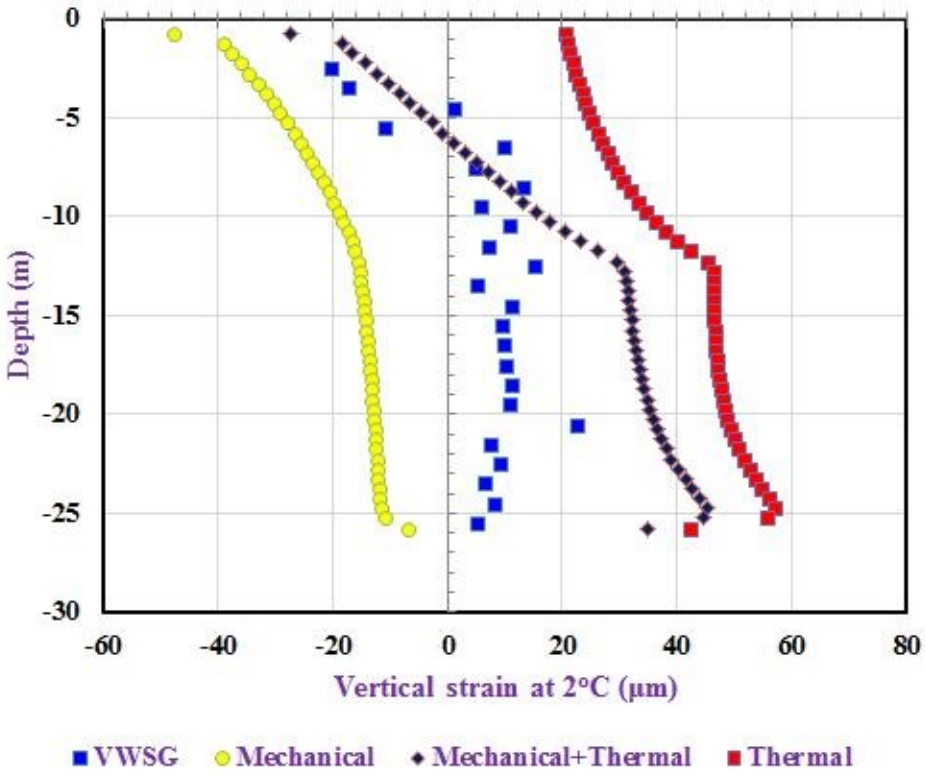

5.3.1.3 Stress

The stresses induced by the combined mechanical and thermal loads are presented in Figures 5.32 and 5.33. The predicted maximum compressive stress of 0.92 MPa occurred at the pile tip due to the restraint generated by the sandstone layer (Figure 5.32). The vertical stresses due to the mechanical loading decrease with depth, while the vertical stresses induced by the thermal load increase with depth for the most part (Figure 5.32). Thus, the stresses due to the mechanical load are smaller than the stresses due to thermal loading only. However, above the depth of 4 m vertical stresses due to the mechanical load are larger than those due to the thermal load.

Figure 5.31 Vertical strain in the pile versus depth at the end of cooling phase (T7)

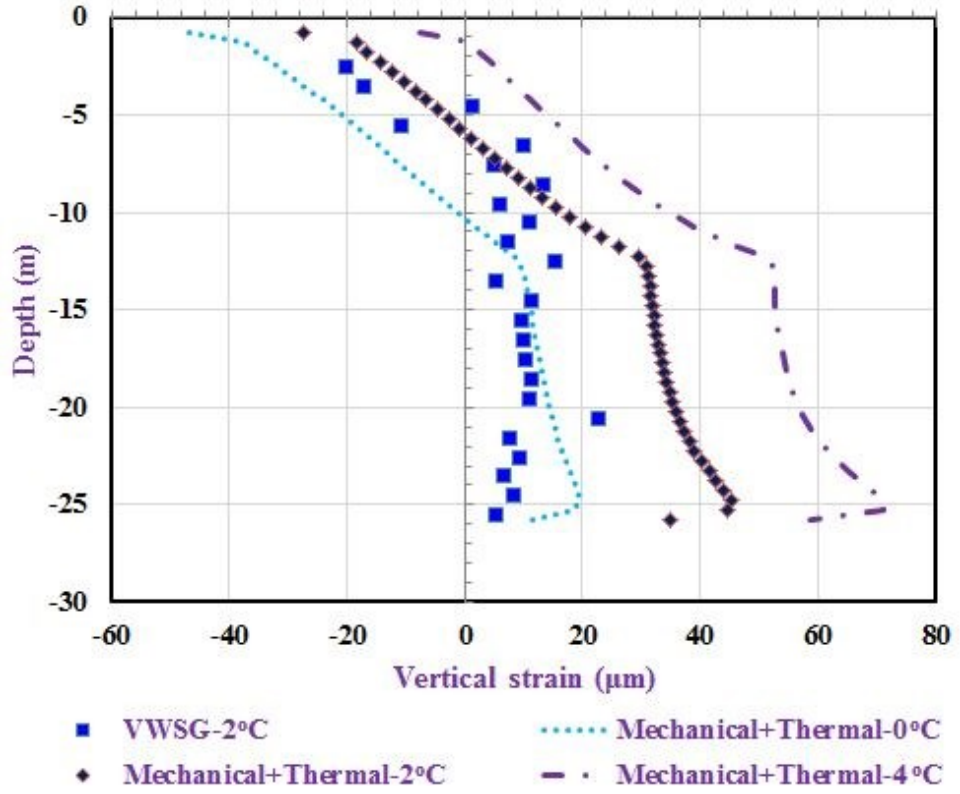

Figure 5.32 Vertical stress in the pile versus depth at 14°C (T7)

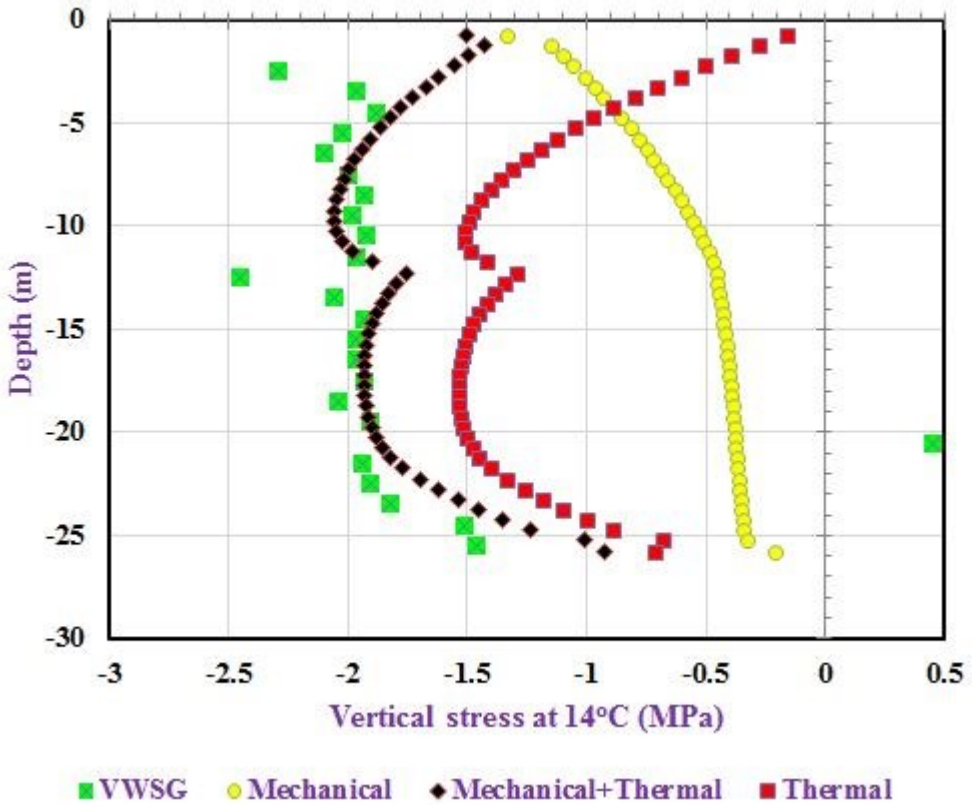

Figure 5.33 Vertical stress in the pile versus depth at the end of heating cycle (T7)

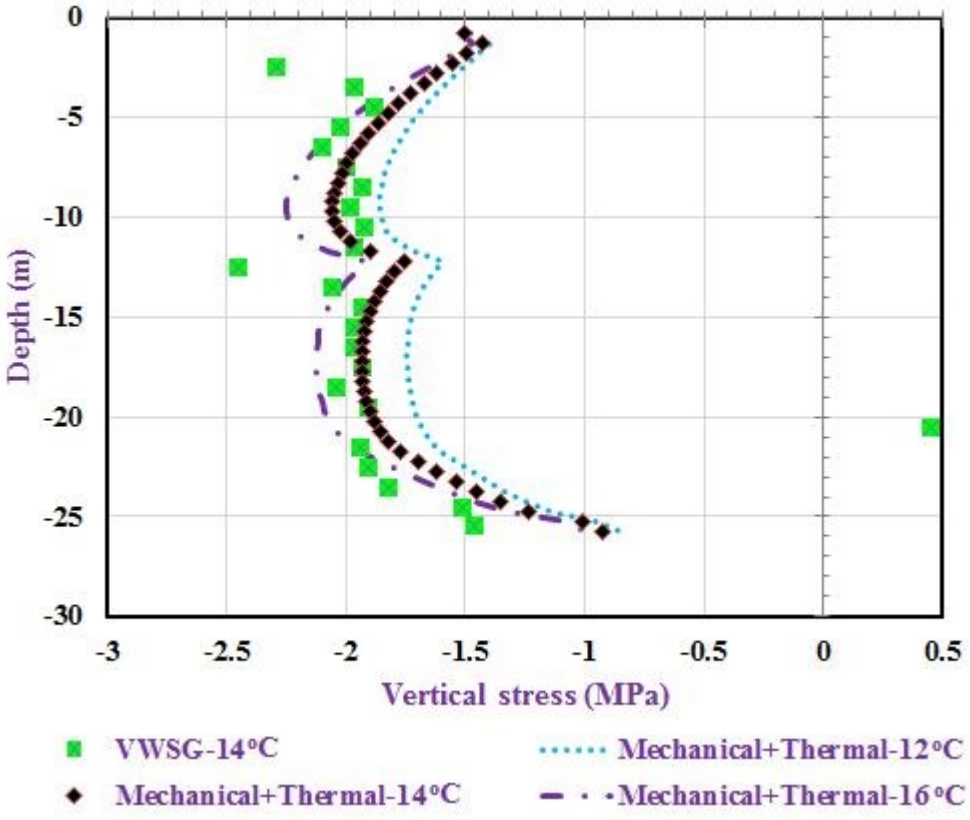

Figure 5.34 Shear stress next to pile versus depth at 14°C and 2°C (T7)

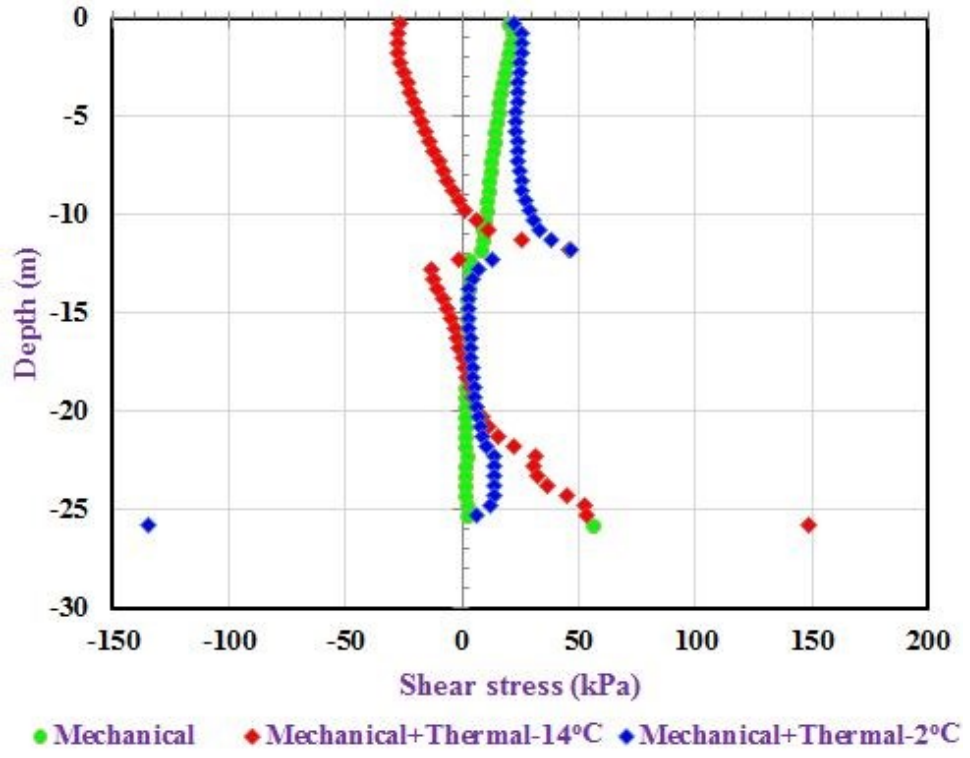

The shear stresses in soil B and C are almost zero at the end of mechanical loading as shown in Figure 5.34. They are positive in layers A1 and A2 with the maximum magnitude of 22 kPa. At the end of heating phase (14^{o}C), the negative shear stresses in the upper part of the pile decreases and change into positive sign until it reach the boundary of the soil layer and jump in the negative shear stress again. At 2^{o}C of the cooling phase, shear stresses are positive and below 12 m depth, it is fairly constant.

5.3.1.4 Equivalent soil

Figure 5.35 depicts vertical displacements of the pile head and tip versus time after the pile embedded in the isotropic elastic soils has been mechanically loaded. The tip displacement is similar to the previous cases, with the largest displacement of approximately – 0.12 mm. The vertical displacement at the pile head is also similar to the previous cases with the maximum of 1.8 mm at 14^{o}C. Vertical displacement along the length of the pile is shown in Figure 5.36 for the temperatures of 14^{o}C and 2^{o}C. The null point of the pile was located approximately at 24.5 m depth at the end of heating period. It changed the location to about 25.5 m depth at the end of cooling phase.

Figure 5.35 Vertical displacement of the pile head and tip versus time (T7)

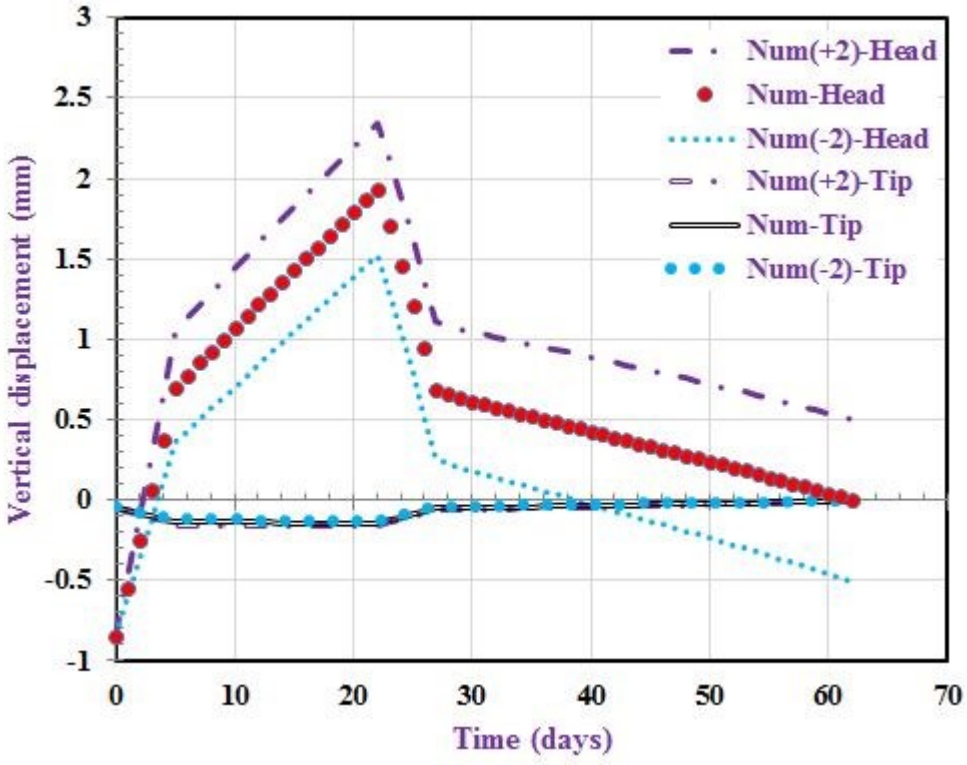

Figure 5.36 Vertical displacement of the pile versus depth at 14°C and 2°C (T7)

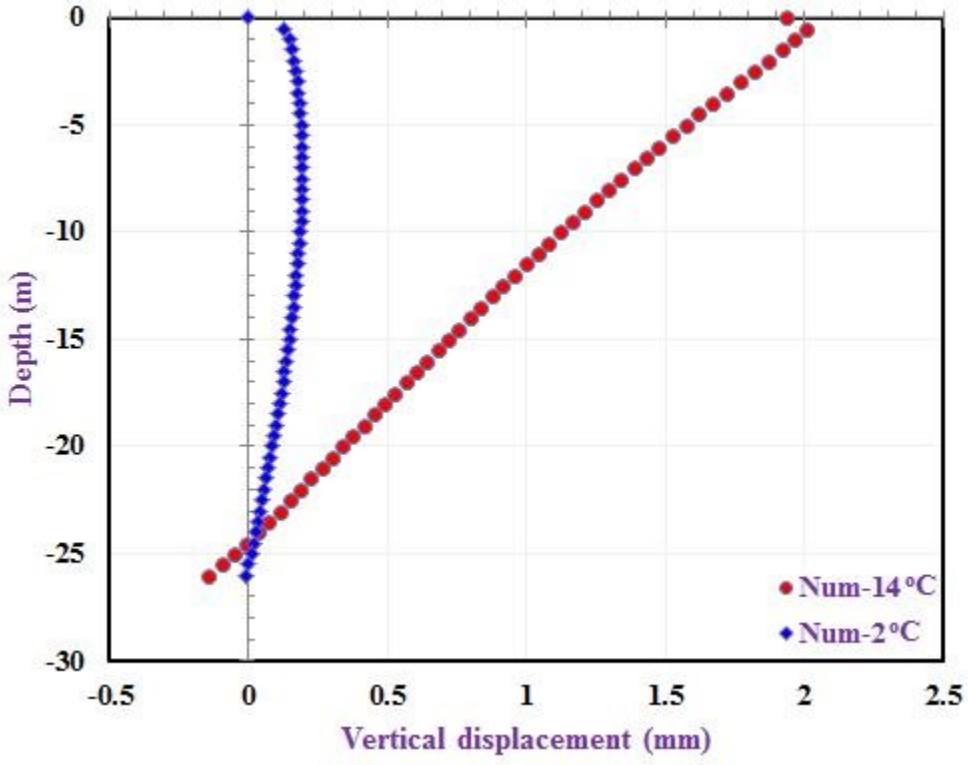

Figure 5.37 Vertical strain in the pile versus depth at 14°C (T7)

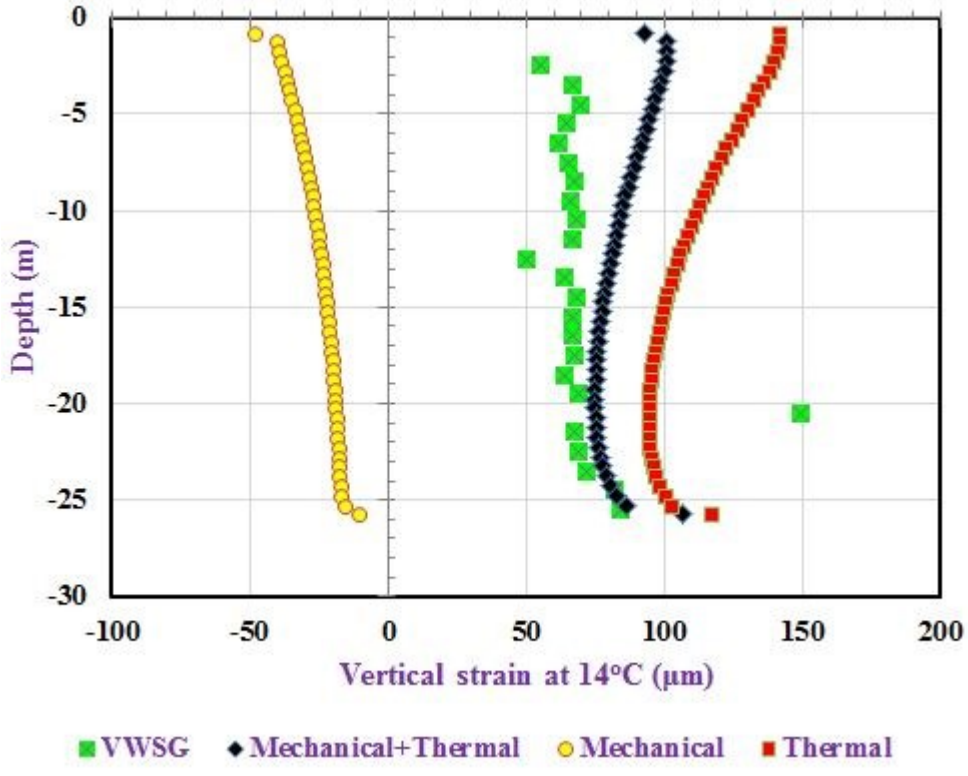

Figures 5.37 and 5.38 depict the vertical strain in the pile versus depth obtained by the numerical model and from the field data. The predicted vertical strains in the top part of pile are over estimated compared to the measured data. Approximately from the depth of 15 m to the pile tip, the numerical solution gives an excellent prediction of the measured values.

Figure 5.38 Vertical strain in the pile versus depth at the end of heating phase (T7)

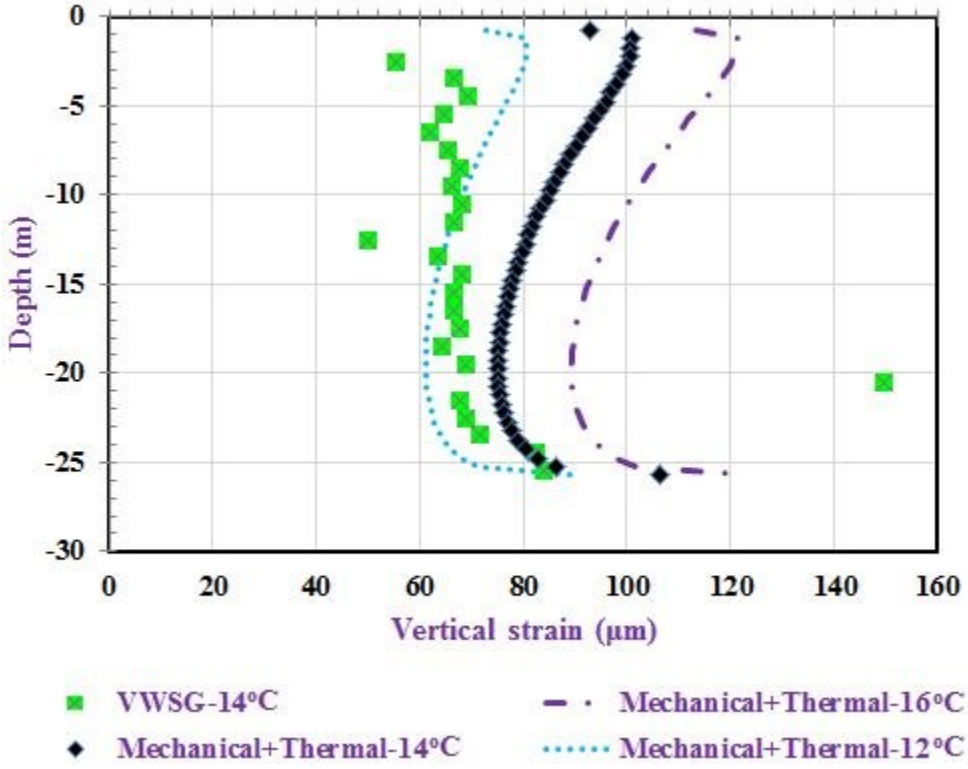

At the minimum temperature of 2°C, the predicted vertical strains in the pile are compressive from the pile head to a depth of 7 m. Below this depth, the vertical strains are tensile with the maximum value of 19 μm at the pile tip (Figure 5.39). The experimental data are located in within the lower and upper limits of the vertical strain at the end of cooling phase. (Figure 5.40).

Figure 5.39 Vertical strain in the pile versus depth at 2°C (T7)

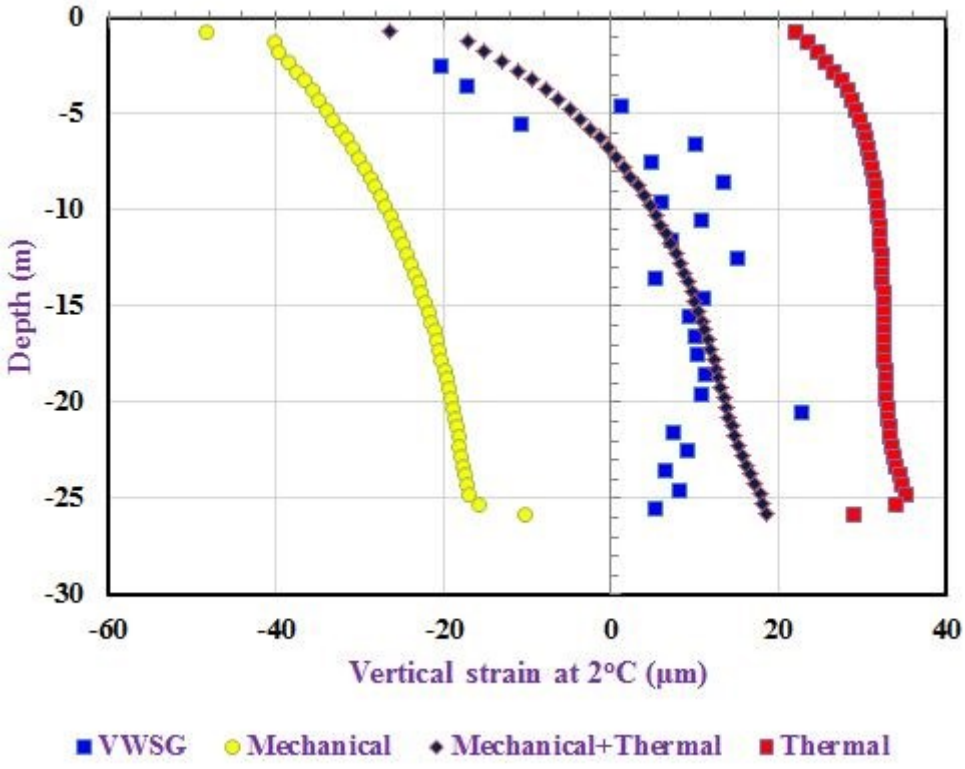

Figure 5.40 Vertical strain in the pile versus depth at the end of cooling phase (T7)

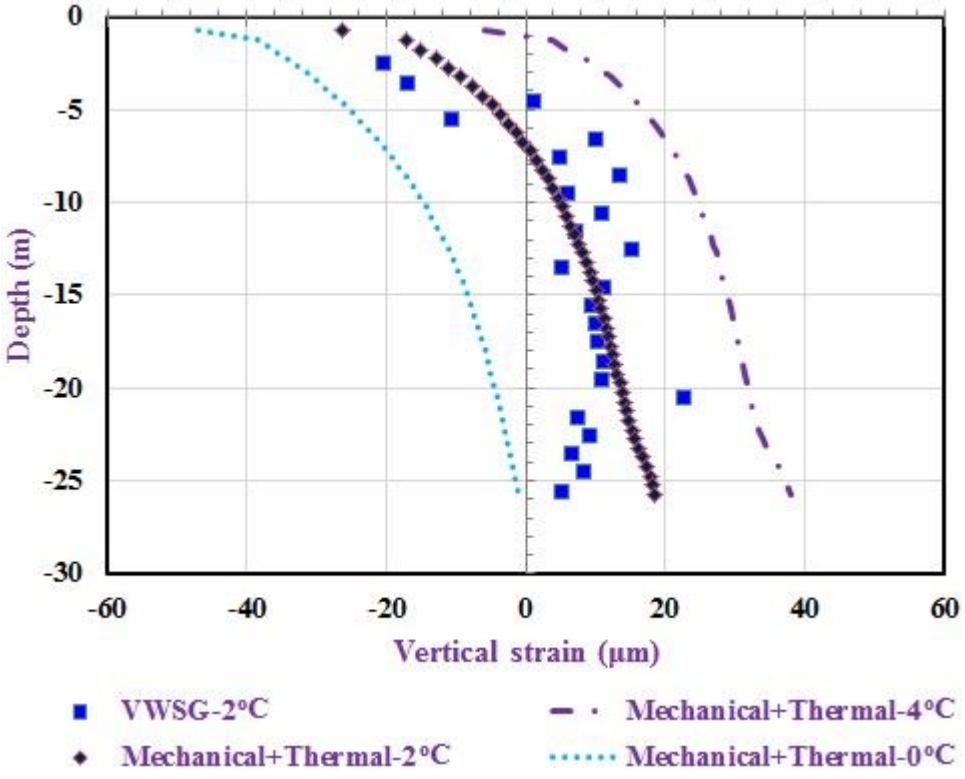

Figures 5.41 and 5.42 depict the actual, lower and upper limits vertical stress in the pile versus depth at 14°C obtained by the numerical model and the field data (VWSG). The predicted vertical stresses in the top part of the pile are under estimate the measured data. From approximately 15 m depth, the numerical solution provides a very good prediction of the measured data. The predicted maximum vertical stress of 2.1 MPa was found at the depth of 20 m.

The shear stresses that develop in the equivalent homogeneous soil are plotted versus depth at the end of heating and cooling phases in Figure 5.43. Negative shear stresses developed in the upper part of the pile. They reversed to positive values at the depth of 21 m at the end of the heating period. At the end of the cooling phase, the maximum shear stresses occurred at the pile head. Shear stress was nearly equal to zero below the depth of 15 m. The largest shear stress (240 kPa) occurred at the pile tip because pile tip is embedded into the bedrock over the length of 0.5 m.

Figure 5.41 Vertical stress in the pile versus depth at 14°C (T7)

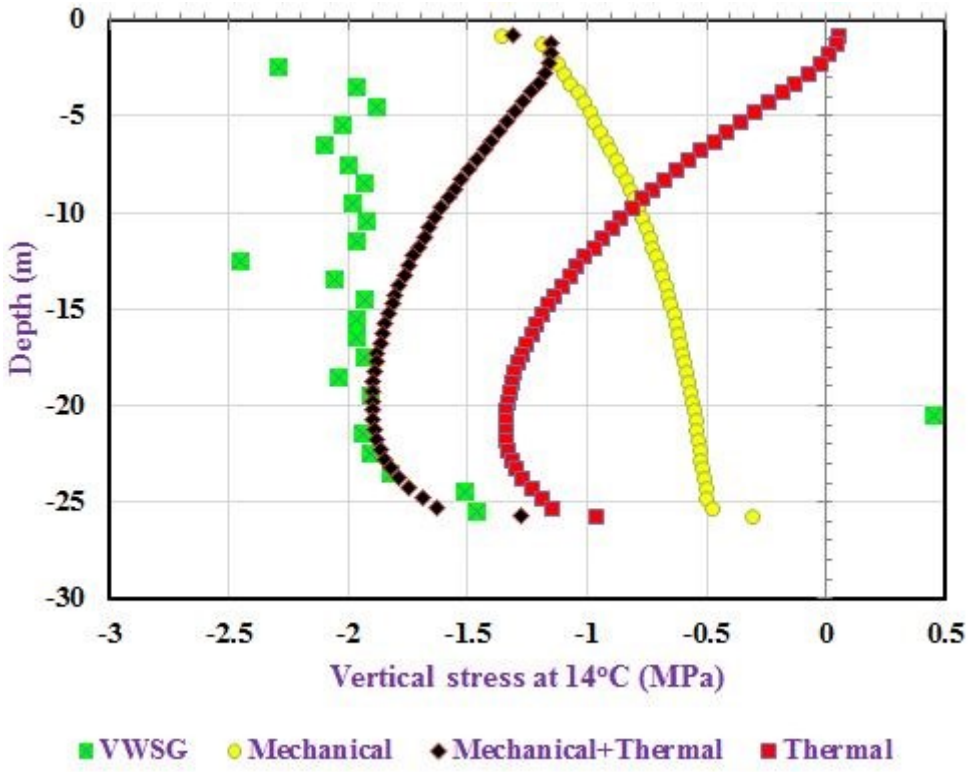

Figure 5.42 Vertical stress in the pile versus depth at the end of heating phase (T7)

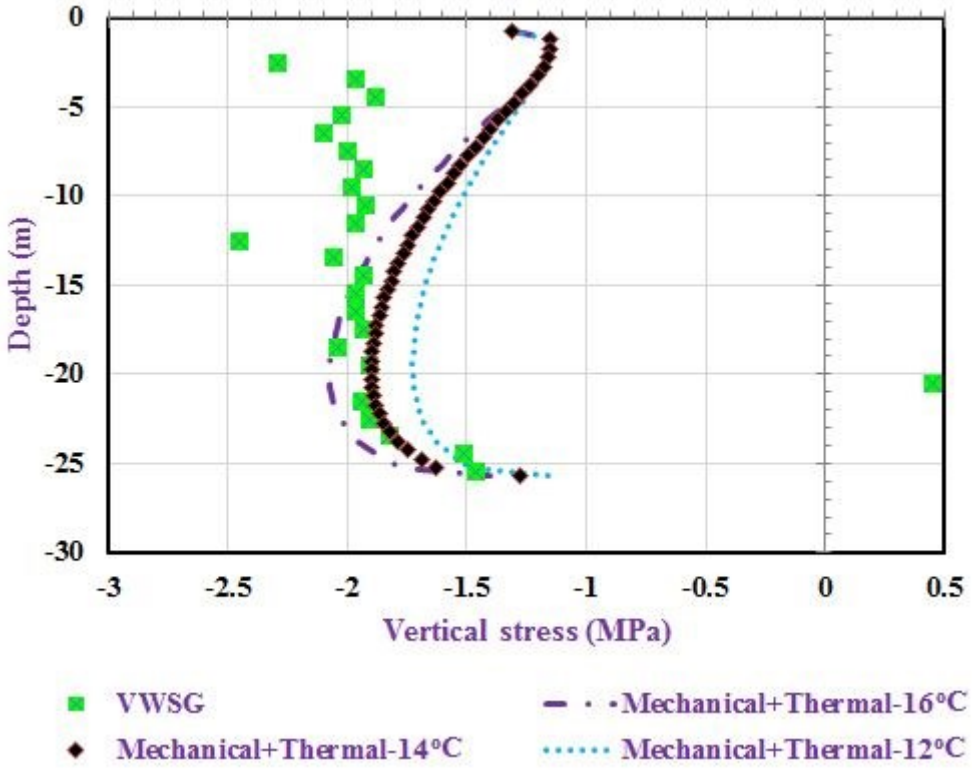

Figure 5.43 Shear stress next to pile versus depth at 14°C and 2°C (T7)

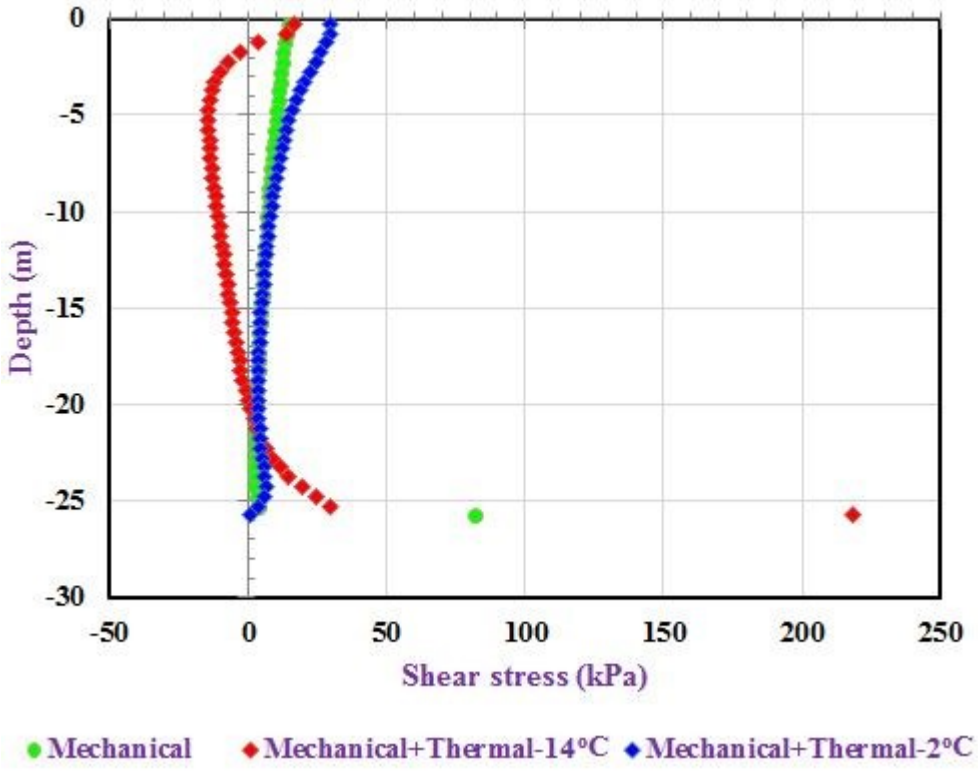

5.3.2 Anisotropic elastic model

5.3.2.1 Displacement

Vertical displacements of the pile head and tip versus time and depth for anisotropic elastic model are shown in Figure 5.44 and 5.45 respectively. At the end of the mechanical loading, the downward displacement of the pile head is 0.9 mm. A maximum upward displacement increased equal to 2 mm at the end of the heating phase. For the pile tip, the displacement is almost zero at the end of mechanical loading, while it is approximately equal to 0.14 mm during the heating period.

Figure 5.44 Vertical displacements of the pile head and tip versus time (T7)

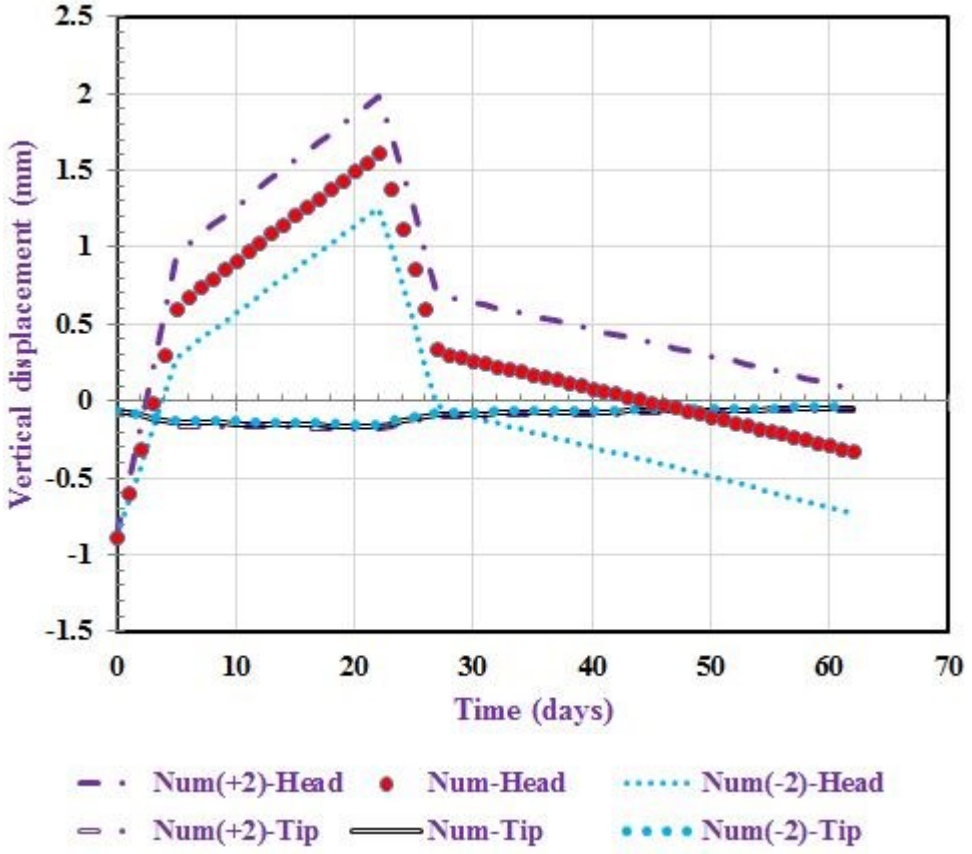

5.3.2.2 Strain

There is an improvement in the predicted vertical strain of the pile at the end of the heating phase (14^{o}C), which is shown in Figure 5.46. Figure 5.47 shows the upper and lower limits of the vertical strain in the pile versus depth as they compare to the experimental data.

Figure 5.45 Vertical displacement of the pile versus depth at 14°C and 2°C (T7)

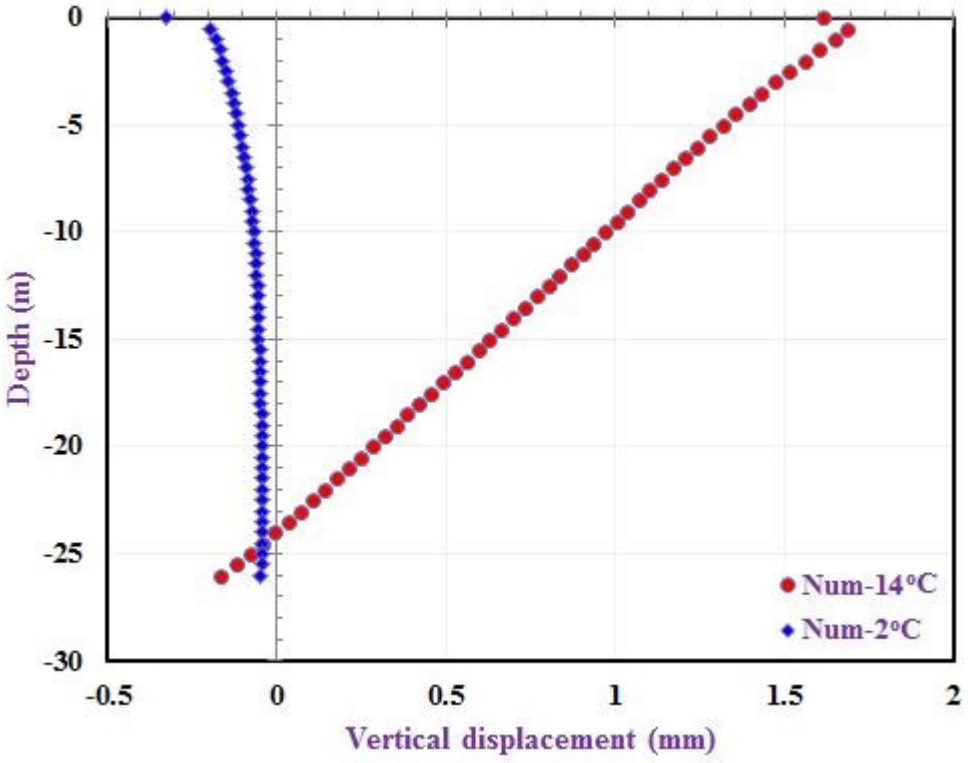

Figure 5.46 Vertical strain in the pile versus depth at 14°C (T7)

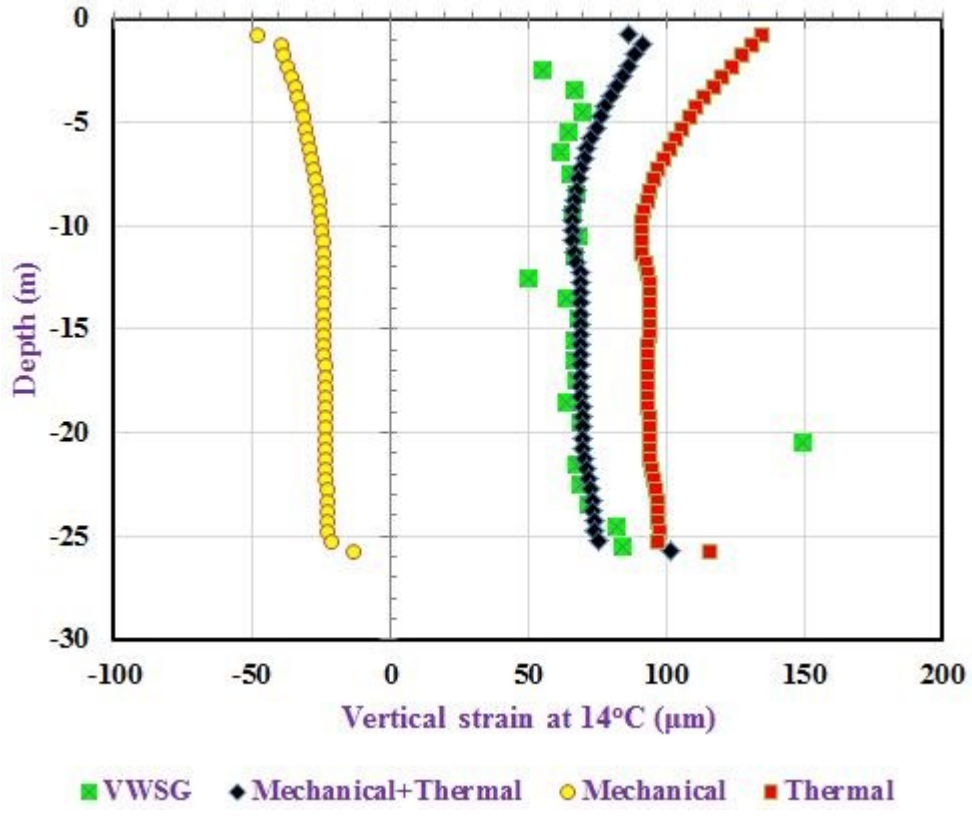

Figure 5.47 Vertical strain in the pile versus depth at the end of heating phase (T7)

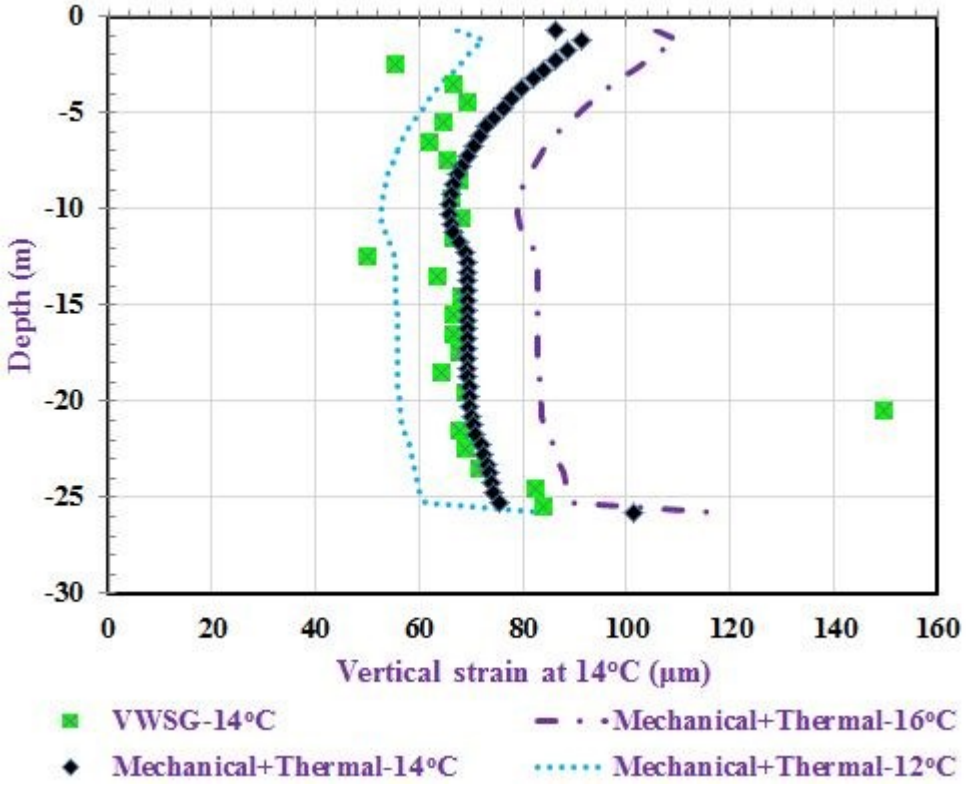

Figure 5.48 Vertical strain in the pile versus depth at 2°C (T7)

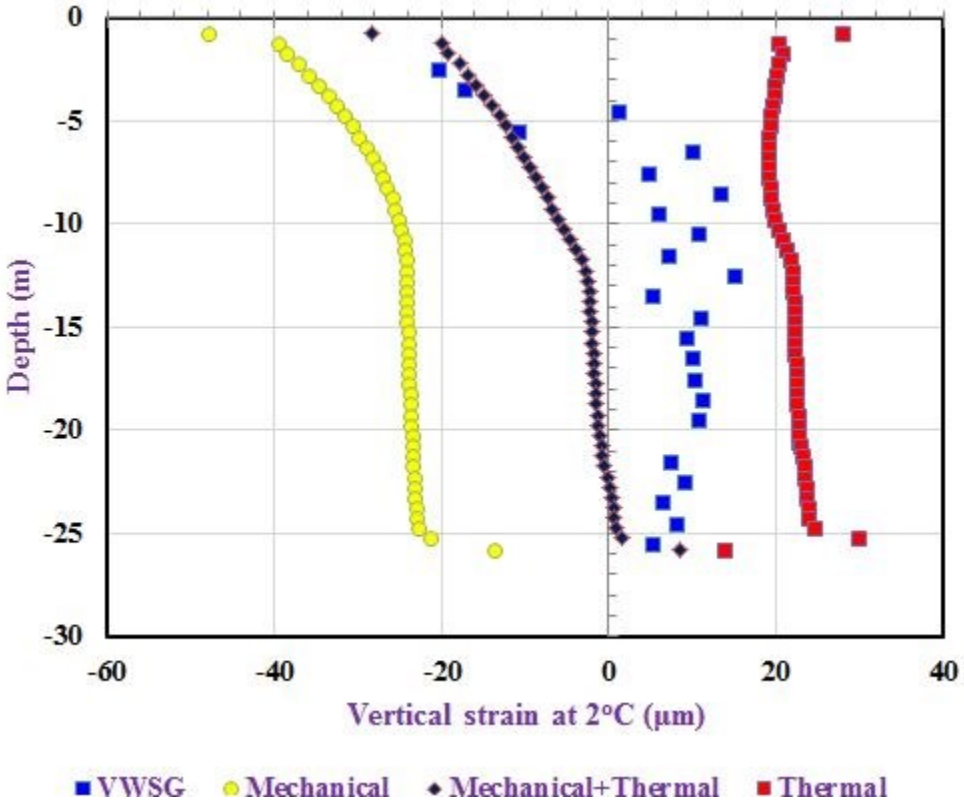

At the end of cooling phase (2°C), the predicted vertical strains in the pile are compressive from the pile head until a depth of 13 m. Below this depth the vertical strains are tensile (Figure 5.48). Figure 5.49 depicts lower and upper bounds for the vertical strain in the pile at the end of cooling period.

Figure 5.49 Vertical strain in the pile versus depth at the end of cooling phase (T7)

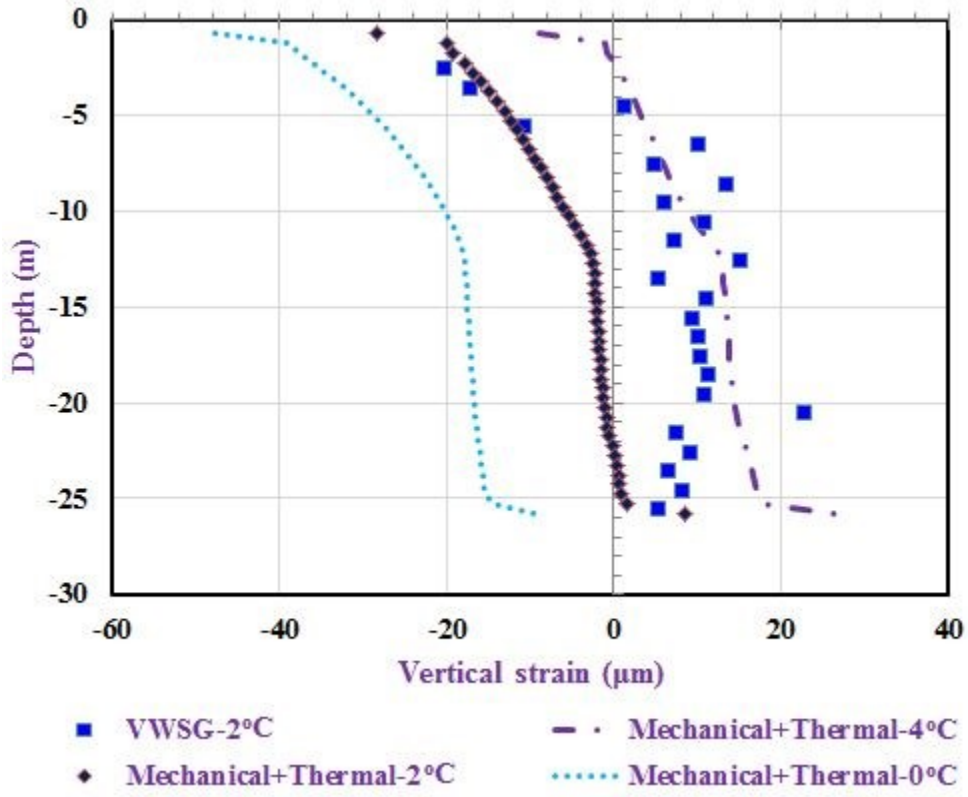

5.3.2.3 Stress

The compressive stresses induced by the mechanical and thermal loads are presented in Figures 5.50 and 5.51. The predicted vertical stresses due to the mechanical and thermal loads increase with depth within soils A1 and A2. They remain fairly constant in soils B and C. The predicted vertical stress reaches a minimum value of 1.4 MPa at the pile tip. Upper and lower and bounds for the predicted vertical stresses at the end of heating phase are depicted in Figure 5.51.

Figure 5.50 Vertical stress in the pile versus depth at 14°C (T7)

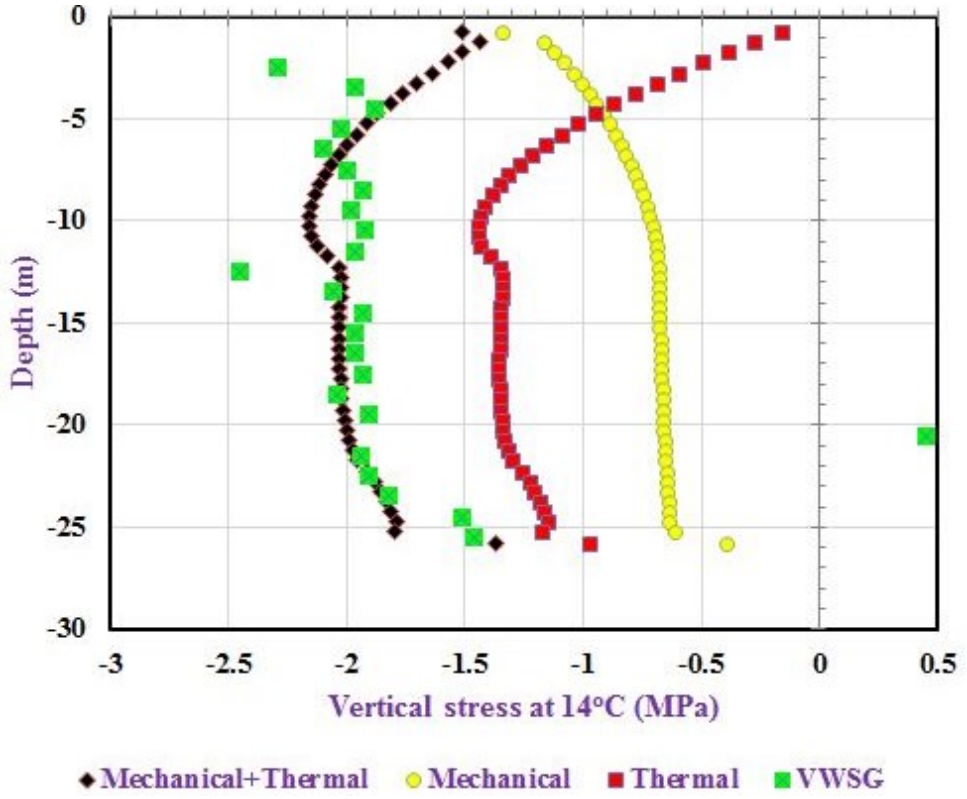

Figure 5.51 Vertical stress in the pile versus depth at the end of heating phase (T7)

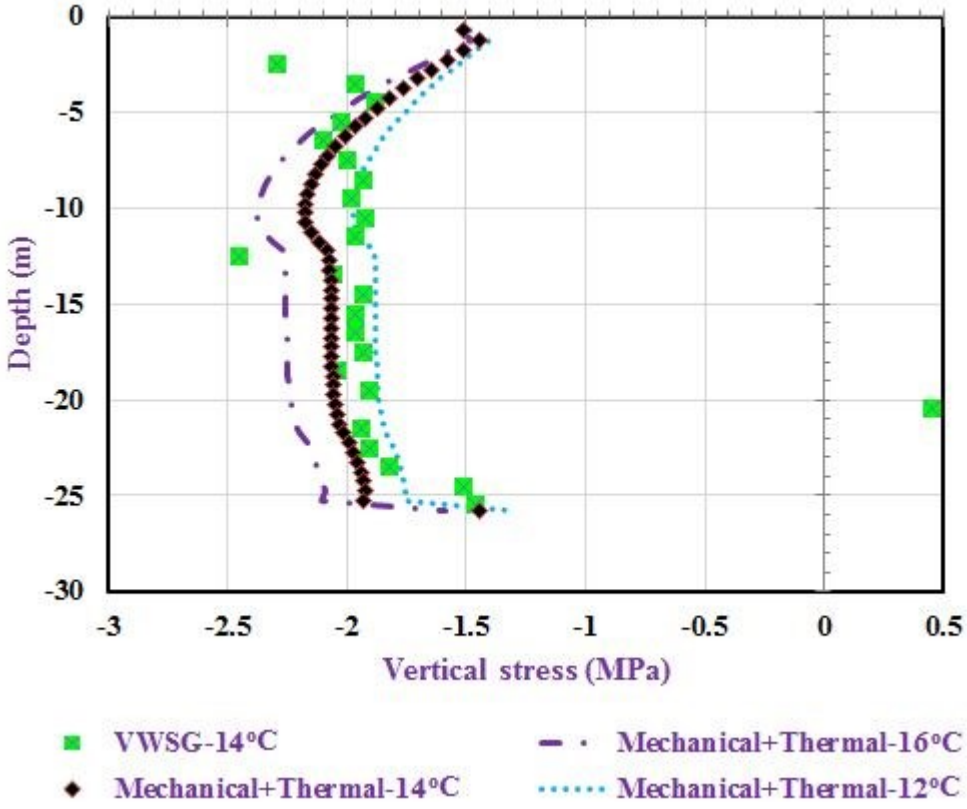

Negative shear stresses (Figure 5.52) develop in the soils A1 and A2 at the end of heating period (14°C). In the soil B the shear stresses are nearly equal to zero while they become slightly positive in soil C. However, the magnitude of the positive shear stress in soil C is insignificant. At the end of the cooling phase (2°C), the shear stresses are positive in the entire soil profile, but their magnitude is small.

Figure 5.52 Shear stress next to pile versus depth at 14°C and 2°C (T7)

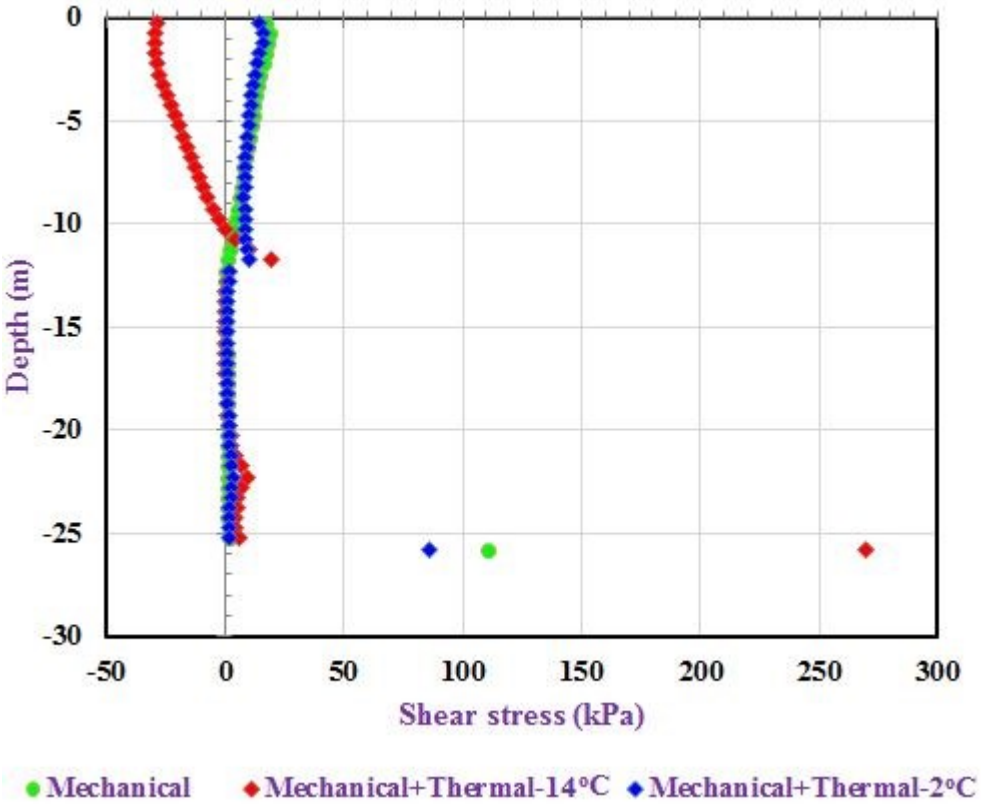

5.4 Discussion

5.4.1 Thermal loading only (T1)

Figure 5.53 shows the axial stress versus depth at 13.4°C reaches during the heating phase of a combined mechanical and thermal loading (test T7). While the HEP was still loaded up to 1000 kN over the time period of eight months, the temperature history imposed on the pile is equal to that of the test T1. The stresses induced by the thermal loading are depicted in Figure 5.53. And they correspond to those induced by the thermal loading only (Figure 5.9). It is noted that thermally induced stress in Figure 5.68 was computed by deducting the stresses induced by

mechanical load from those generated by both mechanical and thermal loads. Thus, for equal temperature histories imposed on the pile, the thermally induced stresses due to thermal load are equal to those extracted from a combined thermal and mechanical load.

Figure 5.53 Vertical stress in the pile versus depth at 13.4°C

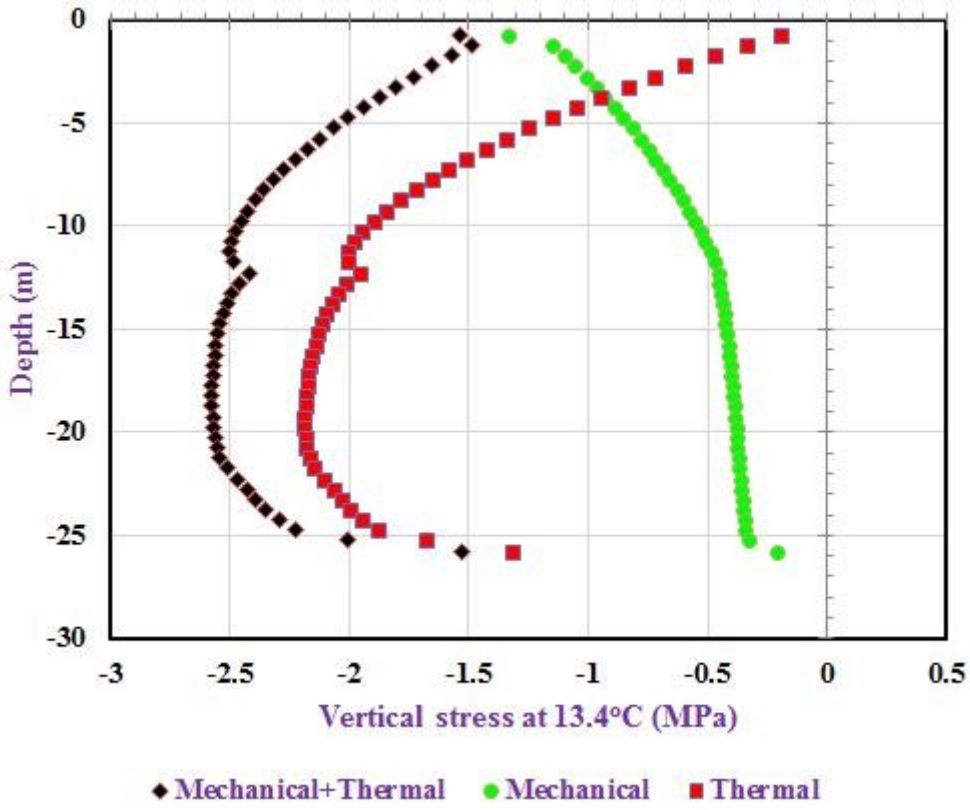

The displacements of the pile head in isotropic and anisotropic elastic soils are shown in Figure 5.54. The predicted displacements agree very well with the field measurements obtained by optical fibers. Most of the predicted head displacements are approximately 0.6 mm smaller than the measurement obtained by the extensometers during the heating phase. However, in the isotropic elastic layered soil profile, the maximum vertical head displacement of the pile is 1.2 mm less than the field measurements obtained by extensometers.

The predicted vertical strains in the pile versus depth at 13.4°C are presented in Figure 5.55. The strains predicted for the isotropic elastic layered soil profile are lower than the field measurements obtained by the VWSG. From the depth of 12 m to 22 m, the axial strains in the pile predicted by the anisotropic elastic layered soil system are almost constant with a slightly

increase after a depth of 22m. In both equivalent homogeneous soils (isotropic and anisotropic) the predicted strains in the pile seem to fit well with the experimental data.

Figure 5.54 Comparison of vertical displacements of the pile head versus time (T1)

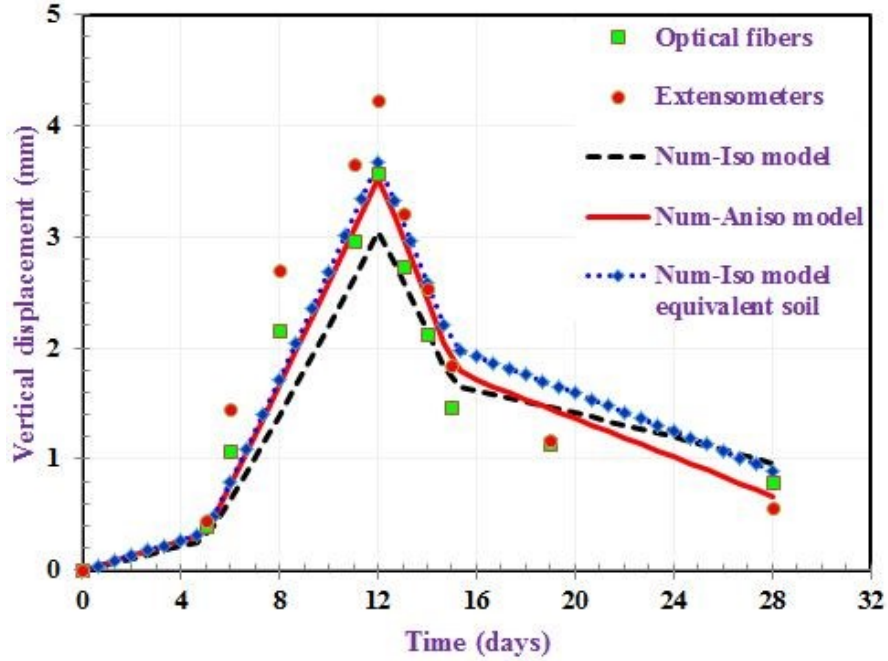

Figure 5.55 Comparison of vertical strains in the pile versus depth at 13.4°C (T1)

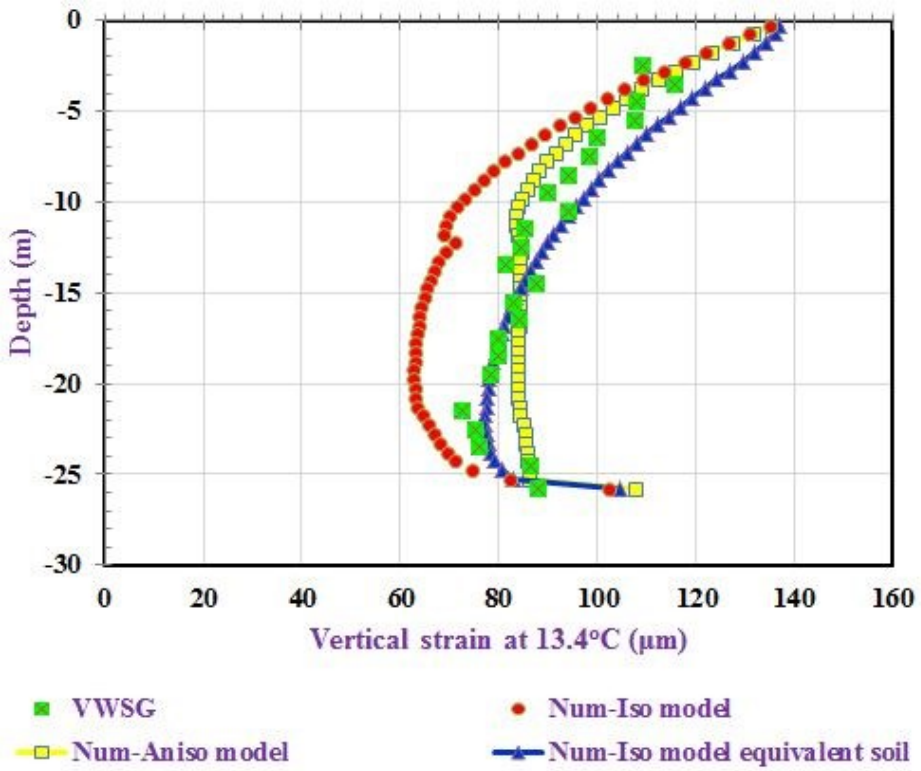

The vertical stress response depicted in Figure 5.56 is similar to the vertical strain response in the pile. The stresses predicted for isotropic elastic layered soil profile are larger than the field measurements obtained by the VWSG. The predicted axial stresses in the pile for anisotropic elastic layered soil profile are almost constant from the depth of 12 m to 22 m, which is followed by a slight stress increase below the depth of 22 m. In both equivalent soils (isotropic and anisotropic elastic) the predicted vertical stresses in the pile seem to fit well with the experimental data.

Figure 5.56 Comparison of vertical stresses in the pile versus depth (T1)

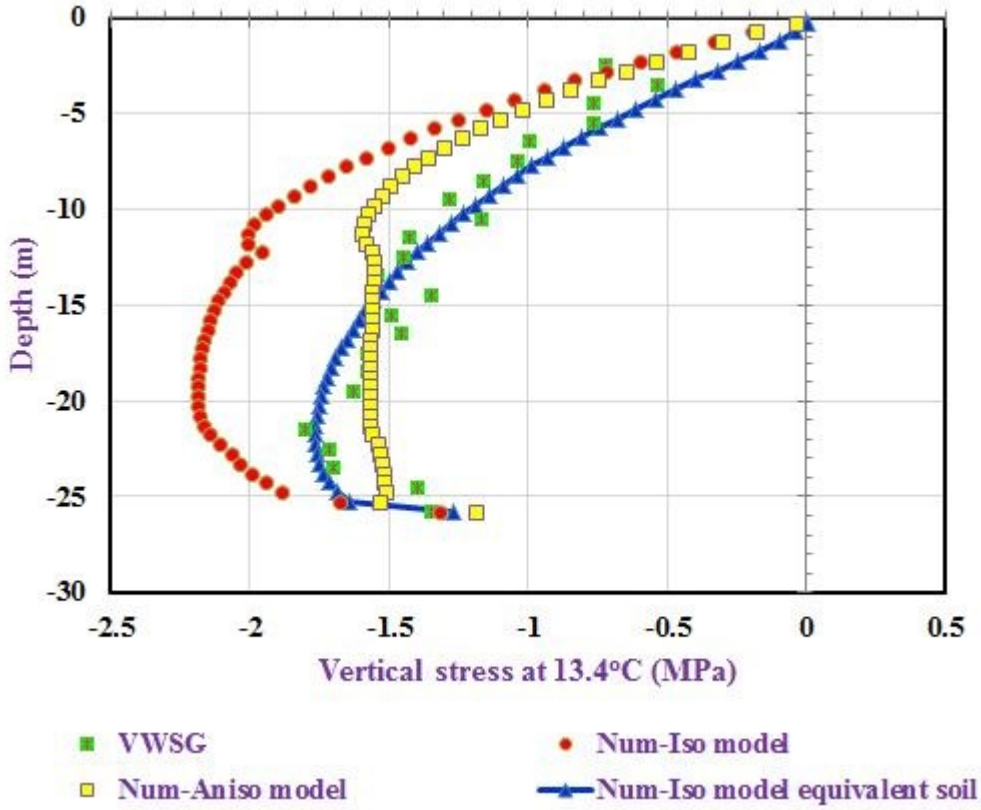

5.4.2 Mechanical and Thermal loading (T7)

The predicted displacements of the pile head in isotropic and anisotropic elastic soils generated by mechanical and thermal loads (Test T7) are shown in Figure 5.57. The predicted maximum head displacement is approximately 1.8 mm corresponding to the maximum temperature of 14^{o}C at the end of the heating phase. The trend of the predicted vertical head

displacements is not significantly affected by the different material models. Nevertheless, after 26 days the displacements predicted by different material models tend to differ.

Figure 5.57 Comparison of vertical displacement of the pile head versus time (T7)

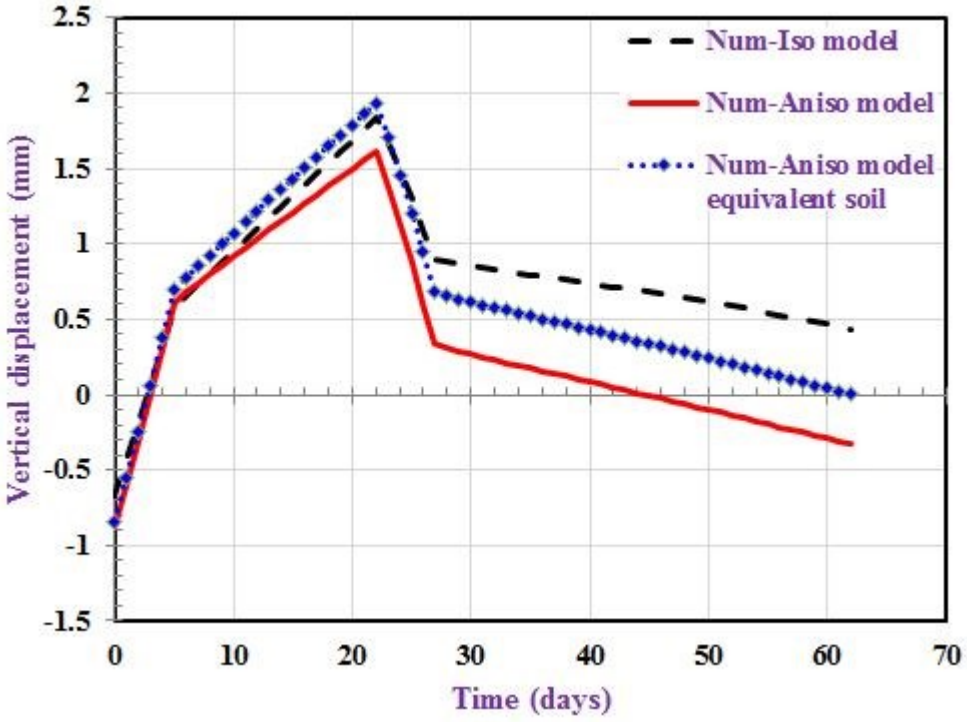

Figure 5.58 shows the axial strain at the maximum temperature of 14^{o}C versus depth for test T7 (mechanical and thermal loading). The strains predicted in isotropic elastic soils are larger than measured strains, especially at the pile tip where the predicted strain is almost 120 μm while the strain measured by VWSG is 85 μm. The magnitudes of predicted strains in the pile for equivalent isotropic and anisotropic elastic soils are larger than the measured strains in soils A1 and A2 and extend to the depth of 12 m. The best prediction of measured vertical strains is obtained for the anisotropic layered soil system.

The vertical strains in the pile versus depth show in Figure 5.58 corresponded to the vertical stresses in the pile depicted in Figure 5.59. The predicted stresses follow similar trends to the predicted strains (Figure 5.58). Again, the predicted axial stresses for anisotropic elastic layered soil profile provide better fit to experimental data than the other model.

Figure 5.58 Comparison of vertical strain in the pile versus depth (T7)

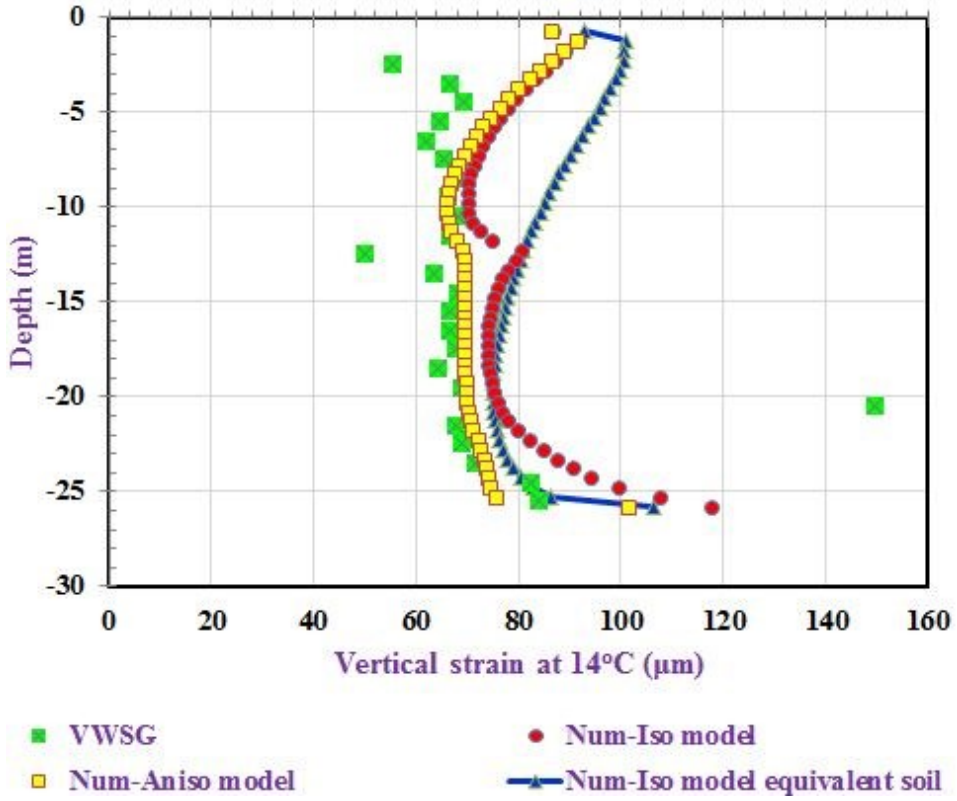

Figure 5.59 Comparison of vertical stress in the pile versus depth (T7)

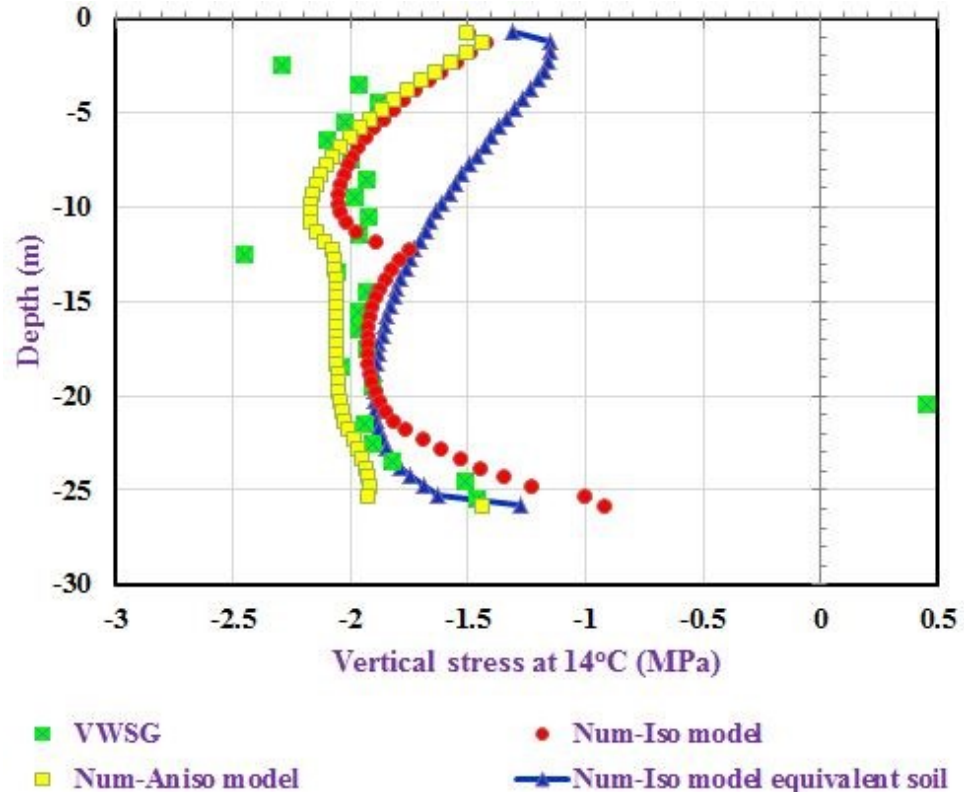

Chapter 6 - Conclusions and Recommendations

Thermo-active foundations decrease the use of fossil fuels by harvesting renewable geothermal energy. Their use an environmentally friendly and sustainable alternative energy source compared to the ones used by current heating and cooling practices. To advance knowledge about soil-structure interaction in HEP, coupled thermo-hydro-mechanical finite element modelling was conducted. This enabled identification of load-transfer mechanisms in a single energy pile under thermal as well as combined mechanical and thermal loading. The site located in Lausanne, Switzerland was selected for the computational modeling due to the abundance of the available experimental data. A four-story 100 m x 30 m building, which is supported by 97 drilled piled, was constructed at the Swiss Federal Institute of Technology. The in situ tests were conducted on a HEP, which is located at the side of the building

Due to the symmetry of geometry, load and soil profile only a half of the longitudinal pile section with a radius of 0.5 m and a length of 26 m was modelled. The selected model size of 10 m x 52 m resulted from the size sensitivity studies. The FE model consists of a total of 6,489 nodes and 2,080 elements. The pile was modelled by using 8 node biquadratic axisymmetric quadrilateral elements (CAX8R). The soil was modelled by using 8 node axisymmetric quadrilateral biquadratic displacements, bilinear pore pressure elements (CAX8RP). The contact between the pile and soil was assumed to be perfectly rough.

The modelling was performed in two runs. The first run conducted the heat transfer analysis in order to capture the heat transfer from the pile into the surrounding soil. The second run performed the coupled displacement-pore pressure analysis to obtain stresses, strains and pore pressures induced by the thermal loading from the first run. In test T1 (thermal loading only), the HEP was heated to a maximum of 21^{o}C during the heating phase, which was followed by a cooling phase with the ultimate temperature of 3^{o}C. In the case of test T7 (mechanical and thermal loads), the pile was subjected to mechanical load of 1000 kN. This was followed by thermal loading, during which the pile was heated to a maximum of 14^{o}C, and then subsequently cooled to 2^{o}C (Laloui et al., 2006).

In the FE model, the stress-strain relationship of the pile was assumed to be linear elastic and the soils are also assumed to behave as linear elastic materials. The soil profile that resulted from the field and lab investigations consists of five different layers. The alluvial soils A1 and A2 extend from the top soil surface to a depth of 12 m. Beneath these soils is the sandy gravel moraine B from the depth of 12 m to 22 m. The moraine C is located below soil B and it extends until the depth of 25.5 m. The molasses D is the weak sandstone extending to the maximum depth explored.

This study has been conducted for two different soil models:

1) Isotropic elastic 2) Anisotropic elastic model.

6.1 Conclusions

Based on the results of the 2D coupled thermo-hydro mechanical modeling presented in Chapter 5, the following conclusions are derived from this research:

1. The predicted radial strain in the pile is not significantly affected by the degree of the soil anisotropy.
2. For the end bearing heat exchanger pile, the null point was found to be very close the pile tip.
3. Maximum thermal axial strains occurred at the pile head at the end of heating period. It was also found that heating induced additional compressive stresses in the pile while increasing the mobilized shear stresses in the surrounding soils. More importantly, the heating induced a negative skin friction in the upper portion of the pile. This might cause at least a temporary decrease in the overall bearing capacity of the pile, which is of a vital importance for design.
4. The stresses induced by the thermal loading (at the end of the heating phase) were found to be greater than those generated by the mechanical loading.
5. The history of the temperature imposed on the pile will affected the displacements, strains and stresses generated in the pile. The plot of the displacements versus time corresponds to the temperature history.
6. At the same history temperature imposed on the pile, the stresses induced by the thermal in both case: thermal, and mechanical and thermal loading do not change.

7. When the pile was embedded in the layered systems, the difference stress levels result from different types of surrounding soils and layer boundaries was clearly indicated.
8. It should be noted that in most cases the direction of shear stress during cooling reversed to the positive sign. This will lead to development of tensile stresses in the pile surrounded by these soils. So far, the magnitudes of these tensile stresses have been well within the accepted limits for the reinforced concrete.
9. In general, for this study the anisotropic elastic model is the appropriate model to consider the behavior of the HEP when the pile was subjected to thermal, and mechanical and thermal loading.

In summary, this research provides a contribution toward wider use of energy pile by advancing the knowledge that is necessary for the design.

6.2 Recommendations

Recommendations for the future research in the area of computational modeling of HEP include:

1. Analyze the effects of temperature changes on the stresses, strains and pore pressure in the surrounding soil.
2. Analyze the effects of multiple thermal loading cycles on the stresses and strains in the energy pile.
3. Conduct 3D thermal-hydro-mechanical modeling by using elastic and if needed elastoplastic soil material models to explore the behavior of a pile group from both thermal and mechanical perspectives.

References

1. ABAQUS Inc. (2013). Abaqus Analysis User's Guide 6.13-2

2. ABAQUS Inc. (2013). Abaqus/CAE User's Guide 6.13-2

3. Alex Morris and Andrea Sheets (2009). Geothermal Systems; Systems Types, Applicabaility and Environment Impacts. UTSoA – Seminar in Sustainable Architecture.

4. Amatya B. L., Soga, K., Bourne-Webb, P. J., Amis, T., and Laloui, L. (2012). Thermo-mechanical behavior of energy piles. Géotechnique 62, No. 6, 503-519.

5. American Concrete Institute. Building code requirements for structural concrete (ACI 318-11) and commentary; August 2011.

6. Andersland, O. B. and Ladanyi, B. (1994). An Introduction to Frozen Ground Engineering. Chapman & Hall. One Penn Plaza, NewYork, NY 10119.

7. Bourne-Webb, P. J., Amatya, B., Soga, K., Amis, T., Davidson, C., and Payne, P. (2009). Energy pile test at Lambeth College, London: geotechnical and thermodynamic aspects of pile response to heat cycles. Géotechnique 59, No. 3, 237-248.

8. Brandl, H. (2006). Energy foundations and other thermos-active ground structures. Géotechnique 56, No. 2, 81-122.

9. Clauser, C. (2006). Geothemal Energy. In: K. Heinloth (ed), Landolt-Börnstein, Group VIII: advanced Materials and Technologies, Vol. 3: Energy Technologies, Subvol. C: Renewable Energies, Springer Verlag, Heidelberg-Berlin, 493-604.

10. Deep Foundations Institute. Deep foundation magazine: Jan Feb 2014. http://viewer.epaperflip.com/viewer.aspx?docid=932afa9c-e893-437e-951f-a2ab00d337fc (accessed 2 Feb 2014).

11. Farouki, O. T. (1981). Thermal Properties of Soils. CRREL Monograph 81-1. U.S Army Cold Regions Research and Engineering Laboratory, Hanover, New Hampshire 03755.

12. Ghildyal, B. P. and Tripathi, R. P. (1987). Soil Physics. Wiley Eastern Limited, New Delhi 110002, India.

13. Graham, J. and Houlsby, G. T. (1983). Anisotropic Elasticity of a Natural Clay. Géotechnique 33, No. 2, 165-180.

14. Kelly, R. (2011). Going Underground. The Journal of the American Institute of Architects 2011; http://www.architectmagazine.com/technology/going-underground_o

15. Kersten, M. S. (1949). Thermal Properties of Soils. Bulletin No. 28. University of Minnesota Institute of Technology, Engineering Experiment Station; Vol. LII, No.21.

16. Kluitenberg, G. J. (2014). Soil Physics: Lecture Note. Department of Agronomy, Kansas State University, Manhattan, Kansas.

17. Knellwolf, C., Peron, H., and Laloui, L. (2011). Geotechnical analysis of heat exchanger piles. Journal of Geotechnical and Geoenvironmental Engineering 2011; 137: 890-902.

18. Laloui, L., Moreni, M., Steinmann, G., Vulliet, L., Fromentin, A., and Pahud, D. (1999). Test en conditions réelles du comportement statique d'un pieu soumis à des solicitations thermos-mécaniques. Report of the Swiss Federal Office of Energy 1999.

19. Laloui, L., Nuth, M., and Vulliet, M. (2006). Experimental and numerical investigations of the behavior of a heat exchanger pile. International Journal for Numerical and Analytical Methods in Geomechanics 2006; 30:763-781.

20. Lee, S. R. (2009). Energy Piles. Department of Civil and Environmental Engineering KAIST.

21. Lund, J. W., Freeston, D. H., Boyd, T. L. (2010). Direct Utilization of Geothermal Energy 2010 Worldwide Review. Proceedings World Geothermal Congress 2010, Bali, Indonesia, 25-29 April 2010.

22. McCartney, J. S., Murphy, K. D. (2012). Strain distributions in full-scale energy foundations. DFI Journal 2012 Vol.6, No. 2, 26-38.

23. Mimouni, T., Laloui, L. (2014). Towards a secure basis for the design of geothermal piles. Acta Geotechnica 2014; 9: 355-366.

24. Mitchel, J. K. and Soga, K. (2005). Fundamentals of Soil Behavior. 3rd Edition. John Wiley & Sons, Inc., Hoboken, New Jersey.

25. Murphy, K. D., McCartney, J. S., Henry, K. S. (2014). Evaluation of thermo-mechanical and thermal behavior of full-scale energy foundations. Acta Geotechnica 2014.

26. RETScreen International, Clean Energy Decision Support Centre (2001-2005). Ground-Source Heat Pump Project Analysis Chapter. Minister of Natural Resources Canada 2001-2005.

27. Richter, D. and Simmons, G. (1974). Thermal expansion behavior of igneous rocks. Int. J. rock Mech. Min Sci. & Geomech. Astr., Vol. 11, No.10, pp. 403-411.

28. Stewart, M. A. and McCartney, J. S. (2014). Centrifuge modelling of soil-structure interaction in energy foundations. Journal of Geotechnical and Geoenvironmental Engineering 2014. 140.

29. Sundberg, J. (1988). Thermal Properties of Soils and Rocks. Geologiska Institutionen Publ. A 57, Dissertation, Göteborg Sweden.

30. Van Wijk, W. R. and De Vries, D. A (1963). Physics of Plant Environment. North-Holland Publishing Company-Amsterdam. Interscience Publishers, a division of John Wiley & Sons, Inc.-New York.

31. Wood, D. M. (1990). Soil Behaviour and Critical State Soil Mechanics. Press Syndicate of the University of Cambridge, the Pitt Building, Trumpington Street, Cambridge CB2 1RP.